UNIVERSITÀ DEGLI STUDI DI
MILANO - BICOCCA

DIPARTIMENTO DI SCIENZA DEI MATERIALI

TESI DI DOTTORATO DI RICERCA IN
NANOSTRUTTURE E NANOTECNOLOGIE
CICLO XXII

SYNTHESIS AND CHARACTERIZATION OF SEMICONDUCTOR NANOPARTICLES AND HYBRID NANOCOMPOSITES FOR OPTOELECTRONIC APPLICATIONS

DR. SILVIA MASALA

UNIVERSITÀ DEGLI STUDI DI
MILANO - BICOCCA

DIPARTIMENTO DI SCIENZA DEI MATERIALI

TESI DI DOTTORATO DI RICERCA IN
NANOSTRUTTURE E NANOTECNOLOGIE
CICLO XXII

SYNTHESIS AND CHARACTERIZATION OF SEMICONDUCTOR NANOPARTICLES AND HYBRID NANOCOMPOSITES FOR OPTOELECTRONIC APPLICATIONS

Tutors	*Candidato*
PROF. MAURIZIO DE CRESCENZI DR. TIZIANA DI LUCCIO	SILVIA MASALA

Coordinatore
PROF.
LEONIDA MIGLIO

ANNO ACCADEMICO 2009-2010

to my beloved mum

Contents

Introduction

Interest in nanoparticles and nanocomposites of hybrid organic/inorganic materials has increased considerably over the last decade, an interest that has been fueled by novel and exciting potential applications of these materials as electronic devices such as organic light emitting diodes, solar cells and sensors. Group IV semiconductors as well as compounds formed with group II-VI elements are among the most used inorganic materials in this field, mainly because their physical properties can be significantly altered at the nanoscale.

The focus of this thesis is on the realization and the study of size-dependent modification of the electronic properties of two classes of semiconductors, germanium (Ge) and cadmium sulfide (CdS). Germanium is an indirect semiconductor of particular interest because it exhibits a more pronounced quantum confinement effect than silicon, and offers efficient visible luminescence at the nanoscale. CdS is an extensively studied direct band gap semiconductor compound. It is characterized by strong optical absorption in the visible range and n-type behavior. Nanometer-size particles of CdS are excellent emitters in the visible range—they offer narrow emission, broad absorption and high photostability. Both Ge and CdS have great potential in various applications such as optoelectronic devices.

Extensive research has been devoted to the preparation of semiconductor nanoparticles. Different approaches, compatible with silicon based technology, have been carried out to achieve the growth of nanocrystals of high Ge content (density), with diameters less than 10 nm. Concerning the synthesis of CdS nanoparticles, several consolidated methods that generally involve complex control processes, long synthesis times, and the use of hazardous solvents and reagents have been developed. The main aim of all these synthesis methods is to obtain nanoparticles with a high degree of crystallinity, and controlled size (size distribution) and shape. On the other hand intensive effort has been focused on the development of methods to prepare hybrid nanocomposites. Typically the polymerization of monomers and the preparation of inorganic nanoparticles are carried out separately, with the two components being combined in a subsequent step. However, alternative methods involving the simultaneous polymerization of the organic monomer and reaction of the nanoparticle precursor(s) exist.

In this thesis an investigation of the physical properties of Ge nanocrystals prepared by a consolidated method, so as to achieve nanostructures on silicon dioxide substrates, is presented. Concerning the synthesis of CdS, a rapid and inexpensive method that avoids the mixing of toxic reagents and solvents has been developed for the preparation of colloidal nanoparticles and (CdS) nanoparticle/polymer nanocomposites. In particular the CdS based nanocomposites were realized by two main classes of synthesis: ex- and in-situ. With respect to the former class, the nanocrystals were synthesized in a solvent, then extracted and subsequently combined with a polymer. In the case of the latter class, the nanocrystals were produced directly in the polymer matrix. In both cases the nanoparticles were synthesized by adopting the method of the thermolysis of a single source precursor. Beyond the synthesis, several characterization techniques have been employed to study the chemico-physical, optical and structural properties of both the Ge and CdS nanoparticles and nanocomposites. These include Scanning Tunnel Microscopy (STM), X-ray Photoelectron Spectroscopy (XPS), Nuclear Magnetic Resonance (NMR), Fourier Transform-Infrared Spectroscopy (FT-IR), UV-Vis absorption and photoluminescence (PL) spectroscopy, Atomic Force Microscopy (AFM), Transmission Electron Microscopy (TEM), Wide Angle X-ray Scattering (WAXS) and Grazing Incidence x-ray Diffraction (GID). The latter two synchrotron based techniques were performed during the synthesis process.

This thesis may be divided into four main areas of study:

1. With the aim of investigating quantum size effects in Ge nanoparticles, high density Ge nanoparticle samples have been realized via a method of high temperature vacuum evaporation onto SiO_2 substrates. By means of electrochemical photocurrent measurements, (a) the ability of the Ge nanoparticles to generate photocurrents in the near ultraviolet and visible spectral ranges and (b) the

strong dependence of the photocurrent features on the Ge nanoparticle size are demonstrated.

2. Concerning the II-VI compounds, CdS nanoparticles have been fabricated by thermolysis of a Cd precursor in octadecene (ODE), an ex-situ method. Sample preparation under varying conditions—precursor concentration, temperature, and annealing time and rate—was carried out. The dependence of nanoparticles size (size distribution) and crystal structure on the annealing conditions has been studied by means of optical and morphological measurements as well as by real time scattering experiments. Some examples of dispersion of nanoparticles in polymers are also presented.

3. In accordance with an in-situ method, CdS nanoparticle-based nanocomposites have been prepared by thermolysis of a Cd precursor in different polymeric matrices, firstly employing a dielectric polymer (e.g. Topas, Tp) and then later conductive polymers like poly(N-vinylcarbazole) (PVK) and poly(3-hexylthiophene) (P3HT). Success in the synthesis of CdS nanoparticles in the 2-5 nm (diameter) range for all polymers employed is demonstrated. Particle size is enhanced by increasing the annealing temperature.

4. Electrical properties of nanocomposites prepared via both methods (see above) have been investigated by realizing simple stack devices, e.g. ITO-CdS/polymer-LiF-Al (ITO = indium tin oxide substrate). Such devices were studied by performing current-voltage, electroluminescence and photocurrent measurements. It is deduced from different experiments that the synthesis method adopted can be extended to several polymer producing nanocomposites with improved electro-optical properties.

The thesis is organized as follows:

- Chapter 1 reviews the theory of solids at low dimensions, and summarizes the key effect of reduced dimensionality on semiconductor properties.
- In Chapter 2 a description of the synthesis of germanium quantum dots on SiO_2 substrate is given, followed by a presentation of quantum size effects observed

by STM. Photo-electrochemical experiments that demonstrate the capability of Ge dots to generate photocurrent are then described.

- The properties of CdS at the nanoscale as well as a discussion on the present and possible future technological impact of such nanoparticles are presented in the Chapter 3. An overview of state-of-the-art methods for synthesis CdS nanoparticles is given followed by a report on the synthesis and characterization of CdS nanoparticles prepared in octadecene by thermolysis of Cd bis-thiolate. Discussion on the possible advantages and drawbacks of the proposed synthesis method is made.

- Chapter 4 begins with a discussion on the importance of hybrid nanocomposites in advanced technologies, after which a thermolytic route allowing the growth of CdS nanoparticles in a polymer matrix is described. Studies of the growth of CdS nanoparticles in Topas by synchrotron diffraction and optical experiments are subsequently reported.

- The synthesis and the optical characterization of CdS nanoparticles in a conductive polymeric foil of poly(N-vinylcarbazole) (PVK) are reported in Chapter 5. The results of electrical measurements made on single layer devices are discussed, comparing nanocomposites with CdS particles of different (average) size. The electrical properties of in- and ex-situ prepared nanocomposites are also compared−the ex-situ nanocomposites were prepared using commercially available, chemically stabilized CdS nanoparticles as well as nanoparticles obtained by thermolysis in octadecene.

- In Chapter 6, synthesis by thermolysis of CdS in poly(3-hexylthiophene) (P3HT) is described, and possible applications of the realized nanocomposites are proposed. In particular, improvements in both the performance of hybrid organic - inorganic solar cells and organic light emitting devices (OLED) are demonstrated.

- The final paragraph concludes the thesis work.

Chapter 1

Survey of quantization effects in low dimensional solids

Prior to the early 1990s the properties of solid crystalline materials were typically defined without any specific reference to their size. However the nanometer size regime has revealed interesting properties such as the tailoring of macroscopic properties of materials via size and shape control. For this reason semiconductor materials at nanometer size have been widely investigated. They led to many innovations in diverse areas as non-traditional materials with unique properties crossing over the limitations of existing materials and going beyond. The semiconductor nanoparticles are characterized by tunable optical properties. For this reason they are exploited for many applications from fluorescent tags to lasers, from OLED to solar cells, impacting dramatically the development of electronic and optical devices. Today, despite the fact that well consolidated results in the synthesis and study of their physical properties has been reached [1] [2], and there are commercially available products, the interest for semiconductor nanoparticles is still wide and there is a continuing extensive research on nanoparticles of group IV or II-VI for advancement in synthesic routes and technological applications. In the following sections we introduce some theoretical concepts related to the physics of materials at nanometer size and we list some scaling laws induced by the low dimensionality.

1.1 Theoretical approach to quantum confinement effect

The optical, electrical, and structural properties of solids are generally defined for bulk state. In bulk materials electrons and holes are described as a superposition of plane waves, extended throughout the solid. The band structure and the physical properties of the solid can be calculated by means of complex theoretical models which can be simplified considering two basic assumptions, the conservation of translational symmetry and the neglect of contribution from the surface by assuming an infinite solid (periodic boundary conditions)[3].

In metals in a bulk state the energy levels are so close to each other that they are considered as continuous. In semiconductors some energy levels are calculated quantum mechanically as forbidden energy levels defining the so called band gap which is different for each bulk material. The band gap is also defined as the energy required to create an electron hole pair at rest with respect to the lattice and far enough apart so their Coulomb attraction is negligible. If one of the carrier approaches to the other, they may form a bound state, a Wannier exciton. A free exciton is a bound electron-hole pair that has a binding energy of few meV. The pair acts as a single hydrogenic particle and is free to move in a perfect crystal, in other words such excitations are not spatially bound to a region smaller than the natural charge separation distance (Exciton Bohr Radius a_B). It is possible to calculate the energy of the excitonic bound state using the Bohr's hydrogen model that gives:

$$E_{ex} = \frac{m^*}{m_0}\frac{1}{(k\varepsilon_0)^2}(13.6)eV \tag{1.1}$$

where m^* is the reduced effective mass ($1/m^* = 1/m_h + 1/m_e$ and m_e and m_h are the electron and hole effective mass respectively), m_0 is the electron rest mass, ε_0 is the permittivity of free space and k is the dielectric constant.

In a solid the De Broglie wavelength of an electron and a hole λ_e, λ_h and the Bohr radius of an exciton, a_B can be considerably larger than the lattice constant a_L. Therefore it is possible to create a mesoscopic structure which is in one, two, or three dimensions comparable to or even less than λ_e, λ_h, a_B but still larger than a_L. In these structures elementary excitations will experience quantum confinement resulting in a finite motion along the confinement axis and infinite motion in other directions. If the motion of electrons, holes, and excitons is restricted in all three directions, we come to a quasi-zero dimensional system, the so called quantum dot.

In nanocrystals, the assumptions of translational symmetry and infinity of the bulk are not valid any more, therefore a new approach is needed. The confinement effects can be understood by using the quantum mechanical model of the particle in a box in the framework of the effective mass approximation (EMA), in other words, by considering that the nanocrystals are a receptacles of electron and holes whose effective masses are the same as in the ideal infinite solid of the same stoichiometry.

As found out by Brus et al. in 1984 [4], the minimum energy (energy gap, $E_g(nano)$), required for creating an exciton in a 0-dimensional system mainly depends on three important contributors. The first contributor is the bulk band gap energy ($E_g(bulk)$) of the nanocrystal, the second is the energy for the confinement of carriers. This term can be calculated starting from the Heisenberg's uncertainty coupled with the energy dependance on the square of the wavevector, obtaining the following expression:

$$E_n = h^2 n^2 / 8 m^* R^2 \tag{1.2}$$

where h is the Plank constant (6.6×10^{-34} Js) and R is the radius of the nanostructure. Eq. 1.2 states the confinement energy for carriers in a quantum well and shows that the levels are no longer continuous but rather discrete. The third contributor comes from the Coulomb screening interaction potential that is proportional to 1/R. By combining the three contributors the ground state solution of the stationary Shroedinger equation becomes:

$$E_g(nano) = E_g(bulk) + \frac{h^2}{8R^2 m^*} - \frac{1.8q^2}{\varepsilon R} \tag{1.3}$$

Employing the Eq. 1.3 and considering that the Coulomb term affects the particles size value by 10%, the confinement effect become the dominant in the size calculation and it is possible to predict the widening and the blue shift of nanocrystals band gap respect to its bulk phase.

Beyond the widening of the band gap and the discretization of the energy levels with reducing size, materials at low dimension experience the transformation of the density of states as function of energy. The density of electron and holes states can be expressed

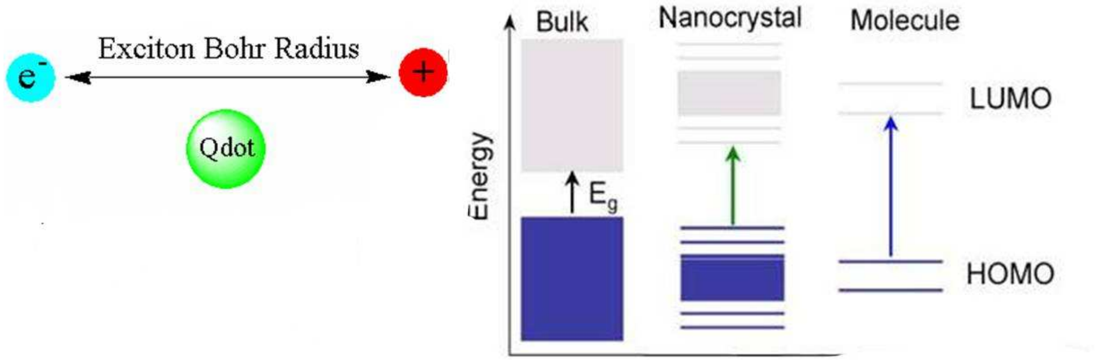

Figure 1.1: *Size difference between QD and exciton Bohr radius (www.evidenttech.com)(left side). Bulk and confined energy levels in nanocrystals compared to molecular orbital energy-level diagram (right side).*

in the general form

$$\rho(E) \propto E^{d/2-1} \tag{1.4}$$

where $d = 1, 2, 3$ is the dimensionality and the energy is measured from the bottom of the conduction band for electros and from the top of the valence band for holes. In the three dimensional system $\rho(E)$ is a smooth square-root function of energy. In the case of d=2 and d=1, a number of discrete subbands appear due to the quantum confinement effect and the density of states follows the Eq. 1.4 within every subband. For quasi-zero dimensional system the density of states is described by a set of $\delta - functions$. As a consequence, from the density of state perspective nanocrystals lies between the discrete atomic and the bulk continuous band limit (Figure 1.1).

Surface effects: free energy variation

The macroscopic properties of nanocrystals such as the inherent size dependence of optical signals are also the result of free energy variation. Since the nanocrystals are typically made up of ten to thousands of atoms, geometric considerations promote a very high surface to volume ratio compared to the bulk version. The surface atoms contribute proportionally to the total free energy so the nanocrystals exhibit significantly differentiated thermodynamic properties respect to the bulk phase.

Nanocrystals thus can have their free energy manipulated in a controlled manner by changing the crystal size.

1.2 Scaling laws

The combination of low dimensionality and the contribution from the surface are responsible for the existence of scaling laws [5]. Some of them are summarized as follows.

- *Size dependence of the melting temperature.* The melting temperature in nanocrystals is lower with respect to the bulk phase [6] [7], this happens because surface energy is always lower in the liquid phase compared to the solid phase. Consequently the surface atoms prefer to reach earlier the liquid state, where they can minimize their energy. The decrease of the melting temperature is approximately dependent on the inverse of nanocrystals radius.

- *Size dependence of the structural phase transitions.* When a pressure is progressively applied to a crystal a structural phase transition can occur: the crystal becomes more stable in a new, more compact phase. Real crystals have a certain number of defects (point, linear and planar). It is documented that structural phase transitions nucleate on one or more of these defects and then propagate along the solid. Defects act as catalyst for the phase transition. This mechanism contributes to significantly lower the pressure that must be applied in order to induce the phase transition. Nanocrystals are usually so small that the probability of occurrence of defects is very low. Phase transitions occur via different mechanisms and require higher pressures.

- *Coulomb blockade effect.* The energy required to add successive charges onto an extended (bulk) crystal does not vary. In a nanocrystal the presence of one charge acts to prevent the addition of another. Thus, in metals or semiconductors, the current voltage curves of individual crystallites resemble an additive step function like a staircase. This effect is called Coulomb blockade [8]. The Coulomb energy scales as 1/R, being R the radius of the confined structure.

- *Superparamagnetism in nanomagnets.* When the size of ferromagnetic materials decreases below a certain threshold, there is an increasing chance that it will be composed of a single ferromagnetic domain. Nanomagnets tend to be then perfectly aligned along a magnetic field. Their magnetization curve has no hysteresis, that is, there is no memory of the field when it is turned off. An ensemble of nanomagnets behaves as a single, giant, paramagnetic atom and the direction of magnetization is easily influenced by thermal fluctuations of the local environment (superparamagnetism) [9].

- *Tunable absorption and emission behavior.* The change of optical properties are the most interesting effect of semiconductors at low dimensions particularly in quantum dots. As result of quantum confinement effect the band gap of quantum dots varies with size of the nanocrystals and is always larger than that of its bulk state. The absorption spectrum of quantum dots can be considered as overlapping peaks corresponding to a transition between different exciton energy levels. The wavelength corresponding to the first exciton absorption in UV visible spectrum of a quantum dots is called absorption onset and depends on the size of the nanocrystals. Excited electron returns to ground state through radiative recombination with the hole (fluorescence). Consequently tunable emission can be obtained by varying the nanocrystals size. The peak emission is bell-shaped (Gaussian) and occurs at a slightly longer wavelength than the lowest energy exciton peak (the absorption onset). The energy separation between absorption and emission is referred as the Stoke's shift and originates from the loss of some energy during the exciton lifetime.

  Quantum dots are characterized by narrow emission profile which is generally required for minimum overlap of emitted colors. This is one of the many advantages of quantum dots over organic fluorophores. The bandwidth of the emission spectra expressed as the Full Width at Half Maximum (FWHM) gets larger with the increasing size distribution of the quantum dots. Moreover it depends on the temperature and the natural spectral line width of the dots.

Bibliography

[1] C.B. Murray, D.J. Norris, M.G. Bawendi, J. Am. Chem. Soc. 115, 8706, (1993).

[2] D.J. Norris, M.G. Bawendi, L. E. Brus, *Optical properties of semiconductor nanocrystals (quantum dots), in Molecular Electronics* (Eds.: J. Jortner, M. Ratner), Blackwell, Oxford, 281,(1997).

[3] N.W. Ashcroft, N. David Mermin, *Solid State Physics*, Sounders college, Philadelphia.

[4] L.E. Brus, J. of Luminescence 31, 381-4 (1984).

[5] . A.P. Alivisatos, Phys. Chem. Chem. Phys. 101, 1573, (1997).

[6] A.P. Alivisatos, J. Phys. Chem. 100, 13226, (1996).

[7] P.Buffat, J.P. Borel, Phys. Rev. A 13, 2287 (1976).

[8] . D.L. Klein, P.L. McEuen, J.E.B. Katari, R. Roth, A.P. Alivisatos, Appl. Phys. Lett. 68, 2574 (1996).

[9] . I.M.L. Billas, A. Chatelain, A.W.A. deHeer, Surface Review and Letters 3, 429 (1996).

Chapter 2

Germanium nanoparticles: synthesis and study of their optoelectronic properties

In this chapter we report the realization and characterization of germanium (Ge) nanoparticles (quantum dots). This project has been developed at University of Roma ”Tor Vergata”, in the research group of Professor Maurizio De Crescenzi [1] [2]. The quantum dots have been characterized by scanning tunnel microscopy (STM) and spectroscopy (STS) in order to investigate the quantum confinement effect in Ge at nanometer size. The optoelectronic properties and in particular the photocurrent generation by quantum confined Ge have been investigated by using electrochemical measurements.

2.1 Introduction

Quantum dots of indirect-gap semiconductors such as Ge are widely studied due to their quantum confinement effects, which cause changes in their electronic and optical properties. The energy band gap of Ge is equal to 0.66eV in the bulk state but it changes with the size [3] [4] Moreover Ge is characterized by a large excitonic Bohr radius of 11.5nm, thus the quantum confinement effects in this semiconductor material are easily observable. As confirmed experimentally by spectroscopy analysis [5] the quantum confinement effect increases strongly in Ge than in Silicon (Si) Many photoluminescence (PL) studies of Ge nanocrystals have been performed since the report of blue luminescence from Ge nanocrystals embedded in SiO_2 matrixes [6] [7] Such PL results have been explained in terms of both quantum confinement effects and interface effects [6] The mentioned properties make the Ge quantum dots promising for many applications in optoelectronics [8]

The epitaxial growth of Ge on Si has been widely investigated. The Ge growth on Si proceeds via the Stranski-Krastanov mode [9]. According to this mechanism an epitaxial wetting layer forms on Si surface and when a critical thickness of few monolayers is reached the 3D Ge islands formation starts. As a result self-assembled Ge quantum dots on Si substrates can be produced in a way that is compatible with the Si technology. There are some drawbacks related to this growth mechanism. The lateral size of the dots is about 20 - 40 nm while the height is usually one order of magnitude less, thus the nanoclusters appears as domlike structures. The Ge dots density on Si surface is limited to $10^9 - 10^{10}\ cm^{-2}$. Moreover the epitaxial growth can promote important interdiffusion effects leading to GeSi alloys at the interface. On the other hand the Ge nanodots on an oxidized Si surface created by a procedure reported by Ichikawa et al.[10] have attracted a wide interest in the Si-based technology (Figure 2.1). The main advantages of this procedure are the preparation of uniform-size nanodots with very high density $10^{12} cm^{-2}$, the tunable control of dot size ranging from a few nanometers in diameter and the formation of nanoclusters which are is actually a sphere.

Spectroscopic measurements of the valence maximum band and of the conduction band minimum are generally employed to evaluate the energy band shift as a function of Ge dots size [14] Among the most recent works, Scanning Tunnelling Microscopy (STM) and Spectroscopy (STS) measurements are used to prove the widening of the band gap by reducing the Ge dot size [15] In this work we used ultrathin SiO_2 films thermally deposited on Si(100) substrate to obtain ultrahigh dense nucleation of Ge dots. We characterized the samples by STM and investigated the possible use of Ge dots for photovoltaic applications.

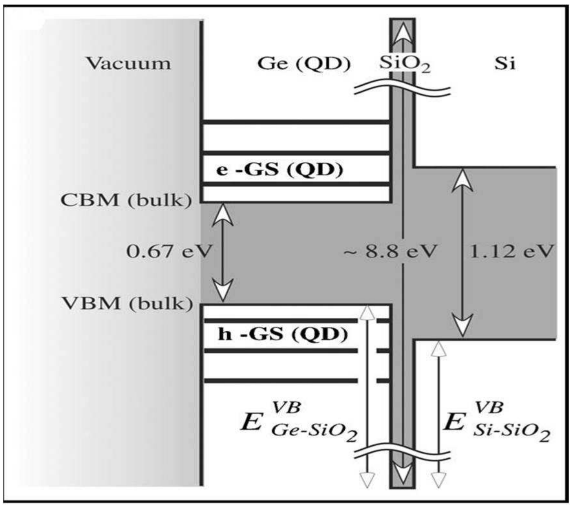

Figure 2.1: *Schematic band structure of Ge in bulk state or as quantum dots, between vacuum and an ultrathin SiO_2 film on a Si substrate. Bulk valence band maximum V_{BM} and conduction band minimum C_{BM} at each material are traced by thin lines. Size of bulk band gaps at room temperature are written for Ge, SiO_2, and Si (Refs. [11] [12] [13]).*

2.1.1 Scanning tunnel microscopy: generalities

Scanning tunnel microscopy belongs to Scanning Probe Microscopy (SPM) techniques. All of the techniques are based upon scanning a probe, typically a metallic tip, just above a surface monitoring some interaction between the probe and the surface. The interaction monitored in STM is the tunneling current between a metallic tip and a conducting substrate which are in very close proximity but not actually in physical contact. This technique provides information about the surface structure at atomic level. In order to get such information the position of the tip with respect to the surface must be very accurately controlled (to within about $0.1\AA$) by moving either the surface or the tip. The tip must be very sharp, ideally terminating in just a single atom. According to the quantum mechanical tunnelling theory the electrons can tunnel through a potential barrier (between the tip and the sample) which is classically forbidden. The probability of tunnelling is exponentially-dependent upon the distance of separation between the tip and surface: the tunnelling current is therefore a very sensitive probe of this separation. STM is able to measure the local density of states of a material at it surface as a function of lateral (x-y) position on the sample, surface and energy of the electrons. An STM can typically control the current that flows between the tip and the sample (I), the bias voltage between the tip and the sample (V), the xy (in sample plane) position of the tip, and the z (perpendicular to sample plane) distance between the tip and sample. Using these variables, by the scanning tunnel spectroscopy technique (STS), an STM is able to measure the Local Density of States (LDOS) of a material as function of position on the surface (controlled by where the tip is above the surface) and as a function of energy. The LDOS is proportional to the differential increase in tunnelling current given a differential increase in bias voltage. In other words the LDOS can be obtained by measuring dI/dV.

2.1.2 A brief introduction to photovoltaic effect

The photovoltaic (PV) effect, i.e. the production of electric power from sun light energy is based on the creation of excited states induced by photons absorption in the active material. The excited states are in turn, the source of free charge pair electron and hole. In a solar cell which is basically a p-n diode the photo-generated charges are separated with the help of the junction between the donor and the acceptor material in the active layer and transported and collected at the opposite electrodes as a result of an internal electric field generated by the difference in their Fermi levels (Figure 2.2). To have an optimum PV efficiency it is necessary to have the maximum charge separation efficiency and fast charge transfer process. Moreover the optimum band gap Eg of the active material should be 1.1 eV < Eg < 2 eV in order to maximize the photon absorption from the solar spectrum.

The current-voltage characteristic of an ideal cell resemble that of a standard diode following the thermoionic injection model [19]:

$$I = I_s(exp(\frac{qV}{kT} - 1)) \tag{2.1}$$

where q is the elementary charge, I_s is the saturation current under reverse bias, k is the Boltzmann's constant, T is the temperature in Kelvin and V is the bias in Volt. Under illumination the Eq.2.1 become:

$$I = I_s(exp(\frac{qV}{kT} - 1)) - I_{PV} \tag{2.2}$$

where I_{PV} is the photogenerated current.

There are several ways to describe the electrical characteristics of solar cells under

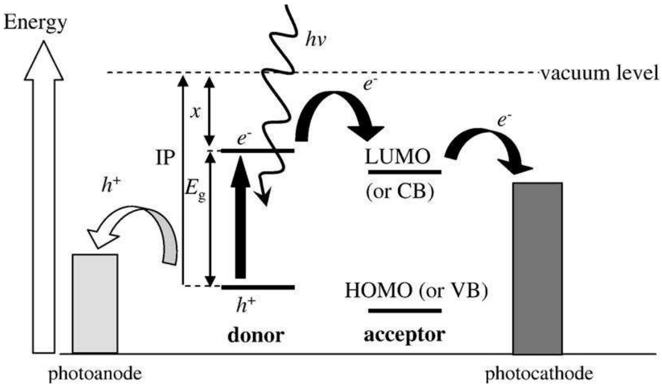

Figure 2.2: *Principle of a solar cell with energy band scheme. The symbols* e^- *and* h^+ *represent electrons and holes. The electron affinity and ionization potential are shown as* χ *and IP, respectively. LUMO and HOMO are the lowest unoccupied molecular orbital and highest occupied molecular orbital, respectively. CB and VB represent the conduction and valence bands, respectively [7].*

illumination. The most relevant is the power conversion efficiency η being the ratio of the maximum obtainable electrical power P_{max} and the incident light power (I_L).

$$\eta = \frac{P_{max}}{I_L} \times 100 \tag{2.3}$$

The point of maximum obtainable electrical power is located in the fourth quadrant of the current density-voltage curve, where the product of current and voltage reaches its maximum value

Another important value in the study of cell performance is the Incident-Photon-to-electron Conversion Efficiency (IPCE), it corresponds to the effectiveness of a solar cell to convert incident photons of a given wavelength into photocurrent:

$$IPCE(\lambda) = \frac{1240 J_{SC}(\lambda)}{\lambda I_L(\lambda)} \times 100 \tag{2.4}$$

where $J_{SC}(\lambda)$ is the short circuit current density in mA/cm^2, λ is in nm, and I_L the intensity of impinging light in mW/cm^2. Measuring the IPCE at different wavelengths results in a spectral response of the solar cells.

It is worth remembering that apart from monochromatic light, continuous irradiation under standard test conditions (Air Mass 1.5 Global, IEC 904-3, at cell temperature of 25^oC) is required for meaningful evaluation and for the proper comparison between different IPCE spectra.

In principle the IPCE as function of photon wavelength, should be proportional to the absorbance Abs(λ). For a conventional solar cell device, the photogenerated current density J is related to the generation rate G(z) and to the collection probability P(z), that is the probability that the generated carrier in the active material will be collected. The parameters G and P are related according to the following equation.

$$J = q \int^{d} G(z)P(z)dz \tag{2.5}$$

where d is the device thickness and q is the elementary charge. The generation rate can be related to the derivative of the transmittance T(λ) plus the reflectance R(λ) respect to z. At the same time T(λ) and R(λ) are defined as the percentage of impinging light that is transmitted or reflected at a given thickness, d, of the sample and the absorbance is defined as A(λ)=1- T(λ)-R(λ) [17]. Consequently the IPCE is proportional to the absorbance A(λ). The fraction of the incident photons that are absorbed within the photoactive layer is an unseizable magnitude. In a multilayer system the determination of A(λ) is even more complicated. It can be basically calculated by using the transfer matrix formalism (TMF) by describing the transmission and reflection of the impinging light by the layers of a cell in terms of the optical constant n and k [17]

2.1.3 The photo-electrochemical cells

The best-known wet chemical method to convert sunlight into electrical energy or chemical fuels is represented by the photo-electrochemical (PEC) systems such as an electrochemical photovoltaic (EPV) cell. An EPV system is made of a semiconductor in contact with an electrically conducting liquid, the electrolyte. The electrolyte is able to provide a redox reaction, transferring electrons to an electrode and accepting electrons from another electrode. The semiconductor electrode forms a junction with the liquid and develops an electric field at its surface. The semiconductor can be n-type or p-type. Upon illumination of the semiconductor, the photogenerated electrons and holes can separate because of the surface electric field. For n-type semiconductors, the holes move to the surface and are captured by a redox couple; the electrons move to the back side of the semiconductor, where they leave the cell via an electrical contact, deliver electrical power to an external load, and then return to the cell by means of the second electrode. Here, they are scavenged by the redox species that initially had captured the hole at the semiconductor surface; this process leads the redox species to their original chemical condition. Thus the electrolyte and redox couple are essential to complete the electrical circuit and to guarantee the charge separation. In the next sections we describe in detail the electrochemical cell used to measure the photocurrent response of Ge dot samples (Figure 2.8).

2.2 Sample preparation and characterization

For the synthesis of Ge quantum dots we used silicon (100) substrates covered by a homogeneous 3.0nm thick layer of thermally grown amorphous SiO_2. The SiO_2 surfaces have been cleaned by chemical etching followed by thermal annealing at 700^oC for 30 min in an ultrahigh vacuum chamber (base pressure of about 10^{-10} Torr). Figure 2.3 shows a STM image of clean Si substrate after the thermal treatment. The step structure of Si is clearly visible. On the terraces, typical of Si surface, small bright protrusion 2nm high are present as shown by the STM profile. The protrusions which are the residuals of SiO_2 layer, determine a rough surface of 0.06 nm root mean square (rms) roughness. The protrusions, being points defects of the Si surface could influence the growth of Ge favoring the growth of nano dots instead of a wetting layer.

The Ge atoms have been evaporated using an OMICRON electron gun with a rate of 0.1 nm/min at a pressure of 5×10^{-10} Torr during the deposition. Ge dots have been grown by following a two step process. First, a few nanometers of Ge have been deposited on the clean SiO_2 surface kept at room temperature, then the sample has been annealed in situ at 600^oC for 30 min. Figure 2.4 shows the STM image after four monolayer Ge deposition at room temperature (on the left) and after the annealing treatments (right side). After Ge deposition full coverage of the SiO_2 surface has been achieved and randomly distributed, strictly interconnected Ge amorphous clusters have been formed with a rms roughness of 0.27 nm and a density of about $4 \times 10^{-12}\ cm^{-2}$. Subsequent heating at 600^oC changed the surface morphology, giving rise to individually separated Ge dots with a density of $3 - 4 \times 10^{-12} cm^{-2}$. Such a

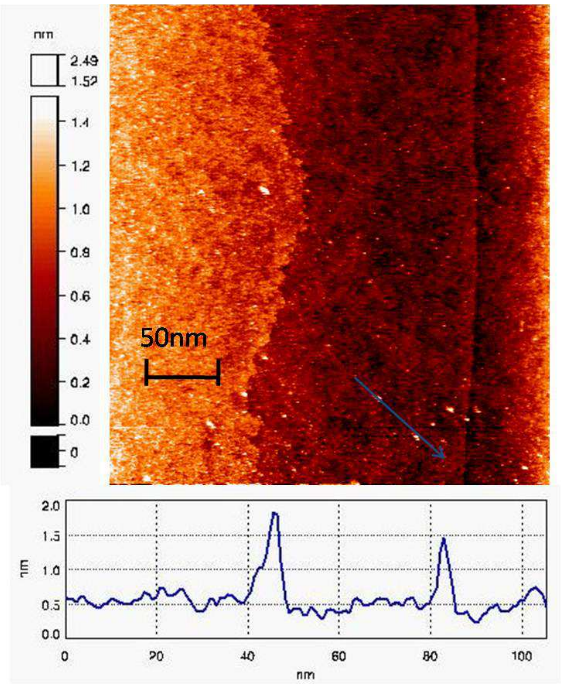

Figure 2.3: *a)STM image of the* $SiO_2/Si(100)$ *substrate after the annealing treatment at* 700^oC *for 30 min, and sectional line profile taken along the blue arrow.*

value is approximately the same as that reported for Ge dots grown on SiO_2/Si(111) surfaces kept at 670^oC [18] but pretty higher than that found for Ge dots deposited on clean and/or lithographically patterned Si surface [18]. The Ge dot average lateral size is 5±1 nm. By collecting several images on different sample areas, it has been possible to figure out that Ge dots uniformly grow on the oxide substrate and appear mainly circular in shape. The average dimensions of the dots have been evaluated from a statistical analysis performed on many STM images. We found that the square root of Ge nominal thickness θ_{Ge} and the average size of the obtained dot after the annealing procedure differ by a factor of 10. As an example, the STM image in Figure 2.4, obtained on a sample with θGe=0.8 nm, produced dots of 12±4 nm average size. The mechanism of Ge dot formation on a SiO_2 substrate is different from that on Si because it is basically driven by surface diffusion and equilibrium surface morphology. In this case a Volmer-Weber growth of Ge islands is observed without the formation of a wetting layer, thus allowing the nucleation and the growth of higher Ge dot density [20] In this context, a crucial point is the existence of equilibrium shapes of the Ge dots and the presence of voids in the SiO_2 ultra thin film under the Ge dots dictating

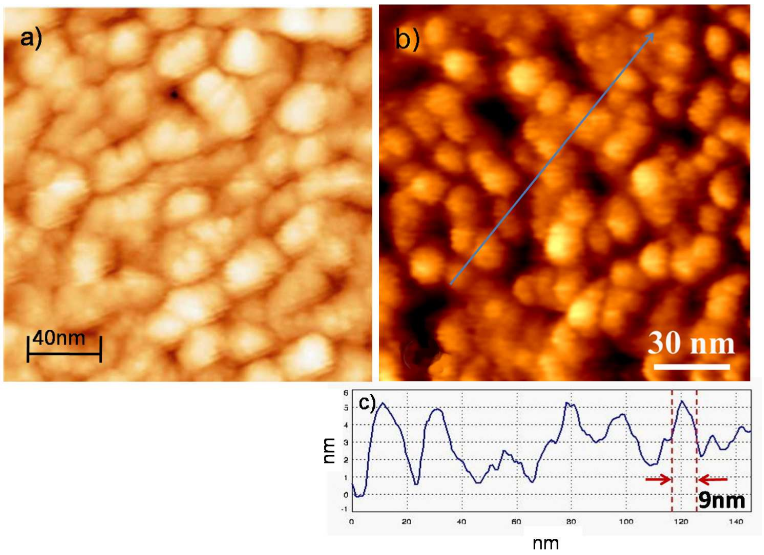

Figure 2.4: *a)STM image of 4 monolayers of Ge deposited on* $SiO_2/Si(001)$ *surface kept at room temperature Vsample=* -3.0 *V, I=*0.5 *nA. b) STM image (150×150 nm*^{2}*) of the 12 nm Ge average diameter after annealing at* 600^oC*. Vsample=*3.5 *V and I=*0.8 *nA. c) Sectional line profile taken along the blue arrow in the image.*

their growth mechanism and crystallinity [14]

X-ray photoelectron spectroscopy (XPS) data were collected with a MAC2 (Riber Instruments) analyzer using non-monochromatized Mg Kα radiation source. XPS data show that both the 3p$_{1/2}$ and 3p$_{3/2}$ Ge features (Figure 2.5 upper part) and the Ge 3d peak (Figure 2.5 lower part) do not exhibit the typical germanium oxide structure located a few eV above the elemental Ge core level, as in the case when Ge dots grow on silicon. This assures us on the absence of any Ge oxide formation during the annealing process necessary to grow the Ge dots, thus confirming that the SiO_2 layer has released no oxygen.

Scanning tunnel spectroscopy (STS) measurements were performed in order to get an evidence of the band gap widening reducing the Ge dot size. Several I-V curves have been recorded by positioning the STM tip on Ge dots of different sizes. Figure 2.6 reports the I-V curves obtained on Ge dots of 8 and 14 nm average size respectively, whereas Figure 2.7 shows the conductance, dI/dV, curves. The measured energy band gap is 1.6 ± 0.1 and 1.0 ± 0.1 eV respectively. The energy band gap as a function of Ge dot size is plotted for Ge dots of different size [1] [15] and shown in the inset of

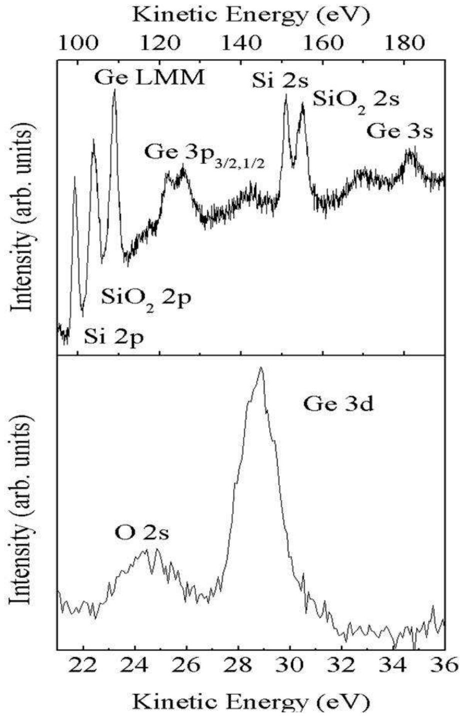

Figure 2.5: *XPS measurements of Ge 3*$p_{1/2}$ *and 3*$p_{3/2}$ *features (upper part) and the Ge 3d peak (lower part) obtained after annealing and crystallization. The spectra do not exhibit the germanium oxide structure located a few eV above the elemental Ge core level [2].*

Figure 2.6. The result is consistent with those reported for smaller Ge nanocrystals grown on SiO2/Si(111) surface [21] and is a further indication that energy band gap widening is an intrinsic property of the Ge dots induced by quantum confinement that changes significantly their electronic band structure as predicted theoretically [4].

2.3 Photocurrent measurements: results and discussion

The photo-conversion efficiency of Ge quantum dots has been evaluated by performing photochemical measurements. The experiments were performed at Science and Chemical Technologies Department of the University of Rome ”Tor Vergata” (laboratory of Prof. M. Venanzi) by using a three electrode chemical cell. Electrochemical cells require at least two electrodes, since the potential of a given electrode can only be

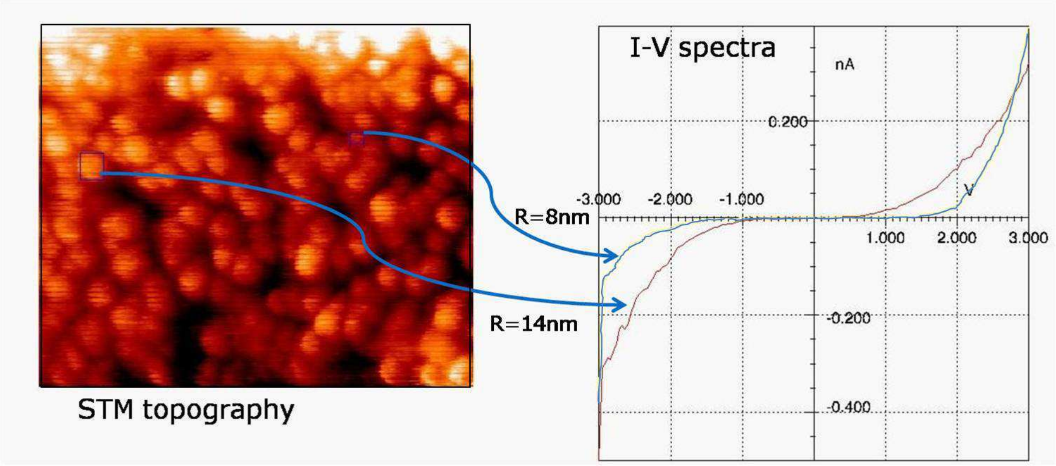

Figure 2.6: *Current-Voltage curves recorded by STM tip on Ge dots of different size, 8 and 14nm in radius respectively.*

measured relatively to another electrode, whose potential must be constant (reference electrode). To measure the current flowing in the cell, a precise control of the external applied voltage is required, but this is generally not possible with a two electrode system, owing to a potential drop across the cell induced by the solution resistance (potential drop is equal to the current times the solution resistance). A better potential control is achieved using a potentiostat and a three electrode system, in which the potential of one electrode (the working electrode) is controlled relatively to the reference one, while the current passes between the working electrode (active or counter electrode) and the third electrode (the auxiliary electrode). The polarization of the counter electrode is required to complete the circuit for current measurements.

Photo-electrochemical measurements were performed by using the Ge dots on SiO_2 sample as working electrode and an AgCl/Ag combined electrode working as reference and auxiliary electrode. The electrolyte was sodium sulphate and the sacrifical electron donor triethanolamine (TEOA) in water. A 200W Xe lamp (Osram) was employed as excitation source ($\lambda > 300nm$). It was equipped with a monochromator to select the incident excitation wavelength and a PG-310 (heka helektronik) potentionstat to measure the generated current. The intensity of the photocurrent signal were normalized to the excited area covered by the Ge dots.

Upon irradiation of the Ge dots with UVVis radiation a photoinduced electron transfer

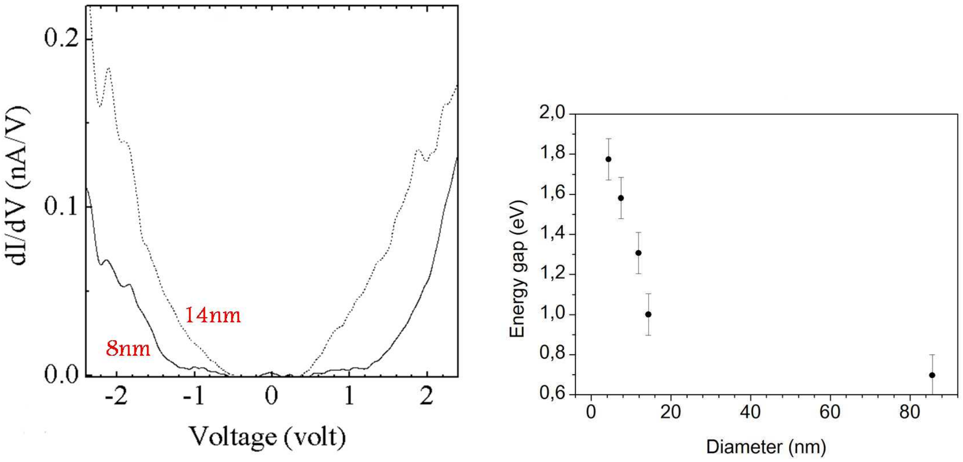

Figure 2.7: *The conductance curves obtained by differentiating the I-V curves recorded on Ge dots of about 8 nm (solid line) and 14 nm (dotted line) in radius (on the left). Energy band gap vs the Ge dot size [1] (on the right).*

from the Ge excited state to the electrode Fermi level primarily takes place. Subsequently, an electron is transferred from the electron donor TEOA molecule to the positively charged Ge group. Hence, the oxidized TEOA rapidly diffuses to the auxiliary electrode, where it takes an electron giving rise to a net anodic electronic current. A sketch of the apparatus, with an illustration of the electron transfer from the photoexcited Ge dots, is reported in Figure 2.8. The photocurrent signal is evidenced by the typical off-on current cycle shown in Figure 2.9.

Figure 2.11(a) shows the photocurrent spectra obtained from Ge dot samples differing in size. The larger dots (85nm) present two main features, located at 4.2 and 2.6 eV. They can be associated with the structures of the optical absorption coefficient reported in Figure 2.11(b). These structures (called E2 and E1 in Figure 2.10) have been interpreted as due to direct electronic interband transitions occurring along X symmetry point and at mid-point between Γ and L of the Ge bulk Brillouin zone, respectively. Reducing the dot size from 85nm to 40nm we obtain the blue shift of the peak at high energy and the reduction of the intensity of the E1 peak. It is worth to note that the photocurrent density for the largest dots is a factor of 5 less than that measured for the 40 nm Ge nanocrystals. This can be ascribed to the lower recombination time present in the larger dots, which hinders the carrier separation, thus reducing the photocurrent intensity. In Figure 2.11(c), we report the photocurrent

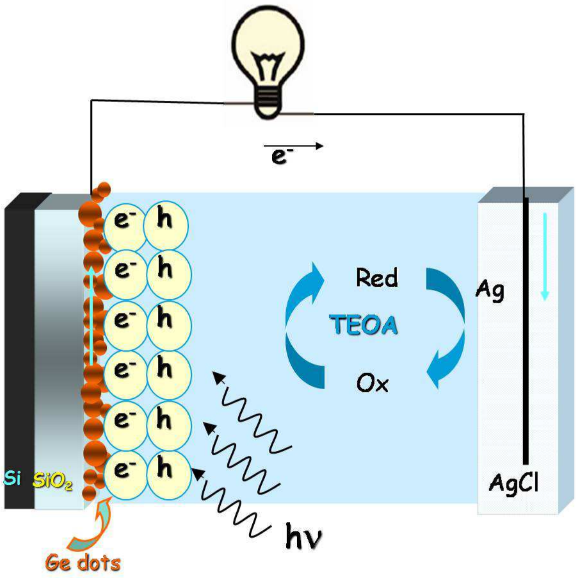

Figure 2.8: *Scheme of the three electrode cell used for the photochemical measurements.*

action spectra of Ge amorphous ultrathin film (open circles) and Ge dots of 5nm (triangles) and 12 nm (black circles) average size. The last sample shows a wide feature in the photocurrent spectrum with a maximum at about 4.35 eV. Also for this sample, the feature can be interpreted in terms of blue shift of the E2 peak. Nothing can be inferred for the lower energy signal due to lack of experimental points. All these results are consistent with optical absorption and ellissometry experiments, reporting a blueshift of the E2 transition and a weakening of the E1 peak by reducing the Ge dot size [22] [23] and have been interpreted as due to quantum confinement effects [24]. Finally, this picture is also supported by calculations of the optical properties of Ge ultrathin films where a blue shift of the optical transitions is reported by decreasing the film thickness [25] In the case of 5 nm Ge dots a broad and intense feature at about 2.4 eV can be observed, while the intensity of the peak at higher energy appears dramatically reduced. This behavior is completely different from those observed with optical measurements [22] and theoretically predicted even for smaller Ge dots [24]. The strong feature could still be ascribed to the E1 transitions, while the observed energy broadening of the peak could be due to the superposition of the contributions to the photocurrent signal coming from the dots of different sizes. However, this interpretation will not explain the E2 peak intensity strong reduction and the E1 feature

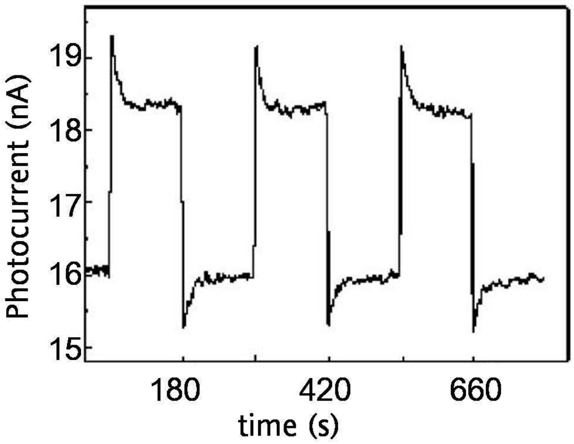

Figure 2.9: *Photocurrent on-off cycles of sample excited with visible light $\lambda = 400nm$ [1].*

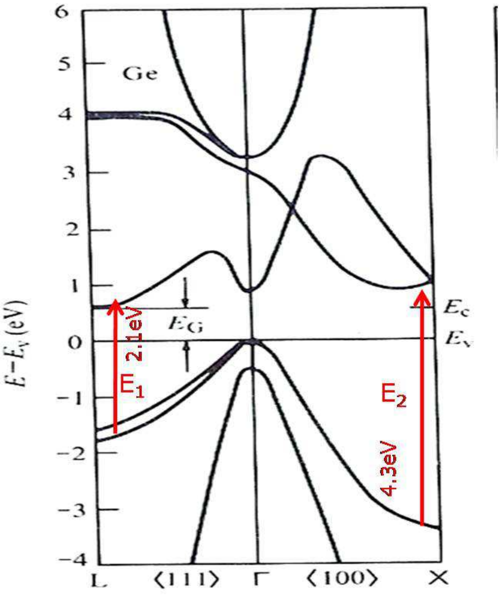

Figure 2.10: *Bulk germanium band structure. E0 and E1 represent the direct electronic interband transitions occurring respectively along X symmetry point and at mid-point between Γ and L of the Brillouin zone.*

small red shift and intensity enhancement. This results could be interpreted as due to an enhancement of the Coulomb-hole attraction [24] of the E1 feature and to exciton longer time of life. This should lead to an increased ability to separate charge carriers before their recombination and to explain the differences among optical and photocur-

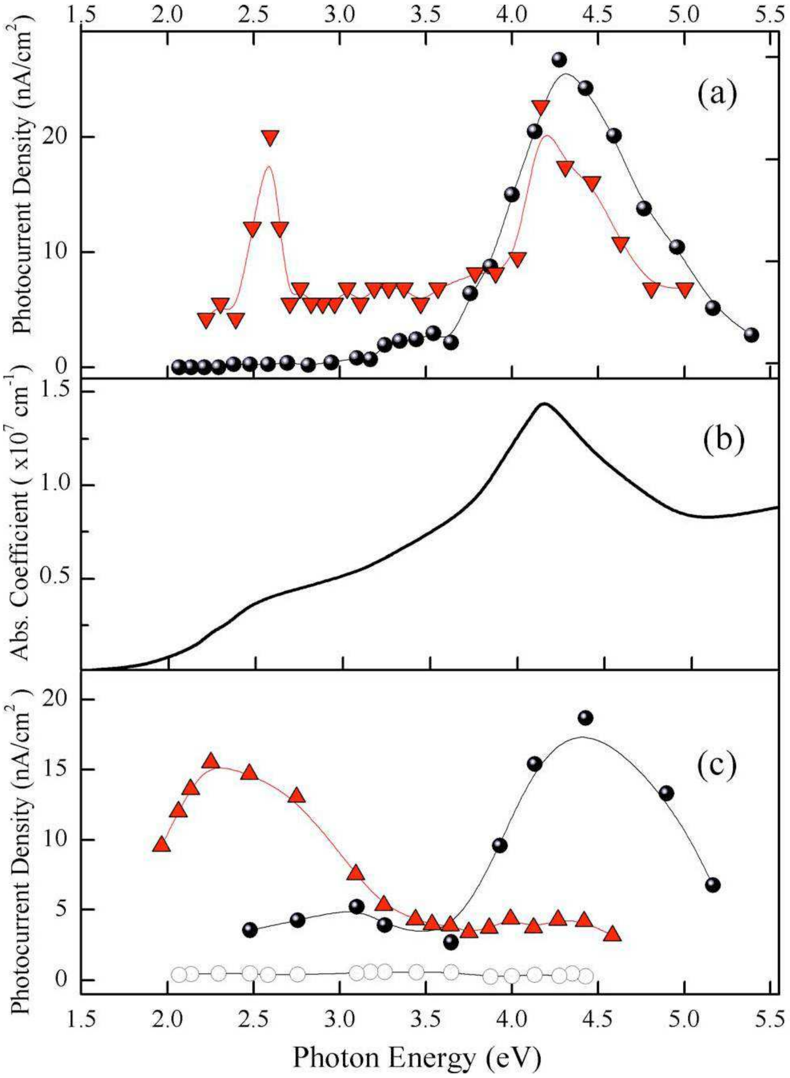

Figure 2.11: *Photocurrent action spectra of (a)85nm Ge dot sample (triangles) and 40 nm Ge dot sample (black circles). The right scale refers to the former sample, while the left scale refers to the latter; (c) 12 nm (black circles) and 5 nm (triangles) Ge nominal thickness samples. The open circles report the photocurrent data for a Ge amorphous ultrathin film [1]. (b) Experimental optical absorption coefficient for Ge bulk [24].*

rent measurements. Moreover, excitonic effect has been reported to play a dramatic role in the imaginary part of the dielectric function for nanometric Ge wires, with the appearance of a strong peak in the visible energy range, in good accordance with the present measurements [26]. Finally, it is worth noting that no photocurrent signal was measured from an ultrathin film of amorphous Ge probably because of short life time of the exciton induced by the large number of defects.

2.4 Conclusions

We have realized Ge dots with high density ($4\times10^{12}cm^{-2}$) on SiO_2. Quantum size effects have been evidenced by I-V measurements by using a STM probe on a single dot. The measurements show the widening of the energy gap into the single and isolated dot (up to 1.8 eV for 5.0 nm sized Ge dots). We demonstrated the ability of Ge quantum dots to generate photocurrent in the near UV and visible range using electrochemical photocurrent measurements. The photogenerated current depends on the excitation wavelength. Moreover by reducing their average dot size a dramatic change in the photocurrent action spectrum occurs due to the quantum confinement effects. Quantum effects enhances the photocurrent yield in the visible range. Our results opens a new issue to Ge for photovoltaic nanodevices and quantum dot based lasers [27] by using the electronic modification occurring in an indirect energy gap material.

Bibliography

[1] M.Scarselli, S.Masala, P.Castrucci, M.De Crescenzi, E.Gatto, M.Venanzi, A.Karmous, P.D.Szkutnik, A.Ronda, I.Berbezier, Appl. Phys. Lett. 91, 1 (2007).

[2] M.DeCrescenzi, M.Scarselli, A.Sgarlata, S.Masala, P.Castrucci, E.Gatto, M.Venanzi, A.Karmous, A.Ronda, P.D.Szkutnik, I.Berbezier, Superlattices and Microstructures, 44, 331 (2008).

[3] T. Takagahara and K. Takeda, Phys. Rev. B 46, 15578 (1992).

[4] C. S. Garoufalis, M. S. Skaperda, and A. D. Zdetsis, J. Phys.: Conf. Ser. 10,97 (2005).

[5] C.Bostedt et al., Appl. Phys. Lett. 84, 4046 (2004).

[6] Y. Maeda, Phys. Rev. B 51, 1658 (1995).

[7] S. Takeoka, M. Fujii, S. Hayashi, and K. Yamamoto, Phys. Rev. B 58, 7921 (1998).

[8] C. Bostedt, T. van Buuren, J. M. Plitzko, T.Mller, L. J. Terminello, J. Phys.: Condens. Matter 15, 1017 (2003); Y. M. Niquet, G. Allen, C. Delerue, and M. Lannoo, Appl.Phys. Lett. 77, 1182, (2000); S. Takeoka, M. Fujii, S. Hayashi,and K. Yamamoto, Phys. Rev. B 58, 7921 (1998); M. Zacharias and P. M. Fauchet, Appl. Phys. Lett. 71, 380 (1997).

[9] K. Brunner, Rep. Prog. Phys. 65, 27 (2002).

[10] A. A. Shklyaev and M. Ichikawa, Surf. Sci. 514, 19 (2002).

[11] S. M. Sze, *Physics of Semiconductor Devices*, 2nd ed. Wiley, New York, (1981).

[12] N. W. Ashcroft and N. D. Mermin, *Solid State Physics* Saunders College Publishing-Harcourt Brace College Publishing,Orlando,Florida, (1976).

[13] S. Miyazaki, H. Nishimura, M. Fukuda, L. Ley, J. Ristein, Appl. Surf. Sci. 113, 585 (1997).

[14] Y. Nakayama, I. Matsuda, S. Hasegawa, and M. Ichigawa, Appl. Phys. Lett. 88, 253102, (2006).

[15] I. Berbezier, A. Karmous, A. Ronda, A. Sgarlata, A. Balzarotti, P. Castrucci, M. Scarselli, and M. De Crescenzi, Appl. Phys. Lett. 89, 063122 (2006).

[16] B.R. Saunders, M.L. Turner, Advances in Colloid and Interface Science 138, 1 (2008).

[17] M. Born, E. Wolf, Pergamon Press, sixth Edition (1980).

[18] A. Barski, M. Derivaz, J. L. Rouvire, and D. Buttard, Appl. Phys. Lett. 77, 3541 (2000).

[19] H. Mathieu, *Physique des semiconducteurs et des composants lectroniques*, 2d Edition, Masson Editor, Paris, (1990).

[20] T. Baron, B. Pelissier, L. Perniola, F. Mazen, J. M. Hartmann, G. Rolland, Appl. Phys. Lett. 83, 1444 (2003).

[21] Y. Nakamura, K. Watanabe, Y. Fukuzawa, M. Ichikawa, Appl. Phys. Lett. 87,133119 (2005).

[22] A. Stella, P. Tognini, C. E. Bottani, P. Milani, P. Cheyssac, R. Kofman, Thin Solid Films 318, 100 (1998).

[23] M. Mansour, A. En. Naciri, L. Johann, S. Duguay, J. J. Grob, M. Stchakovsky, C. Eypert, J. Phys. Chem. Solids 67, 1291 (2006).

[24] M. Palummo, G. Onida, R. Del Sole, Phys. Status Solidi A 175, 23 (1999).

[25] A. N. Kholod, S. Ossicini, V. E. Borisenko, F. Arnaud dAvitaya, Surf. Sci. 527, 30 (2003).

[26] M. Bruno, M. Palummo, S. Ossicini, R. Del Sole, Surf. Sci. 601, 2707 (2007).

[27] V. I. Klimov, A. A. Mikhailovsky, S. Xu, A. Malko, J. A. Hollingsworth, C. A. Leatherdale, H.-J. Eisler, M. G. Bawendi, Science 290, 314 (2000).

Chapter 3

Synthesis of colloidal CdS nanoparticles

3.1 Overview of the chapter

In this chapter, we introduce an important semiconductor material the cadmium sulfide (CdS), describing its most important properties and the most used synthetic routes. We briefly describe the theory of crystal growth in term of a sequence of ideal stages. Following theoretical considerations, we will give a detailed description of the synthetic approach we used to synthesize CdS nanocrystals in colloidal solution, a simple and rapid synthetic route involving only one reagent, a cadmium precursor in a hot non-coordinating solvent. We describe and examine the results of several characterization measurements such as UV-Vis absorption and photoluminescence (PL), Trasmission Electron Microscopy (TEM), Fourier Trasmission Infrared Spectroscopy (FTIR) and Nuclear Magnetic Resonance(NMR). Then we report of the procedure employed to extract the product of the synthesis. A section is dedicated to the Wide Angle X-ray Scattering (WAXS) measurements performed at ESRF Synchrotron Radiation Facility. In that section we describe the WAXS pattern of the samples before and after the extractron treatment and the evolution of WAXS curves during the thermolysis. Finally we describe the method used to deposit the nanocrystals on a substrate and the Atomic Force Microscopy (AFM) analysis performed on such samples. The work of synthesis and characterization of the CdS samples described in this and in the next chapters was performed in the laboratories of ENEA UTTP NANO in Portici (Napoli).

3.2 Introduction

Semiconductor materials are particularly suitable for observation of quantum size effect because they are characterized by relatively small effective masses and large dielectric constants compared to insulators, so the condition $a_B > a_L$ can be easily satisfied [1]. In particular the semiconductors belonging to the II-VI groups like cadmium sulfide (CdS), allows to observe quantum size effect at relatively large nanocrystal size being the exciton Bohr radius of CdS $\sim 50\mathring{A}$ [2]. The cadmium sulfide is a direct band gap semiconductor with energy band gap of 2.42 eV at 300 K. The magnitude of the band gap implies that it macroscopically appears yellow colored. CdS shows dimorphism of cubic form (zinc blend type) and hexagonal form (wurtzite type) [3]. Since the difference in crystalline phase leads to considerable change in the effective masses of electrons and holes in their electronic bands, this peculiarity of CdS influences its optical properties. The hexagonal phase of CdS is thermodynamically-controlled (stable) as compared to the cubic phase which is kinetically-controlled (metastable) [4]. In both phases the cadmium and sulfur atoms are four coordinate.

Figure 3.1 shows the theoretical band structure diagram of CdS in the hexagonal phase [5]. It is an anisotropic plot of the eigenvalue spectrum E as a function of k, the crystal wave vector. The position Γ corresponds to k=0, the Brillouin zone center. The point L refers to the Brillouin zone where k is larger, on one order of magnitude of π/a_0 where a_0 is the lattice parameter [8]. In bulk crystals the different regions of Figure 3.1 contribute to different region of the optical spectrum. The Γ region is related to the band gap of the CdS (in the hexagonal phase and at room temperature) at $2.42eV$ (512nm). In this region (E_0 that is the lowest transition between the 1S electron state and the 1S hole state [7]) the conduction and valence band are parabolic and the effective mass of charges are independent of k. The L region (E_1) contributes with transition at $5.30eV$ (240nm), other transitions occur at higher energies ($\geq$ 6.4eV) [8]. It has been demonstrated experimentally by optical analysis that E_0 is strongly affected by size while E_1 is unaffected [9].

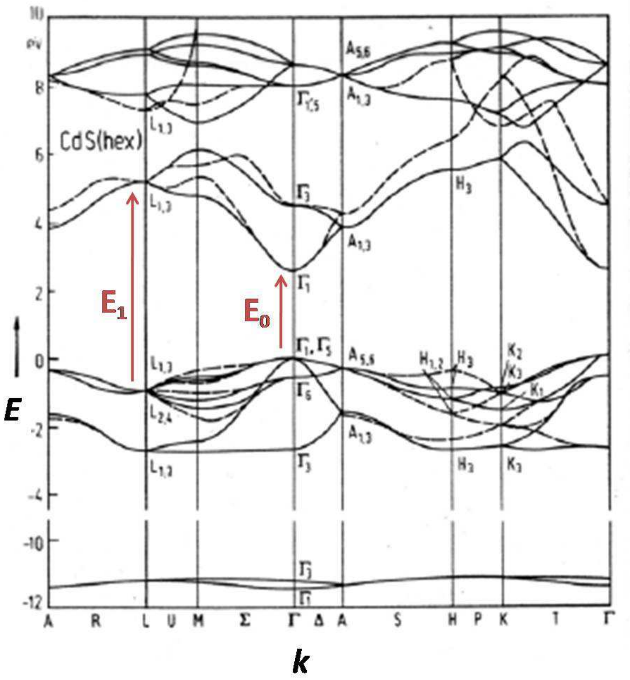

Figure 3.1: *Theoretical band structure diagram of bulk CdS in its hexagonal phase [5] with indication of the first two direct transition energy* E_0 *and* E_1.

3.2.1 The theory of crystal growth

In the theory of crystal growth, the formation of a crystal results from the phase transition in a supersaturated viscous medium. This condition is realized when in a given reaction environment (for instance in a solution) the concentration of reactants is progressively increased by some means passing a concentration threshold, called critical supersaturation. At this point the system become unstable and the process is controlled by diffusion of ions dissolved in solution or in the matrix.

The diffusion-controlled growth from a supersaturated solution can be described in terms of the following idealized stages.

Nucleation . At the first stage of a system at critical supersaturation the reactants in the unstable system tend to form nuclei. At the nucleation stage the concentration of ions can be treated as constant and the time dependence of the cluster size and thus the growth law takes a parabolic form.

Normal growth . At the second stage, the nuclei grow at the expense of the monomer species and the small nanocrystals exhibit a monotonic growth. At this stage the supersaturated phase decreases with time.

Competitive growth . The final stage is realized when the crystallite are big enough and almost all the ions of the supersaturated solution are incorporated in the crystallites. This stage is also called "Ostwald ripening" or diffusion limited aggregation or coalescence. At this stage smaller crystals start shrinking while the larger ones are still growing. The formation of larger crystals is favored by the dissolution of small crystals which provide new monomers and allow the crystallites to grow further. A critical radius,r_{crit} separates crystallites which can experience either further growth or dissolution. The critical radius depends essentially on the monomer concentration. If the monomer concentration is low, the critical radius is large. This means that only crystals larger than this size will be stable in solution and will continue to grow. Smaller crystal will be unstable and will have a tendency to dissolve becoming increasingly unstable. The mass transfer from smaller crystallites to the bigger ones is favored by the surface tension since a decrease in the crystallite-matrix surface gives rise to a decrease in the free energy of the system.

Over time the supersaturation become negligible and the total mass of the semiconductor phase is considered constant.

To estimate the time dependence of the mean particle radius, we define $\triangle r$ as the difference between the largest and the smallest size(r_1,r_2)present in the growing medium. Assuming that r_{crit} is constant (i.e. no variation in the monomer concentration with time), the variation of $\triangle r$ with time is approximated as:

$$\frac{d\triangle r}{dt} = \frac{K_D \triangle r}{\overline{r}^2}\{\frac{2}{\overline{r}} - \frac{1}{r_{crit}}\} \tag{3.1}$$

where $\overline{r}=\sqrt{r_1 r_2}$ is the mean radius. For $\overline{r}/r_{crit} < 2$, the size distribution broadens with time because larger particles grow faster than smaller ones, whereas for $\overline{r}/r_{crit} > 2$ the size distribution narrows with time because smaller particles grow faster than bigger particles.

All those statements are valid under the assumption that the particles are spherical and that an averaged surface tension can be defined. Actually the growth of crystals depends on a number of parameters, such as surface energy, concentration of reactants in solution, crystal size. In real system various stages may coexist and, the normal growth can occur along with the increase of number of crystallites because of ongoing nucleation process.

The three stages are characterized by different activation energies, therefore choosing properly the growth parameters such as the temperature and time it is possible to obtain nanocrystals which have experienced different growth conditions. In particular low temperature and long time is a combination that generally allows the nucleation at extremely small size. On the other hand high temperature combined with short time usually give rise to a rapid increase in size while the number of nanocrystals remains constant. The combination of these two steps can provide a good control of size, size distribution and concentration of nanocrystals.

However the most used procedures to obtain uniform size nanocrystals in quantum confinement regime involve the use of terminating or stabilizing agents like reverse micelles, polymers, thiols and various coordinating solvents. The role of stabilizers is to interact with the particle surface, preventing it from growing fast and from collapsing on another particle, in other words they prevent agglomeration and ensure stability in solution, slow growth and further processability of the nanocrystals.

3.2.2 A brief overview of methods for the synthesis of CdS nanoparticles

The nanoparticle size selectivity and the narrow size distribution are among the main critical issues for the fabrication of nanoparticles. Moreover we have to consider that at the surface of a pure semiconductor, substantial reconstruction at the atomic positions occurs, and energy levels within the energetically forbidden gap of the solid can exist. These surface states act as traps for electrons and holes and manifest themselves as a degradation of the electrical and optical properties of the material. As a consequence a sort of ”passivation” by chemical process is generally needed in order to eliminate the energy levels inside the gap. The passivation process is also requested to favor the solubility of nanoparticles in colloidal suspension, and to enhancing functionality of nanocrystals in different application contexts.

Several technologies have been developed for synthesizing CdS nanoparticles. They differ in the synthesis environment (organic or inorganic matrix, liquid solutions or polymers), in the growth conditions, size range, and size distribution, as well as in the physical and chemical stability and reliability.

One of the first proposed synthetic route to obtain size controlled nanocrystals was that of so called inverse micelles [10], while the most widely used method is the pyrolysis of an organometallic complex containing both metal and elemental sulfur [11],[12],[10]. According to this method the tri-octyl phosphine (TOP) is usually used to dissolve the sulfur and tri-octyl phosphine oxide (TOPO) is employed as coordinating solvent. This method was generally used in mass production of nanoparticles. Oleic acid is generally adopted as a safer and simpler alternative to TOPO. It is used along with a non coordinating solvent like octadecene [13]. Moreover recent advances in colloidal preparation of II-VI nanoparticles in non coordinating solvent have demonstrated that varying the reactants/ligand ratio a formidable control of the size and size distribution of CdS nanoparticles with high quality optical properties can be obtained [14].

Beyond these techniques which employ organic solvents, there is the aqueous solution synthesis [15], It is a very challenging route, necessary for many biological applications. The peculiarity of all the mentioned chemical methods consists in the fact that they produce nanocrystals that can be further processed and manipulated. After the synthesis they can be attached to a variety of molecules via metal coordinating functional groups, such as thiol, amine, nitrile, phosphine, phosphine oxide, phosphonic acid, carboxylic acid or others. By bonding appropriate molecules to the surface, nanocrystals can be dispersed in a variety of solvents, embedded in a polymeric matrix, immobilized on a metal, integrated into electrical circuits. However, the colloidal methods have some drawbacks, for instance the use of highly reactive reagents, the difficulty to get reproducibility in the crystal growth and to handle some reagents which are toxic and very sensitive to oxygen.

Among the several techniques used to growth CdS nanocrystals, the synthesis in a polymer (*in-situ*) has been playing a fundamental role in the development of advanced functional materials. This approach consists of dissolving molecular precursor (such as $Cd_{10}S_4(C_6H_5)_{12}$ or $CdCl_2$) in the polymer and then treating with H_2S gas or adding Na_2S [16]. An alternative approach is the simultaneous polymerization and synthesis of nanocrystals. In some cases mixture of CdS precursor and polymer monomer are thermally treated by microwave radiation [17]. In other cases the polimerization-reduction method was adopted using CO_2 as antisolvent to precipitate both the CdS nanoparticles and the polymer after synthesis.[18] Using the *in-situ* route we can take advantage of the polymer as both stabilizer and matrix. Moreover this method allows the synthesis of nanocrystals with well defined and controllable surface structure and low defect concentration because the temperature of synthesis is limited by the thermal properties of the polymer and cannot go beyond 300^oC in most cases. One more important advantage of the *in-situ* approach is the prevention of nanocrystals aggregation and degradation [19] [20].

The *in-situ* technique can be considered a simple approach to realize CdS based nanocomposites. In many cases it is a valid alternative to the *ex-situ* method which consists in mixing nanocrystals and polymer after their synthesis. In the *ex-situ* method the transfer and dispersion of the nanocrystals in the polymer may represent a critical step and can invalidate the functional properties of the nanocomposites [21].

3.3 Sample preparation

The synthesis of colloidal CdS nanocrystals described in this chapter is based on the thermolysis of an alkanethiolate of Cadmium. Alkanethiolates of transition metals (i.e. $Me_x(SC_nH_{2n+1})_y$ with $n = 7, 12$) are organic compounds characterized by a combination of chemical and physical properties that make them ideal for the generation of nanosized metal or metal sulfide inclusions in polymers. In particular, these compounds have an amphiphilic nature because the metal atom is bound to one or more sulfur atoms through a polar-covalent bond. However, since the ionic contribution to the metal-S bond is low, the presence of long chain alkyl groups gives a hydrophobic character to the molecule, making possible dissolution in non-polar organic solvents (e.g., hydrocarbons, ethers, chlorinated solvents, etc.). As a consequence, these compounds are compatible with hydrophobic polymers and can give homogeneous solid solutions.

Metal sulfur bond energies are usually low $(200 - 400 kJmol^{-1})^{10}$. These compounds are very stable at room temperature and they can be handled and stored without special care.

The Cadmium precursor was synthesized in the laboratories of ENEA C.R. Brindisi. It was obtained by reaction of cadmium nitrate and dodecanethiol in ethanol as reported in the following equation 3.3 [22]

$$Cd(NO)_3 + 2RSH \longrightarrow Cd(SR)_2 \tag{3.2}$$

$$R = -(CH_2)_{11}CH_3 \tag{3.3}$$

Since the metal-sulfur bond energies is higher than the sulfur carbon bond energy $(714.1 kJmol^{-1})$, the thermal decomposition of the precursor molecule usually leads to the production of metal sulfides according to the following reaction scheme:

$$Cd(SR)_2 \rightarrow CdS + RSR \tag{3.4}$$

At high temperature further decomposition of the products (Eq. 3.4) can occur producing metal and sulfur atoms.

Thermogravimetrical Analysis (TGA) and Differential Scanning Calorimetry (DSC) on the Cd bis-thiolate precursor were carried out by Jupiter $TA - 2590$ and a Mettler DSC 822E instrument respectively in order to know the temperature required for the thermolysis of the thiolate compounds. The thermal analysis experiments were performed in a dynamic nitrogen atmosphere on the original $Cd(SR)_2$ powder using a sample weight of about 15 mg in aluminum crucibles, from RT to 400 at $10^oC/min$. TGA and DSC curves are reported in Figure 3.2 and 3.3

The DSC measurements show an endothermic peak at about 125^oC ascribed to the melting of the precursor because no mass loss is observed in the TGA curve in the same range [22]. As shown by TGA curve, the thermal decomposition of $Cd(SR)_2$ under nitrogen flux starts at about 200^oC with a total mass loss of 70% at 370^oC. The TGA curve shows also a complex process of decomposition occurring in numerous, less

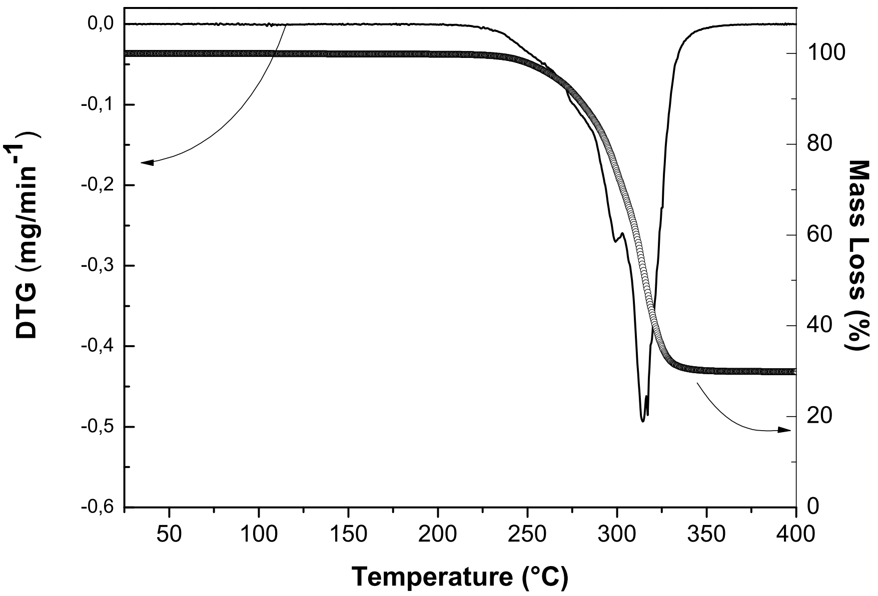

Figure 3.2: *Thermal analysis (TGA and DTG curves) of the Cd precursor* $Cd(SR)_2$*. The mass loss starts at about* 200^oC *and is almost complete at* 350^oC *with 30% of residuals.*

marked steps that are clearly enhanced in the derivative TGA curve (DTG) (Figure 3.2). The peaks of this curve correspond to the more complex pattern on the DSC curve observed in the same temperature range (Figure 3.3). In the range 300-365^oC almost all the $Cd(SR)_2$ is decomposed.

The CdS nanocrystals were synthesized in 1-Octadecene (ODE, Alfa Aesar 90%). ODE is characterized by the following molecular formula:

$$CH_2 = CH(CH_2)_{15}CH_3. \tag{3.5}$$

It is a high boiling point solvent (Tb$\sim$ 315^oC) and is non coordinating for CdS, for these reasons it is widely used as solvent for the nanoparticle synthesis.

We proceeded in the sysnthesis as follows. We dissolved the Cd bis-thiolate precursor, $Cd(SR)_2$, in octadecene in a three necked round bottom flask equipped with a thermometer to measure the inner temperature of the solution and a threaded plud to inject inert gas (nitrogen or helium). Due to precursor insolubility in many organic solvent the solution of octadecene containing the thiolate precursor needed to be heated up to allow the complete solubilization of the precursor. For this reason the solution was kept under stirring on hot plate (FALC F 90 T). After the solubilization

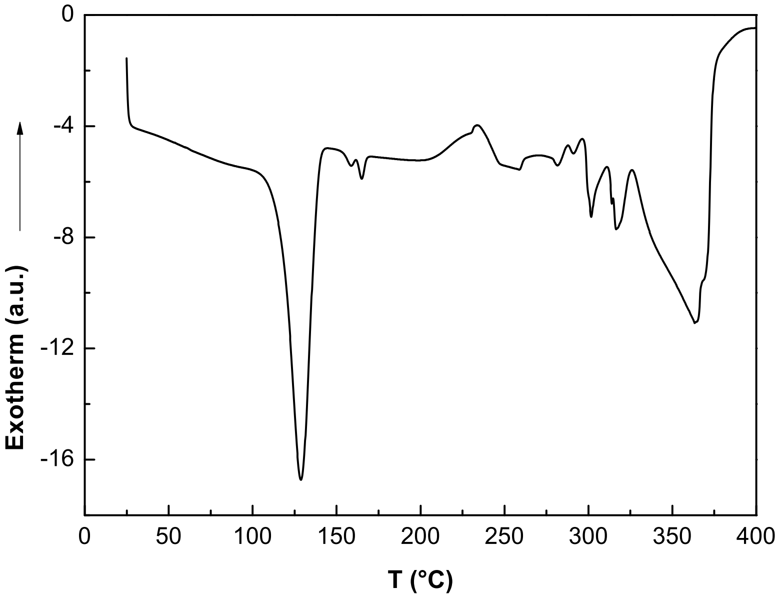

Figure 3.3: *Differential scanning calorimetry (DSC) scan of* $Cd(SR)_2$ *showing that the melting point is at* 128^oC *and the decomposition process start at about* 200^oC.

at about 120^{o}C the precursor decomposed and the first nuclei of CdS formed together with residual organic complexes. The starting white opalescent solution became a yellow colored solution indicating the formation of CdS nanocrystals. The reaction was stopped by removing the flask from the hot plate and cooling down at room temperature.

The synthesis was carried out in different conditions in order to study the influence of both precursor/solvent concentration and annealing conditions on the nanocrystal formation.

The first set of samples were prepared by fixing the precursor/solvent concentration at $10mmol$ and varying the final annealing temperature (T_f), the time at T_f and the annealing rate (Table 3.1). Another set of samples were prepared at lower precursor/solvent concentration, 3mmol. The annealing conditions for each sample are shown in Table 3.2. In all the investigated cases, the we took notes of three steps: the complete solubilization of precursor, the vapor emission and the temperature at which the solution started to appear colored. We noticed that no substantial change

sample	Tf(^oC)	rate ($^oCmin^{-1}$)	t_{Tf}(min)	Eg(eV)	R(nm)
CdSODEHe1	200	5	1	3.90	1.28
CdSODEHe2	200	5	30	-	-
CdSODEHe3	200	5	60	-	-
CdSODEHe5	240	10	1	-	-
CdSODEHe6	240	10	30	3.75	1.30

Table 3.1: *CdS nanocrystal samples synthesized at* $10mmol$ *with indication of the band gap, Eg, and the radius, R, calculated from the absorption spectra.*

sample	Tf(^oC)	rate ($^oCmin^{-1}$)	t_{Tf}(min)	Eg(eV)	R(nm)
CdSODEr1	200	10	1	3.11	1.60
CdSODEr2	190	5	1	3.22	1.49
CdSODEr3	200	5	1	2.75	2.32
CdSODE9	240	10^o/min	1	-	-

Table 3.2: *CdS nanocrystals samples synthesized at* $3mmol$. *The band gap, Eg, and the radius, R, are calculated from the absorption spectra.*

of first two parameters occurred varying the annealing conditions. In fact in all cases the solution appeared completely transparent at about 120^{o}C and the gas emission that represents the starting point of nucleation according to relation 3.4, was observed in the range $170^oC - 180^oC$. The nucleation phase was followed by the change of color. The coloring phase, representative of the growing stage, started in the range $180 - 200^oC$ depending on the annealing conditions. Since the synthesis process was relatively rapid we couldn't distinguish between the normal and the competitive growth regime. However we noticed that longer annealing time produced darker solution.

We attempted to synthesize CdS nanocrystals by using Cd precursor molecules of different chain length in particular using molecules with 7 instead of 12 carbon atoms. The decomposition of thiols occurred faster than in the previous case and induced the formation of agglomerates which precipitated from the reaction medium. As a consequence we preferred the use long chain thiols which allow a more controlled synthesis of the nanocrystals [23].

3.3.1 Extraction procedures

After the synthesis the nanocrystals were extracted from ODE according to two different procedures:

1. An excess of acetone/ethanol 1/1 mole ratio was added to the as prepared solution and flocculant precipitate formed. The precipitate was separated by centrifugation (10000 rpm for 10 min) and rinsed three times by ethanol. Finally the extracted yellow nanocrystals were dispersed in a small amount of acetone and evaporated to dryness at 50^oC under vacuum.
2. As an alternative procedure an excess of methanol was added to the nanocrystals in ODE and centrifuged at 10000 rpm for 10 minutes, then the yellow solid part was rinsed and centrifuged several times in hexane to remove the excess of surfactant. Finally the residual of solvents evaporated under vacuum as in the previous procedure.

The second procedure had the advantage to provide well dryed nanocrystals powder because the organic solvent used during the rinsing procedure avoided the aggregation of the nanocrystals as confirmed by different subsequent analysis.

3.4 Characterizations

- *UV-Vis Absorption Spectroscopy.*

  The synthesis of CdS nanoparticles was monitored by UV-visible absorption measurements by dispersing few μL of solution were dispersed in ODE. The measurements were recorded in a quartz cuvette by a Perkin Elmer Lambda 900 spectrophotometer in the range $200 - 800$nm.

- *Photoluminescence spectroscopy (PL)* .

  PL measurements were recorded at room temperature using a Fluorolog 3 spectrometer (Jobin Yvon Horiba, Instruments SA) equipped with a 450W Xe Lamp as excitation source, double monochromators for excitation and emission, and a Hamamatsu R928P photomultiplier tube as detector. The sensibility was 4000:1

as evaluated by the ratio signal/noise of the Raman spectra of water. Observed luminescence spectra were corrected for the nonlinear response of the instrument using predetermined correction factors. Photoirradiations were conducted within the sample chamber of the emission spectrometer. The excitation wavelength was selected to correspond to the absorption-band maximum, and the samples were irradiated with a band-pass of 5 nm.

- *Trasmission Electron Microscopy (TEM).*

  The nanoparticle morphology was studied in detail by TECNAI G2 F30 microscope operating at 300kV with spatial resolution of 0.205nm. The TEM measurements were carried on in collaboration with the Electron Transmission Microscopy Laboratory of ENEA C.R. Brindisi. The samples were prepared by dropping few μL of a solution of nanoparticles in toluene on carbon coated copper grid, allowing the solvent to evaporate. Bright (BF), high resolution (HTEM) was used in order to evaluate the particle shape and the crystal structure and the diameter distribution. Moreover we used the scanning TEM (STEM) in dark field (HAADF) to scan the sample surface and an energy dispersive spectrometry (EDS) probe to collect the X-rays emitted from a single nanoparticles.

- *Nuclear Magnetic Resonance(NMR).*

  NMR patterns were recorded in the Chemistry department of University of Napoli "Federico II" by a 400MHz Bruker spectrometer. We measured the samples after the extraction by solution state $1H-NMR$ in chloroform, $CHCl_3$, in order to investigate the chemical environment of the nanoparticles surface.

- *Fourier Transform Infrared Spectroscopy (FT-IR).*

  Further information about the sample composition and the chemical environment of nanoparticles were obtained by FT-IR patterns recorded by IR Nicolet 5700 FTIR on solid .

- *Atomic Force Microscopy (AFM).*

  The morphology of the nanocrystals was assessed by AFM analysis on films deposited on silicon and MICA substrates. The AFM was used in tapping mode by IV Dimension Digital Instruments Veeco.

- *Wide Angle X-ray Scattering (WAXS).*

  WAXS experiments were performed at ESRF synchrotron radiation facility to investigate the crystalline structure and the size CdS anoparticles. The details of the experiments and the results are discussed in a separate section at the end of this chapter.n a separate sections we comment the results obtained

3.5 Results and discussion

UV-Vis Absorption Spectroscopy.

Each sample was first characterized by UV-Vis absorption spectroscopy to get an immediate proof of the quality of the nanoparticles. Absorption spectroscopy is a routinely technique that allows to distinguish between bulk and quantum confined systems. Before describing the results we remind some important concepts related to the interpretation of absorption data. The optical absorption cross section of a system of small particles in an homogeneous medium is given by the $Mie's$ theory under the assumption that the particles are describable by their bulk optical dielectric functions. In general, the solutions to Maxwells equations yield an expression for the absorption cross section, which is a sum over electric and magnetic multipoles. When the size of a particle is much smaller than the wavelength of the exciting radiation, the absorption is dominated by the dipole term, with a cross section $\sigma(\omega)$ given by [24]

$$\sigma(\omega) = 9(\varepsilon_m)^{3/2} V_0 \frac{\omega}{c} \frac{\varepsilon_2(\omega)}{[\varepsilon_1(\omega) + 2\varepsilon_m]^2 + (\varepsilon_2(\omega))^2} \tag{3.6}$$

where ω is the frequency, c is the speed of light, ε_m is the dielectric constant of the embedding material, V_0 is the volume of the particle, $\varepsilon_1(\omega)$ and $\varepsilon_2(\omega)$ are the real and the imaginary part of the frequency-dependent dielectric constant of absorbing solid, $\varepsilon(\omega)$. For a sample of dilute (non-interacting) absorbers of number density n and path length l_0, $\sigma(\omega)$ is related to the conventional absorbance through the relation

$$A(\omega) = \frac{n\sigma(\omega) l_0}{ln(10)} \tag{3.7}$$

The shape and the absolute magnitude of $\sigma(\omega)$ (thus of A(ω)) are fixed by ε that is the ratio of the dielectric complex coefficient of the crystal bulk $\varepsilon_2(\omega)$ respect to the real dielectric coefficient of the transparent solvent ε_m. Figure 3.4 shows the plot of ε

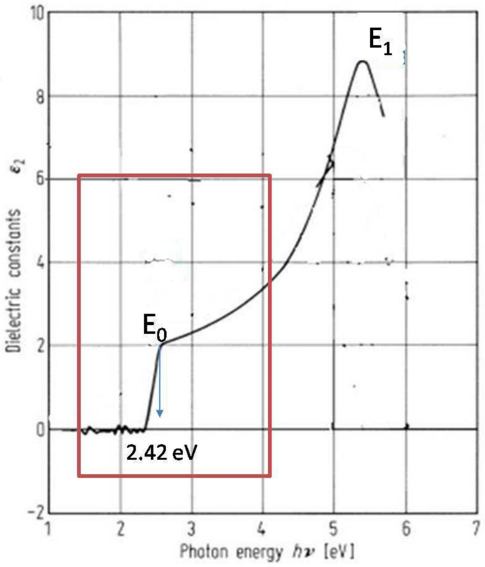

Figure 3.4: *Dielectric complex coefficient of bulk CdS with indication of two allowed energy transitions, E0 and E1. The first corresponds to the* $1S_e - 1S_h$ *and determines the band gap of CdS ([5]).*

as function of energy calculated for bulk CdS in the hexagonal phase. We indicate as E_0 and E_1 the principal band transitions as reported in Chapter 1. Such plot as been used as reference to valuate the size dependent variation in the experimental absorption spectra. For semiconductors in the case for energies less than the band gap $\varepsilon^{'}(\omega)$ is real as a consequence the $\sigma(\omega)$ is expected to be zero. The main evidences of size variation are expected to occur at the band gap. The absorption threshold (i.e. the lowest excited state) shifts toward higher energy (blue-shift) with respect to the bulk showing an intense peak due to the discrete electron-hole states for small crystallites according to the strong confinement model ($a_L \ll a_B$)[1][6][25]. For crystallites belonging to the weak confinement model (a_L is small but still larger than a_B, in other words for CdS crystallites larger than 10nm) the $\sigma(\omega)$ shows almost bulk like behavior but slightly blue-shifted.

Figure 3.5 shows the absorption spectra of samples CdSODEHe1, CdSODEHe3 and CdSODEHe6. The sample annealed at 200^oC for 1min (CdSODEHe1) shows two weak shoulder at about $2.5eV$ and $3.2eV$. The absorption curve of the sample after annealing for 60min at the same temperature (CdSODEHe3), shows a bulk behavior with a pronounced peak at $2.42eV$. On the other hand the sample annealed at 240^oC

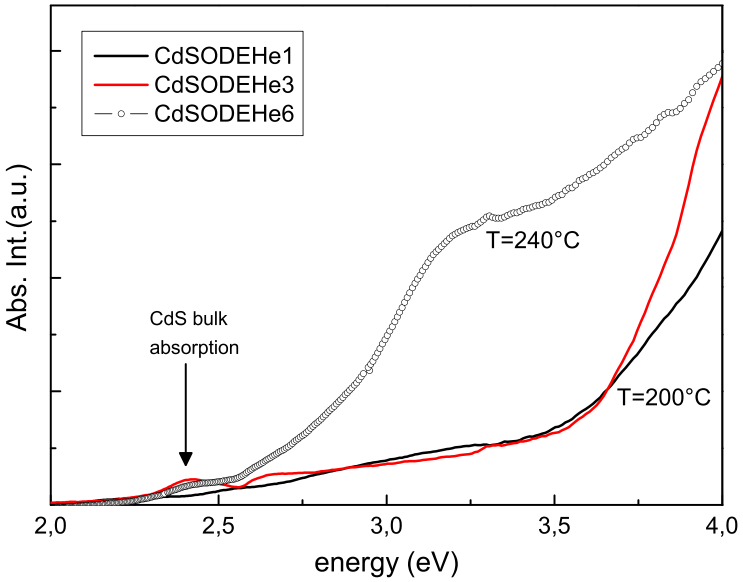

Figure 3.5: *Absorption spectrum of samples (precursor concentration 10mmol) prepared at different annealing temperatures (CdSODEHe1, CdSODEHe6) and different annealing time (CdSODEHe1, CdSODEhe3). The energy position of the CdS bulk absorption is indicated by the arrow.*

for 30min, (CdSODEHe6), presents a typical absorption spectrum of quantized structure with an evident band centered at about $3.2eV$. This results demonstrates that keeping the annealing condition of sample CdSODEHe1 for 1min is not enough for nanocrystals to form or a very little amount is formed. Extending the annealing time to 30min leads to the coalescence of nanoparticles in the colloidal solution. This is probably due to the low concentration of monomer in solution because of the low annealing temperature. Moreover, since the annealing rate is relatively low, the process of aggregation is more rapid than the formation of new monomers in solution. The comparison between the absorption curve of sample CdSODEHe1 and CdSODEHe6 indicate that the nanocrystals grow with annealing time suggesting that at higher temperature and rate of $10^{o}C/min$ the coalescence process is limited and a more controlled growth is favored.

The absorption curves of samples at precursor/solvent concentration of 3mmol, are shown in Figure 3.6. These samples are characterized by different behavior compared

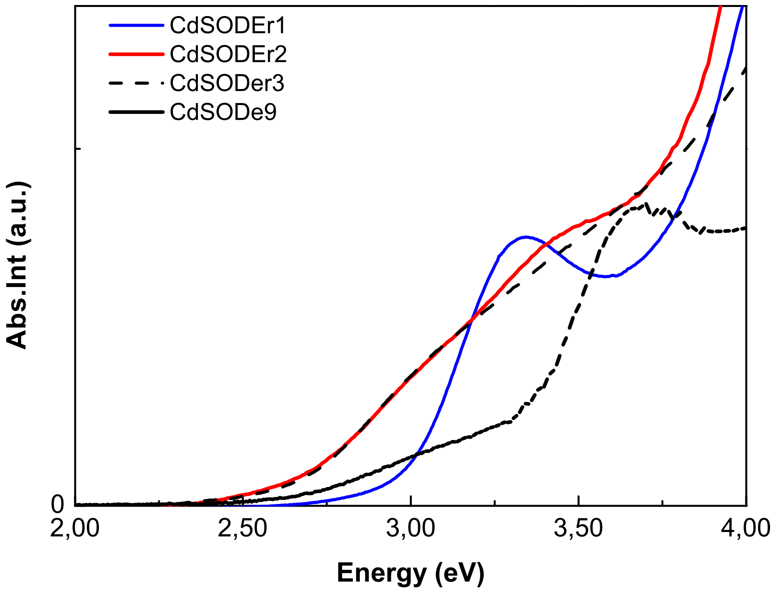

Figure 3.6: *Absorption spectra of sample prepared with 3mmol of Cd precursor.*

to the previous set of samples investigated. In particular the samples CdSODEr2 and CdSODEr3 show weak absorption features with maximum at 3.0 and 3.5eV respectively, while the sample that was processed at higher annealing rate, CdSODEr1, is characterized by a sharp excitonic peak, the absorption onset is blue shifted with respect to the other curves and is smaller than the bulk excitonic onset of cadmium sulfide by 0.2eV. Considering that the absolute value of the onset shift is one order of magnitude larger than the exciton Rydberg energy (that is 0.03eV for CdS) we conclude that the nanocrystals of sample CdSODEr1 fall in the strong confinement regime[1]. Moreover these nanocrystals are characterized by nearly narrow size distribution as indicated by the width of the peak.

The sample CdSODE9 shows an intermediate behavior between the samples CdSODEr1 and CdSODEr2, thus between weak and strong confinement limit. Its spectrum develops into two wide bands slightly shifted with respect to the bulk. From these analysis it is evident that the nanocrystals are already formed at 200^oC at low precursor concentration. If we raise the precursor feed, higher temperature and high annealing rate become a crucial factor to grow nearly monodispersed nanocrystals.

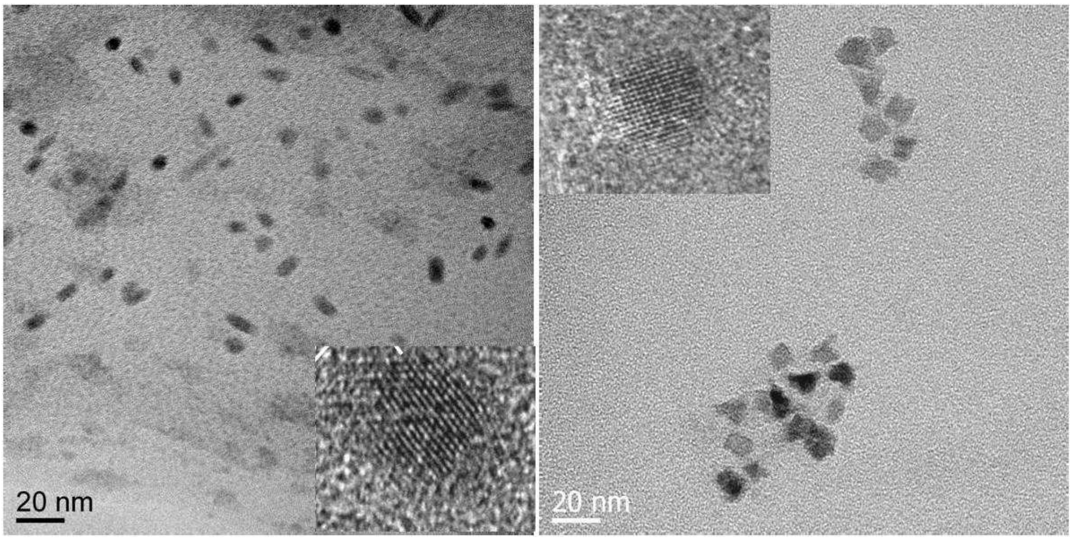

Figure 3.7: *Bright TEM images of samples CdSODEr1 (on the left) and CdSODE9 (on the right). In the inset the HRTEM images taken on single nanocrystals and showing the presence of lattice fringes in both cases.*

Given the threshold wavelength it is possible to estimate the crystal size according to the Brus equation [6]. We estimated the nanocrystals size of all samples from the absorption data by calculating the energy gap Eg^{nano} and the radius R of the nanocrystals (Table 3.1 3.2) through the relation 3.8:

$$\Delta Eg^{nano} = Eg^{nano} - Eg^{bulk} = \frac{h^2}{8MR^2} \tag{3.8}$$

where M=m_e+m_h and m_e and m_h are the electron and the hole effective mass. Eg^{nano} was obtained by fitting the direct transition by the following equation 3.9 [27]:

$$\alpha h\nu = A(h\nu - Eg^{nano})^n \tag{3.9}$$

where $h\nu$ is the photon energy, α is the absorption coefficient, A is a constant and n is equal to $\frac{1}{2}$ for direct band gap [28].

TEM analysis.

The left side of Figure 3.7 shows a bright field image of the sample CdSODEr1. On the right side the corresponding image of sample CdSODE9. Investigating the sample CdSODEr1 we found both spherical shaped and needle-shaped nanocrystals. The average dimension evaluated from sampling 94 nanocrystals is (5.9 ± 1.2)nm. From the high resolution HRTEM image (inset Figure 3.7 left side) it is possible to distinguish the lattice fringes of the nanocrystals corresponding to a lattice distance of 0.31nm. These fringes may be assigned to the (002) lattice planes of the wurtzite phase of CdS. The sample CdSODE9 shows nanoparticles with size ranging from 6 to 12 nm. This result is in agreement with the absorption spectra (figure 3.6) which demonstrate that fixed the precursor concentration at 3mmol, the formation of larger nanocrystals is favored at higher annealing temperatures. Moreover the nanocrystals of sample CdSODE9 appear nearly polygonal rather than spherical. The same shape is observed for nanoparticles of sample CdSODEHe3. As shown by the bright field image in Figure 3.8 the synthesis at $10mmol$ and long annealing time produced large clusters. Their average size determined by statistical analysis on several low-magnification images is about $35.8 \pm 11.7nm$. This result is again in agreement with the UV-Vis absorption measurements which indicate a bulk behavior for this sample (Figure 3.5). The HRTEM image on the right side of Figure 3.8 shows some fringes, although the nanocrystals are very close each other and can be hardly seen at the magnification reported. The presence of fringes proves that the nanoclusters are crystalline but in some zones they are agglomerated rather then separated. Concerning the synthesis at the highest annealing temperature and rate (sample CdSODEHe6) the nanocrystals cannot be clearly identified by bright field TEM (Figure 3.9), this is possibly due to the extraction treatment used to separate them from octadecene. However by TEM at high resolution we were able to distinguish some nanoparticles . They appear spherical and crystalline with mean diameter of $3.6 \pm 0.9nm$. This result is in good agreement with the UV-Vis absorption measurements. The lattice fringes detected are spaced by $0.31nm$ indicating the same crystalline phase of the other samples investigated.

All the samples prepared were also studied by scanning TEM (STEM) analysis in dark field (HAADF). This analysis was performed with a wide angle detector getting images which show a contrast due to the atomic number and the local thickness. We measured the X-rays emitted by an energy dispersive spectrometer (EDS) with the electron beam focused on a single nanocrystal. The EDS spectrum exhibited the Cd K, Cd L, S K and O K edge peaks coming from the samples and also the C, Cu K and Cu L edge peaks which arise from the TEM grid (Figure 3.10).

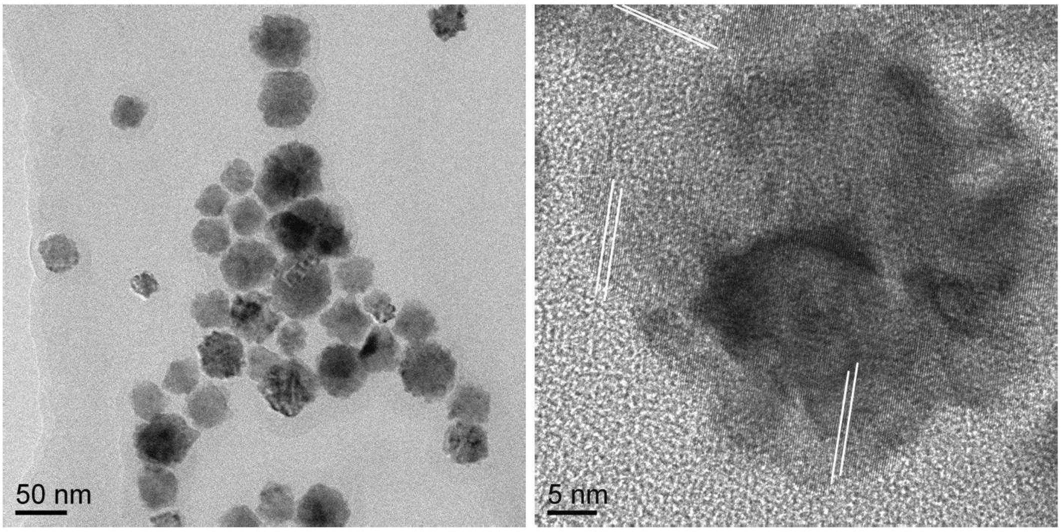

Figure 3.8: *Bright field TEM and HRTEM images of sample CdSODEHe5. The nanocrystals look aggregated and are characterized by a broad size distribution. Some lattice fringes (indicated by solid white lines) are visible but the crystalline phase is not well identified.*

To summarize, we assume that at 200^oC low precursor concentration leads to the nucleation of nanocrystals with wurtzite structure and needle shape. On the contrary higher temperatures promotes the Ostwald ripening process in which larger nanocrystals grow at the cost of the smaller one, resulting in larger size and polydispersity. In addition, the nanocrystals grow with faceted structures. This is a picture of the growth mechanisms in the case of sample CdSODEHe9. In the same manner at high precursor concentration the nanocrystals obey to the rule of the kinetically most favorable direction which is the one with the smallest activation barrier to growth process. Higher precursor concentration, corresponds to a higher value of precursor chemical potential which may be sufficient to induce nucleation on faces where nucleation generally does not occur at lower precursor concentration. These consideration may justify the formation of almost spherical-shaped nanocrystals.

The chemico-physical analysis performed by FTIR and NMR revealed an important property of the nanocrystals produced by thermolysis of $Cd(SR)_2$: the presence of organic chains coming from, thiols, that likely surround the nanocrystals and realize a sort of protective layer against chemical degradation. FTIR spectra of CdS nanoparticles at different precursor concentration and annealing process show a low peak around

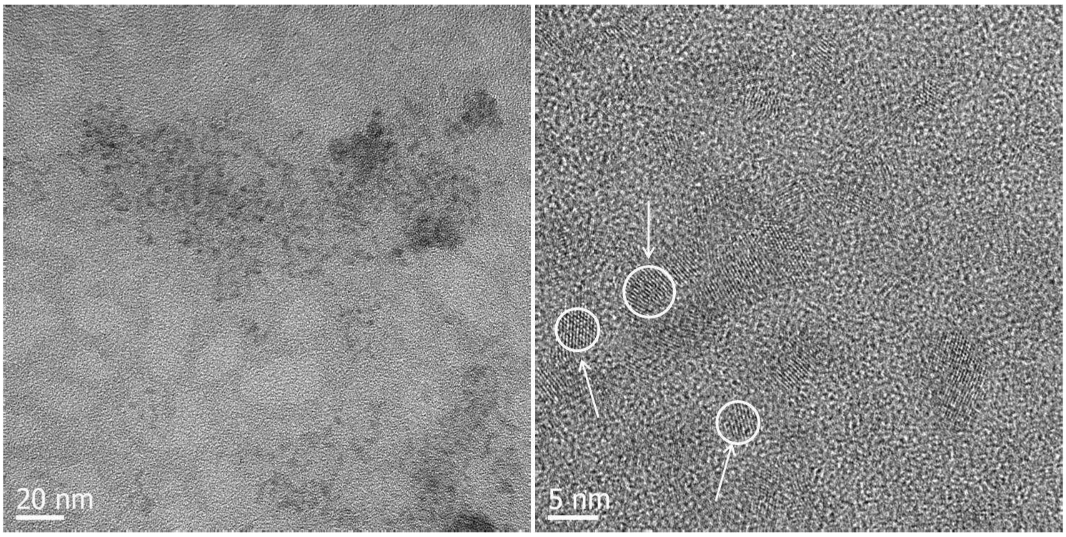

Figure 3.9: *Bright field and HRTEM images of sample prepared with 10mmol of Cd precursor and at the highest annealing temperature (240^oC). The annealing condition favored the formation of small and uniformly sized nanoparticles which also show regular lattice fringes spaced by* $0.31nm$.

$618cm^{-1}$ that indicates the presence of Cd-S bond [29], a signal at $2400cm^{-1}$ which is typical of the S-H groups of thiol molecules and signals at $3000-2800cm^{-1}$ (stretching region) and between 1500 and 600 cm^{-1} (bending region) that can be assigned to $-CH_2$ and $-CH_3$ of both the precursor and residual solvent. In addition the presence of water is also detected with two signals at $3600cm^{-1}$ and $3500cm^{-1}$ typically assigned to the O-H bond of water. On the other hand the ^1H-NMR spectra collected on samples CdSODEr1 and CdSODEHe5 show the typical signals of aliphatic protons of organic chains (at 1-2 ppm).

Both FTIR and NMR techniques confirm that the organic chains are still present after the thermolysis. In addition we verified experimentally that the nanocrystals can be completely and quickly dispersed in organic solvents after extraction treatment. Therefore the nanoparticles are embedded in an organic shell coming from the precursor molecules. This result was easily realized without introducing any more reagents in the reaction system.

Photoluminescence

The nanoparticels were also investigated from optical point of view in order to employ them for electro-optical applications. In particular we performed PL measurements

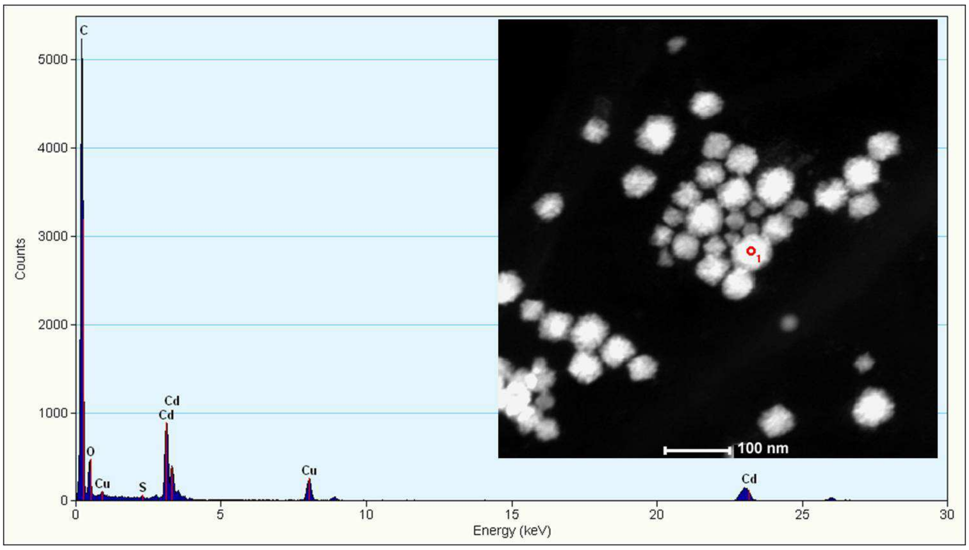

Figure 3.10: *EDS x-ray map recorded on nanocrystals (sample CdSODEHe5) indicated by a red dot in the image. It corroborates the presence of Cd and S in the nanocrystals.*

that provided information on different energy states available between valence and conduction bands responsible for radiative recombination. To perform such measurements we irradiated the nanocrystals in solution at a certain wavelength and collect the emission spectrum in the visible range. It is worth reminding that the absorption spectrum reveals the spectral range over which the sample absorbs, independently of the occurrence or not of radiative transitions. On the contrary the excitation spectrum corresponds to the specific region of the absorption spectrum that really contributes to the emission of light that can be observed. The maximum of excitation spectra appears in a spectral region overlapping the absorption and the photoluminescence curves. According to this rule and considering that the absorption of all the CdS nanocrystals occurs essentially in the UV to the blue spectral region, we got the emission spectra irradiating the samples at in the range 320 - 390 nm.

In Figure 3.11 we report the UV-Vis absorption and PL spectra of the samples CdSODEr1 and CdSODE9 excited at 375nm. It shows the evolution of photoemission of the growing nanocrystals with the temperature at concentration of 3mmol. The emission spectrum of CdSODEr1 exhibits two bands, a high energy band at 420 nm and a low energy band at 558 nm. The low energy peak is broad and stoke shifted, it can arise from deep trap emission. The high energy peak is a sharp peak (approximately

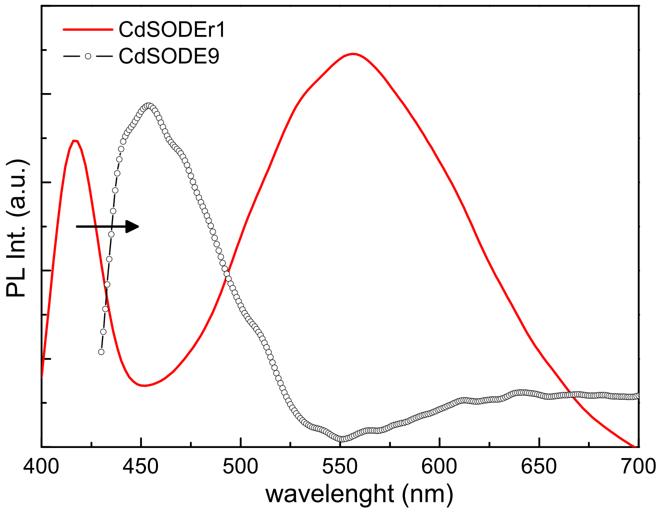

Figure 3.11: *PL spectra of the samples CdSODEr1 and CdSODE9 excited at 375nm. The emission spectrum of CdSODEr1 exhibits two bands, the first at 420 nm ascribed to luminescence by bound excitons and the second at 558 nm which can arise from deep trap emission. The sample annealed at higher temperature (CdSODE9) exhibits a broader and red-shifted (as indicated by the arrow) excitonic peak emission.*

20nm full-width half-maximum, FWHM) located near the absorption edge, it can be attributed to luminescence by bound excitons [30]. The stoke shift of the excitonic emission respect to the absorption peak is about 40meV. It is attributed to midgap states that probably come from surface defects. When the synthesis temperature was $240^o C$ (CdSODE9) the nanocrystals exhibited red-shift of excitonic peak from 420nm to 454nm and broader FWHM. The trap emission is greatly reduced, just a weak shoulder is present at about 504nm. This is probably due to a degree of trap emission suppression when the nanocrystals are larger or to a combination of exciton and trap emission. In Figure 3.12 we report the absorption and the PL curves (380nm excitation wavelength) of the sample at 10mmol (CdSODEHe6). The band gap emission in this case is peaked at about 425nm and is as broad as 50nm FWHM. No trap emission has been detected as in the case of sample CdSODE9.

The PL quantum Yield (QY) of the sample investigated was estimated according to the formula proposed by Demas [31], by comparing the integrated emission of a given nanocrystal sample in a diluite toluene solution ($10^{-6} M$) with that of florescein in

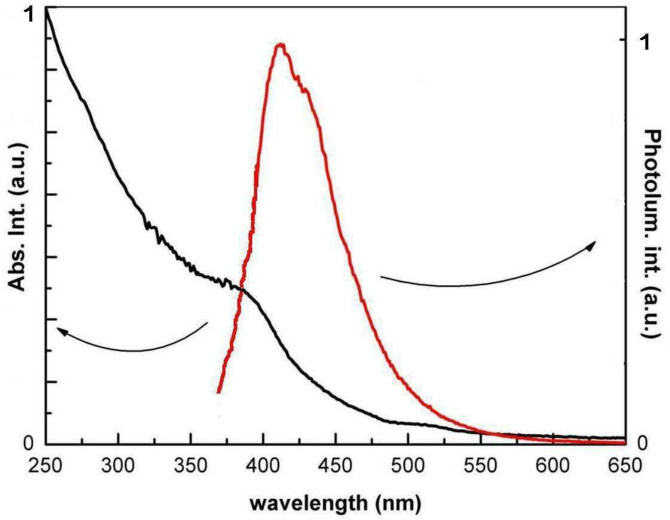

Figure 3.12: *Absorption and luminescence spectra of sample CdSODEHe6.*

0.1M NaOH solution. For CdSODEHe6 the QY is approximately 3.8%, for all the other samples it falls in the range 2-4%. This result is in agreement with the literature [32]

3.5.1 Wide Angle X-ray Scattering experiments

One aspect for working out a proper picture of the nanocrystals is the precise determination of their geometric parameters. Wide angle x-ray scattering (WAXS) is a technique that belongs to a family of non-destructive analytical methods, it is used to get information about the crystallographic structure, chemical composition, and physical properties of materials in solution, powders and thin films. In particular since it is based on elastic scattering of monochromatic X-rays, it can be used to study materials that do not have long range order. In particular synchrotron-based WAXS is particularly interesting to achieve higher quality of diffraction measurements with accurate background subtraction. Moreover the high brilliance of the synchrotron beam is usually needed to get good intensity and resolution that we are generally not achieved by in-house measurements due to the limited number of photons of common x-ray diffractometers and the poor scattering power of the samples. For these reasons we performed WAXS experiments at the ESRF synchrotron radiation facility in Grenoble (France) in order to evaluate the crystal structure (cubic or hexagonal) and estimate the dimension of the crystalline domains of the nanocrystals.

We measured the diffraction peaks of the samples and studied the influence the reaction annealing temperature and extraction treatment on the nanocrystals structure. The experiments were carried out at the beamline ID02. We put the samples in borosilicate glass capillaries (diameter = 2mm) to perform transmission diffraction measurements. The wavelength used was $\lambda = 0.918\AA$ corresponding to an incident energy of $12.46keV$. The distance between sample and detector was 0.118m. The investigation range is of the order of $1\AA$. The signal was revealed by a CCD camera in the range 2θ=$4^o - 35^o$. The WAXS q scale was calibrated using a Si standard and a powder sample of p-bromobenzoic acid. The empty-camera background was subtracted from WAXS pattern.

We performed both ex-situ and in-situ measurements. The ex-situ measurements were carried on the samples listed in Table 3.1. For each sample we compared the scattering pattern before and after the extraction procedure in order to get information about the crystal structure and the effect of the extraction process on the structure itself. The in-situ measurements were recorded starting from the solution of the precursor in ODE (precursor concentration 10mmol) and collecting data during the thermolysis. To heat the solution in the capillaries we used a Linkam heating stage. This measurement allowed to follow the evolution of the nanoparticles nucleation and growth in suspension.

For the analysis of WAXS pattern we assumed unstrained crystallites of pure materials with simple diffraction patterns instead of using methods with strain and finite crystal size or Fourier analysis [33][34]. As a consequence we approached the data analysis by the straightforward of peak-shape method which has the advantage that it does not assume any particular model for structural disorder or deformation. The principle of this method is that if crystallites are sufficiently small, the Bragg peaks in a diffraction pattern are broadened by an amount inversely proportional to the particle size. Measurement of the broadening thus gives a means of estimating the size through the well-known Debye Scherrer [35] formula given by

$$D = \frac{0.9\lambda}{\beta \cos\theta} \tag{3.10}$$

where D is the apparent particle size, β is the FWHM of the X-ray diffraction line in radians, λ is the wavelength used, and θ is half the scattering angle. The constant 0.9 in Eq.3.10 depends slightly on the symmetry of the crystal [36][37]. Concerning the ex-situ measurements, we report the results for two samples, CdSODEHe1 and CdSODEHe3, before and after extraction treatment (Figure 3.13 3.14). The crystalline CdS nanoparticle growth is hardly detectable for the sample CdSODEHe1, in which we distinguish three weak peaks in the diffraction curve. The peaks at q = $26.5nm^{-1}$ and $37.2nm^{-1}$ may be assigned to the reflections (102) and (201) of the hexagonal phase of CdS while the peak at $23nm^{-1}$ doesn't belong to CdS and could be due to impure crystalline phases. The sample CdSODEHe3 shows more intense diffraction peaks in the same position of sample CdSODEHe1 stressing the fact that the nanocrystals population and their size increased with annealing time as we expected. It is interesting

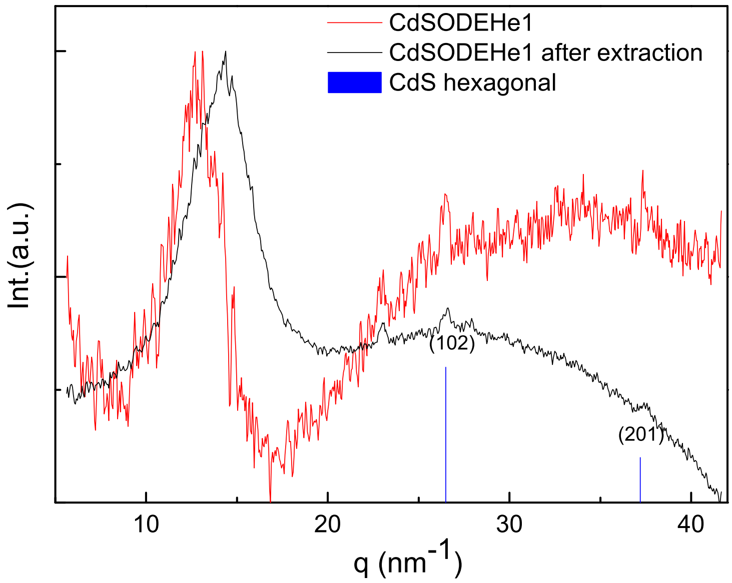

Figure 3.13: *Synchrotron wide angle scattering curves of sample annealed at* 200^oC *for 1min. The scattering spectra before and after the extraction process are compared. The peaks at* $q = 26.5nm^{-1}$ *and* $37.2nm^{-1}$ *may be assigned to the reflections (102) and (201) of the hexagonal phase of CdS while the peak at* $23nm^{-1}$ *doesn't belong to CdS and could be due to impure crystalline phases. The peak at low q is ascribed to the glass capillaries used during the experiments.*

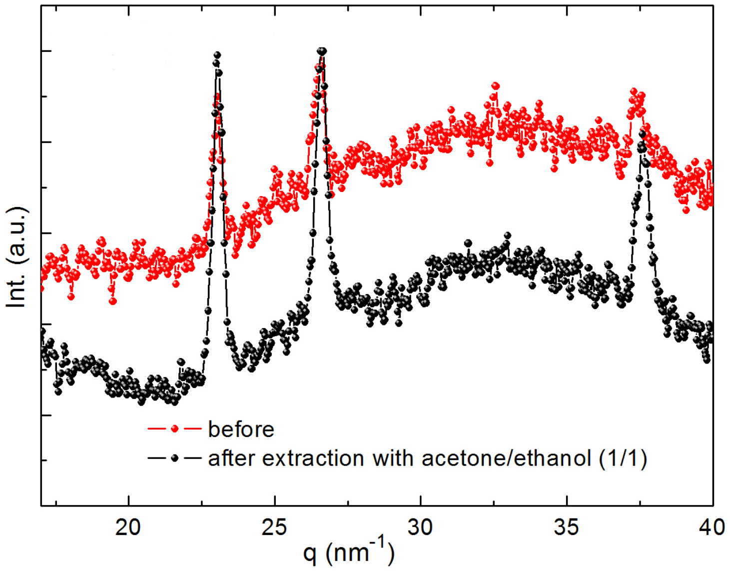

Figure 3.14: *Synchrotron wide angle scattering curves of sample CdSODEHe3 before and after extraction process. The sample shows more intense diffraction peaks in the same position of sample CdSODEHe1 stressing the fact that the nanocrystal population and their size increase with annealing time.*

to observe that for all samples the signal/noise ratio of the peaks improves for the extracted solutions pointing out that the extraction process helps in eliminating organic residuals.

In the case of in-situ experiments we prepared a solution of Cd precursor in octadecene with concentration of 10mmol . Such solution was put in a capillary and heated up to 240^oC at 10$^oC/min$. Then it was kept at the final temperature for 30 min in order to follow the growth of nanocrystals and confirm the results given by the corresponding ex situ samples, CdSODEHe5 and CdSODEHe6. Another experiment was performed up to 300^oC at 10$^oC/min$ in order to get information about the nanocrystals structural evolution through all the decomposition process of the precursor which ends at about 300^oC. WAXS patterns were acquired from the beginning of the annealing process. Therefore, time t=0 s corresponds to the time at which the sample was at room temperature. During the experiments we recorded 1 frame every 30s.

Figure3.15 shows the results of the in-situ measurements at fixed temperature of 240^oC

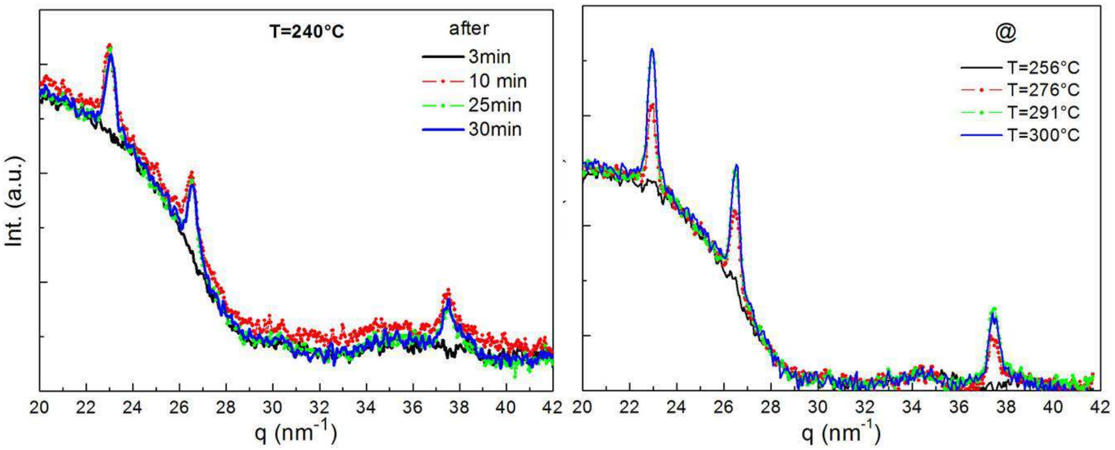

Figure 3.15: *In-situ WAXS measurements during the synthesis of CdS nanocrystals starting from* $Cd(SC_{12}H_{25})_2$ *dispersed in ODE at 10mmol. Scans recorded from room temperature to* 300^oC *(right side) and to* 240^oC *(left side) extending the annealing process up to 30min.*

and different annealing times (on the left) and as function of temperature up to 300^oC (on the right). No diffraction peak was visible up to 240^oC but keeping that annealing condition for 10min was sufficient to allow the formation of nanocrystals. Longer annealing time didn't modify either the crystal structure or the nanocrystal size. This result suggests that the imposed annealing conditions favor the competitive growth of crystallites. Compared to ex situ results the crystal structure is the same but the peaks are less intense. The experiment performed at 300^oC as final temperature, didn't give any evidence of nanocrystal formation increasing the temperature up to 240^oC. Some peaks corresponding to the crystalline phase of CdS, appeared at 250^oC. Therefore it the temperature steadily grows, the nucleation and the normal growth stages occur at temperature higher than 250^oC instead of 240^oC as observed in the previous experiment.

The in situ experiments demonstrated that the increase of temperature promotes a rapid Ostwald ripening process in which larger nanocrystals grow because the crystalline peaks are more intense with narrower FWHM. The measured mean diameter of nanocrystals was 8.9 nm at 240^oC and 9.9nm at 300^oC. Moreover, we found that the diffraction peaks are less intense than in the ex-situ case. This could be due to a lower nanoparticles number as consequence of: a) the in situ process could have taken place in a slightly different conditions of temperature and annealing rate than the ex situ one since the heater and the set-up used were different, b) the in situ reaction took place in a capillary with a very small volume, while the ex situ one was conducted in a reaction flask and the solution was continuously stirred to guarantee a homogeneous heating.

3.5.2 Atomic Force Microscopy analysis

In many technological applications the nanoparticles need to be placed on solid substrates covering uniformly the surface as a monolayer or multilayer. Uniform distribution of nanoparticles on a surface is also important to study the properties of single nanostructures through scanning probe microscopy technoques. In the latter case the nanoparticles need to be placed on solid substrates, spaced farther apart than the spatial resolution of the probing method because of the limited image acquisition rates of such techniques. However, uniform deposition distribution is still a difficult task. It usually cannot be achieved by simply drying a colloid drop on a substrate. Surface asperities and solute particles pin down the contact line, creating a radial outward flow when the solvent evaporates. The laminar flow drags solute particles outward and forms a ringlike deposit (coffee ring effect). When the solvent layer becomes thinner than the particles, capillary forces pull the deposited particles into a close-packed arrangement.[38][39]. Methods such as self-assembly and spin coating [40][41] have been developed and are widely used to overcome these phenomena. A new route to deposit colloidal particles was proposed by Lee et al.[42]. It consists on the deposition of boiling drops on hot substrate to avoid laminar flow and aggregation process of the nanoparticles. We tested the feasibility of this so called "boil deposition" method by dropping few μL of nanoparticles in solution on two different substrates, a silicon wafer and mica. The nanoparticles of sample CdSODE1 and CdSODEHe6, after the extraction procedure, were diluted in ethanol, a solvent characterized by low boiling point. The substrate was heated up on a hot plate, then we placed few drops of the colloid on the substrate and left the solvent to evaporate. We also tested the so called indirect boiling method by dropping the colloidal solution on an hot steel plate adjacent to the substrate, in this case the deposition would have achieved through microdrops ejected from the main boiling drop.

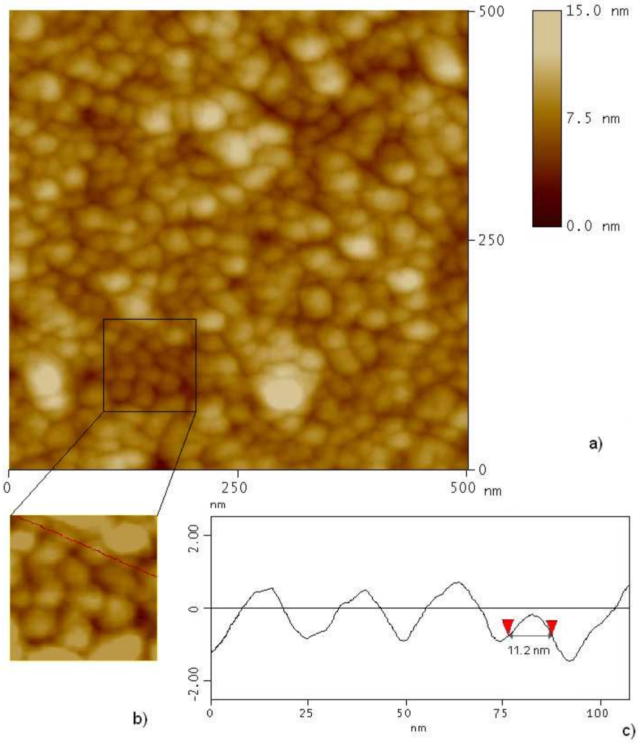

Figure 3.16: *a) Tapping mode AFM image of CdS nanoparticles of sample CdSODEr1; b) blow up image (scan size 100nm 100nm, height scale 5 nm) and c) section analysis taken along the straight line.*

Upon several attempts we found out that the optimum condition was the direct deposition on substrate heated at $150^{o}C$. In particular cleaved mica substrate was preferred because it offers an extremely flat surface and allows the acquisition of reliable scanning images. We also learned that the microdrops must wet the surface. If a substrate is too hot, the microdrops slid off without wetting (Leidenfrost effec) and dispersed deposition does not occur. However, at sufficiently high temperatures, a microdrop seems to dewet smoothly the surface probably because of heating-related contact-line perturbations that prevent self-pinning of nanoparticles on the surface.

We monitored the effectiveness of this method through AFM analysis. The scanning probe analysis provided also information about the shape and the size of the nanoparticles. Those results have been compared with those obtained by different techniques such as TEM and optical spectroscopy.

The AFM image in Figure3.16 shows the topography and section analysis taken along the straight line of sample CdSODEr1. They were recorded in tapping mode and indicate circular shape structures covering uniformly the investigated area (scan size 500nm x 500nm). The mean surface roughness was $1.6nm$. The average dimension determined by statistical analysis ranges between 10-16nm nm in lateral size with a standard deviation $\sigma = 1.5nm$ indicating that the nanoparticles are almost uniformly synthesized and distributed on the MICA surface. However the nanoparticles dimension is overestimated with respect to the diameter values calculated from the absorption spectrum and TEM. In fact it is not easy to obtain a reliable estimation of nanoparticles size because of both the slightly layered nature of the sample and the tip-curvature radius of about 8nm [43]. We applied the method to different colloids with little or no change in the morphological details.

3.6 Conclusions

We have shown that it is possible to prepare CdS nanocrystals adopting a simply synthetic route on the way to green chemical synthesis, the thermolysis of a single Cd precursor in octadecene. The thermolysis proceeds with the melting of the thiolate precursor (in the range 110-130^oC) and its transformation into the relative metal sulfide nanoparticles at higher temperature (above 190^oC). Small nanoparticles with a good degree of crystallinity were prepared by studying the nanocrystals growth at different annealing conditions. On the basis of the results of HRTEM, EDS and WAXS we assume that the CdS nanocrystal phase has not yet clearly determined. Along with the diffraction peaks ascribed to the hexagonal phase also Cd in a crystalline phase and non stoichiometric phase, Cd_xS_y, might be considered. We found that the CdS nanocrytals size prepared by thermolysis of cadmium thiolate precursor in ODE mainly depends upon a combination of the temperature, speed and duration of the annealing procedure and also on the precursor concentration. The use of both relatively high precursor concentration (10mmol) and low annealing rate favor the growth of bigger nanocrystals that shows up as a darker solution with a broad size distribution. Whereas less concentrated solution as well as high annealing rate favor the formation of CdS nanocrystals with narrow size distribution and good optical properties even at temperature as low as 200^oC. In particular, we noticed that the precursor concentration maybe more than the reaction temperature and time played a critical role in the growth of nanocrystals with uniform size in the confinement regime. The synthesis method here reported is a one pot process leading to nanocrystals with a surface passivated by the thiol chains coming from the precursor without the use of additional passivating agents. This synthetic route of nanocrystals has several advantages. The first and most important aspect is that the synthesis involves a single source precursor. Consequently, there is no preparation complication due to multicomponents mixing, moreover no toxic reagents and solvents are used. In addition, it is a low cost and environmental-friendly method. The mentioned properties lead to the consideration that the thermolytic synthesis is a very promising technique which can be extended to other semiconductor compound and provide an extensive nanoparticle production.

Bibliography

[1] S. V. Gaponenko, *Optical Properties Of Semiconductor Nanocrystals*, Cambridge University Press (1998).

[2] S.Tiwari, Cryst. Res. technol. 41, 1, 78 (2006).

[3] L.A. Patil, P.A. Wani, D.P. Amalnerkar, Materials Chemistry and Physics, 61,3, 260 (1999).

[4] K.Murakoshi, H. Hosokawa,M. Saitoh, Journal of the Chemical Society, Faraday Transactions, 94, 4, 579 (1998).

[5] S. Ninomiya, S. Adachi, J.Appl.Phys. 78, 1183 (1995).

[6] A. Zunger, A.J. Freeman, Phys.Rev. B 17, 4850 (1978).

[7]) A.N. Goldstein, O. Park, *Handbook of nanophase materials*, Michigan, USA.

[8] A. Zunger, A.J. Freeman, Phys.Rev. B, 17, 4850 (1978).

[9] R.Rossetti, R. Hull, J.M. Gibson, L.E. Brus, J.Chem. Phys., 82, 1, (1985).

[10] A.P. Alivisatos, A.L. Harris, N. Levinos, M. Steirgerwald, L. Brus, J.Phys. Chem. 89, 4001 (1988).

[11] D.V. Talapin, A.L. Rogach, A. Kornowsky, M. Haase, H. Weller, Nano Lett. 1 (4) (2001).

[12] C.B. Murray, D.J. Norris, J. Am. Chem. Soc. 115 (19), 8706 (1993).

[13] W.W. Yu, X.G. Peng, Angewandte Chemie-International Edition, 41(13), 2368 (2002).

[14] J. Ouyang, J.Kuijper, S. Brot, D. Kingston, X. Wu, D. M. Leek, M. Z. Hu, J. A. Ripmeester, K. Yu, J. Phys. Chem. C, 113, 7579 (2009).

[15] J.O. Winter, N. Gomez, S. Gatzert, C.E. Schmidt, B.A. Korgel, Colloids Surf. A, 254, 147 (2004).

[16] Y.Wang, N. Herron, Chem. Phys. Lett., 200,1 (1992).

[17] A.R. Rao, V. Dutta, Phys. Status Solidi A, 201, R72 (2004).

[18] Z.Li, J. Zhang, J.Du, T.Mu, Z.Liu, J.Che, B.Han, J. Appl. Polym. Science, 94, 1634 (2004).

[19] J.H. Warner, A.A.R. Watt, R.D. Tilley, Nanotechnology 16, 2381 (2005).

[20] A.B.R. Mayer, Mater. Sci. Eng. C, 6, 155 (1998).

[21] V. Rotello, *Nanoparticles: Building Blocks for Nanotechnology* (Nanostructure Science and Technology) Springer-Verlag, Berlin, (2003).

[22] F. Antolini, M. Pentimalli, T. Di Luccio, R. Terzi, M. Schioppa, M. Re, L. Mirenghi, L. Tapfer, Mater. Lett. 59, 3181 (2005)

[23] T. Di Luccio, A.M. Laera, L. Tapfer, S. Kempter, R. Kraus, B. Nickel J.Phys. Chem. B 110, 12603 (2006).

[24] G. Mie, Ann. Phys., 25, 377 (1908).

[25] R.L. Wells, C.G. Pitt, A.T. McPhail, A.P. Purdy, S. Shafieezand, R.B. Hallock, Chem. Mater. 1, 4 (1989).

[26] L.E. Brus, J. Chem. Phys. 79, 5566 (1983).

[27] J. Tauc, *Amorphous and liquid semiconductor*, Plenum Press, New York, 159 (1974).

[28] S. M. Sze, *Physics of Semiconductor Devices*, John Wiley and Sons Inc., New York (1969).

[29] P. Thangadurai, S. Balaji, P.T. Manoharan, Nanotechnology 19, 435708 (2008).

[30] Y. Wang, G. Meng, L. Zhang, C. Liang, J. Zhang, Chem. Mater. 14, 1773 (2002).

[31] J.N. Demas, G.A. Crosby, J. Phys. Chem. 75, 8 (1971).

[32] B.A. Harruff, C.E. Bunker, Langmuir 19, 893 (2003).

[33] B.E. Warren, B.L. Averbach, J. Appl. Phys. 21, 595 (1950).

[34] P.W. Stephens, J.Appl. Cryst. 32, 281 (1999).

[35] P. Scherrer, Nachr. Ges. Wiss. Gttingen, Math.-Phys. Klasse 26 98 (1918).

[36] F.W. Jones, J. Sci. Instrum. 18, 157 (1941).

[37] K.H. Riewe, Z. Kristallogr. 96, 85 (1937).

[38] R.D. Deegan, O. Bakajin, T.F. Dupont, G. Huber, S.R. Nagel, T.A. Witten, Nature London 389, 827 (1997).

[39] N.D. Denkov, O.D. Velev, P.A. Kralchevsky, I.B. Ivanov, H. Yoshimura, K. Nagayama, Langmuir 8, 3183 (1992).

[40] A.N. Shipway, E. Katz, I. Willner, Phys. Chem. Phys. Chem. 1, 18 (2000).

[41] Y.K. Hong, H. Kim, G. Lee, W. Kim, J.I. Park, J. Cheon, J.Y. Koo, Appl. Phys. Lett. 80, 844 (2002).

[42] K. Lee, M. Duchamp, G. Kulik, A. Magrez, Jin Won Seo, S. Jeney, A.J. Kulik, L. Forr, R.S. Sundaram, J. Brugger, Appl. Phys. Lett. 91, 1731 (2007).

[43] *Scanning Probe Microscopy Training Notebook*, Version 3, Digital Instruments/Veeco Metrology Group Inc., 2000.

Chapter 4

Synthesis of CdS nanoparticles in an inert polymer matrix

4.1 Introduction

Hybrid organic and inorganic materials with an organic matrix filled with inorganic species of the size usually 1-100 nm have emerged as an advanced class of electronic, optoelectronic and sensor media for several technological applications. The basic idea behind the development of hybrid materials is the combination of organic and inorganic components at the molecular scale in order to achieve a synergy of the most important properties of the components. Organic materials such as the polymers offer some advantages that have attracted so much interest from the electronic manufacturers. The following lists some of them:

- Easy processing;
- Low cost of production, usually by chemical synthesis rather than microelectronic based clean technologies;
- Low cost of the materials for the devices fabrication;
- Non expensive manufacture of large area devices such as LEDs or photovoltaic cells;
- Availability of totally new materials morphologies and devices geometries;
- Opportunity to make devices based on totally new principles;

- Possibility to realize nanometric devices components especially using self assembly-based techniques;
- Enormous possibilities to vary the composition and hence properties of the materials.

On the other hand inorganic materials, such as nanoparticles, offer tunable properties achieved by controlling their composition, size and interface with the matrix, fluorescence efficiency and great stability that can be further improved by modifying the nanoparticles surface Mixture of polymers and inorganic nanoparticles (nanocomposite) produces hybrid materials with tuneable attributes offering modulated properties. They have been designed in the last two decades opening up exciting directions in the material science and related technologies with significant implications in the nanotechnological processing, which facilitate integration, miniaturization and multifunctionalization of devices [1] [2].

The structure, the degree of order and the main characteristics of nanocomposites depend not only on the chemical features of the organic and inorganic components, but also on the interaction that is established between them. Therefore the design of hybrid nanocomposites is primary dictated by the nature the extent and accessibility of inner interfaces [3]. With regard to the nature of interaction between organic and inorganic components two categories of materials can be distinguished. Class I includes hybrids in witch both components interact in a weak manner (Van der Waals contacts, $\pi - \pi$ interacion and hydrogen bonding) and Class II in which the organic and inorganic part are linked through strong chemical bond (covalent, ion-covalent bonds). The chemical route employed determines dramatically the tailoring of the hybrid networks [4].

Concerning the synthesis techniques of nanocomposites we first distinguish between the top-down or the bottom-up procedures. In the top-down approach, the large micron sized particles are disintegrated to form nanostructures, this technique is typical of the nanocomposites prepared from layered silicates-clays. In the bottom-up approach the nanosctructures grow within the polymer matrix from a molecular level. Two main techniques belonging to the bottom-up approach have been developed:

- classical self assembly strategies involving the presence of organic templates that act as structure-directing agents
- self directed assembly strategies that is self organization of precursor molecules. This strategy yields complex hierarchical architectures with intricate structures and several stages of organization.

A key problem of polymer-nanoparticles nanocomposites is the achievement of a fine dispersion of the nanoparticles in a polymer matrix. The very high surface energy of nanoparticles and interparticle distances result in strong particle-particle interactions, and in a tendency to the formation of aggregates and agglomerates. This effects could deteriorate the material properties. In this framework, the success of nanotechnology is related to the capability to organize uniformly the nanoparticles within the polymer matrix. The bottom up technique which consists of *in-situ* generated nanostructures, is generally acknowledged as an useful synthesis technique to get uniformly nanoparticles distribution because the initially reacting species are dispersed in the polymer matrix.

This part of PhD work is devoted to the preparation of polymer-nanoparticle nanocomposites by bottom up technique, in other words by inducing the growth of CdS nanoparticles within an a polymer matrix. We started studying the synthesis in an amorphous and inert polymer which doesn't interfere with the structural and optical properties of CdS in nanocomposite. Our work was devoted to the study of the structural and optical properties of CdS in the nanocomposites by grazing incidence x-ray diffraction (GID), UV-Vis absorption and luminescence spectroscopy.

The activity about the realization of hybrid nanocomposites proceeded further by synthesis of CdS nanoparticles in a conducting polymers (COPs) as described in the following chapters.

4.1.1 Grazing Incident Diffraction: generalities

Grazing-incidence x-ray diffraction (GID) is a scattering technique in which the geometry of the Bragg condition is combined with the conditions for x-ray total external reflection from sample surfaces. This provides superior characteristics of GID as compared to the other diffraction schemes in the studies of thin surface layers, since the penetration depth of x-rays inside the slab is reduced 1-10nm. As a consequence, in GID experiments, the incident beam, k_i is kept below a critical angle in order to enhance the signals from the surface and determine the two dimensional Bragg reflections of crystalline structures on the top layer of the sample [?]. For instance, an ordered 2D system gives rise to rod like Bragg reflections that contain information on the electron density along the z-axis of the ordered objects. However, since the total cross section for scattering from a 2D system is in general very small X-ray flux from synchrotron sources is generally required.

4.2 Synthesis of Topas-CdS nanocomposites

A simple method to realize CdS polymer-nanoparticle nanocomposites by bottom-up approach is the thermolysis of Cd and S precursor in the polymeric matrix. The thermal treatment of bulk precursor/polymer system causes the decomposition of the precursor and the aggregation of the Cd and S atoms into CdS nanoparticles within the polymer. The nanoparticle size and aggregation in bulk nanocomposites are mainly determined by the annealing conditions, namely temperature and duration of the treatment [5].

In addition to bulk nanocomposites the thin film technologies are also being developed as a means of reducing the cost of optoelectronic manufactures and allowing the fabrication of devices on flexible substrates. In this framework our attention was focused on realizing nanocomposite in a inert matrix both as bulk and as thin film. In particular we realized CdS based nanocomposites by thermolysis of Cd precursor, $Cd(SC_{12}H_{25})_2$, in Topas.

Topas (TP) is the brand name of the cyclic olefin copolymer (Topas COC) manufactured by Ticona. It is an amorphous transparent copolymer characterized by highly transparency (light trasmittivity=91%) and stable optical properties. It is an excellent dielectric and shows high heat resistance (glass transition temperature equal to about 50^oC). Concerning the Cd precursor, we report about its chemico-physical properties in the Chapter 3.

The performances of hybrid nanocomposite based device can be greatly improved if the formation of nanoparticles occurs at relatively low temperature and their growth within the polymer matrix is carefully controlled since the very first stages of formation. Given these assumptions we are interested in discovering the annealing condition that allows the CdS nucleation in the polymeric matrix. To this purpose the samples as thin film were characterized by grazing incidence diffraction (GID) during the annealing process. Besides important indications on the nanoparticle formation were given by optical measurements. Absorption and photoluminescence (PL) spectroscopy measurements allowed to determine the band gap and the size of the nanoparticles at different synthesis conditions.

4.3 Experimental

The samples were prepared adopting the following procedure. We dissolved TP in toluene (TP concentration $5mg/mL$) at 80^oC under magnetic stirring up to its complete solubilization. Then we added a stoichiometric amount of Cd thiolate precursor (20% by weight of Cd precursor in TP corresponding to CdS mass fraction of $\sim$ 4%) to the polymer solution under magnetic stirring. The solution was dried under vacuum and the obtained bulk foil was annealed in the range 200^oC-300^oC for 20min. Each annealed sample was then dissolved in toluene to make optical measurements in quartz cuvettes. A different set of samples were prepared by spin coating the precursor/polymer dispersion (at 3000rpm) onto Si/SiO_2 substrates in order to get films 30nm thick. Such samples were used to make GID analysis. The experiments were carried out at ESRF synchrotron radiation facility in Grenoble (beamline ID01). Figure 4.1 shows the GID geometry used for the experiments. The measurements were performed during the thermolytic process. The incident beam energy was 12 KeV. During the measurements the sample was kept under primary vacuum ($\sim 10^{-1}$ mbar) and was heated by using a small furnace with beryllium dome mounted on the diffractometer.

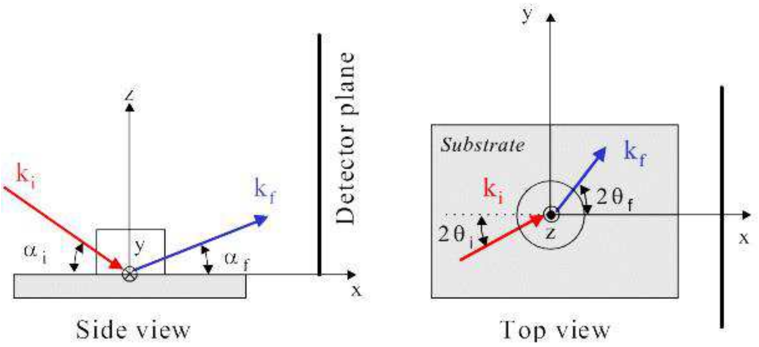

Figure 4.1: *Grazing-Incidence Diffraction geometry used during the experiments with the synchrotron radiation to determine the crystalline structure of CdS nanoparticles embedded in Topas thin films.*

sample	T(^oC)	Eg (eV)	d(nm)	PL peak (nm)	PL FWHM (nm)
$TPCdS-A$	240	3.58	2.48	614	126
$TPCdS-B$	250	3.17	3.08	530	104
$TPCdS-C$	276	2.80	4.33	479	117

Table 4.1: *Annealing temperatures of TP/CdS samples; calculated optical parameters, band gap (Eg) and diameter (d), relative to CdS nanoparticles embedded in Topas matrix; spectral position of the PL peak emission and full-width-at-half-maximum FWHM.*

4.4 Results and discussion

GID measurements were performed in the annealing temperature range $170-250^oC$. We used an incident angle of 0.08^oC, well below the critical angle ($\alpha_c = 0.15^oC$) to enhance the scattering signal from the nanoparticles. At 170^oC we already observed very pronounced crystalline peaks from cubic CdS corresponding to 2 nm size crystals, as shown in Figure 4.2. With increasing temperature, the CdS Bragg peaks become more intense and sharper, while the TP amorphous peak intensity (at $2\theta = 10.7^oC$) decreases. This indicates that the polymer deteriorates at high temperatures, as shown in the curve at 250^oC where the peak due to the SiO_2 layer becomes more evident. Taking advantage of the optical properties of Topas which is inert in the visible spectral region, we performed UV-Vis absorption and PL analysis in order to determine the band gap, the size and the emission wavelength of CdS nanoparticles embedded in the matrix. The measurements were performed on bulk samples in order to maximize the signal coming from the nanoparticles.

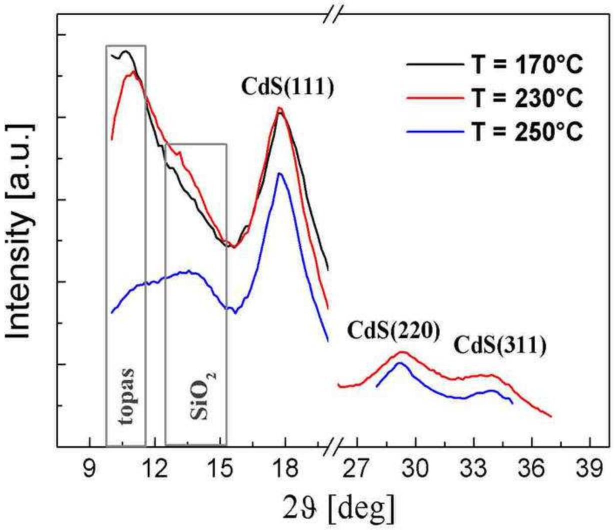

Figure 4.2: *In-situ GID curves measured on a TP/*$Cd(SC_{12}H_{25})_2$ *film* 170^oC, 230^oC *and* 300^oC. *Crystalline peaks of the cubic phase of CdS are already detectable at* 170^oC *and become sharper with the annealing temperature.*

The UV-Vis absorption and PL measurements were performed in solution. Figure 4.3 shows the UV-Vis absorption spectra of Cd precursor in toluene, TP dissolved in the same solvent and samples annealed at 240^oC, 250^oC and 276^oC respectively. The Cd precursor and the polymer curves don't show any structure in the UV-Vis range. Whereas the TP-CdS nanocomposites show a peak which is ascribed to the excitonic absorption E_0 of CdS (see Chapter 1 and Chapter 3 for theoretical details). Its position is clearly blue-shifted respect to the bulk CdS ($2.42eV$ for the CdS hexagonal phase) as we can see from comparison with the dielectric constant spectrum shown in Figure 4.3. This result points out the quantum confinement effect thus the formation of CdS at dimensions below the Bohr radius [6]. The absorption peak moves towards lower energy values with increasing annealing temperature indicating that the nanoparticle size increases. The nanoparticle mean diameter calculated from Brus equation [6] increases from 2.4nm to about 4.3nm as reported in Table 4.1 along with the corresponding band gap values. The PL spectra of nanocomposites excited at the wavelength were the absorption reaches the maximum, are shown in Figure4.4. The curves have been normalized to take into account different exposure times and different detector amplifications. The measurements show a broad features which red-shifts with increasing the annealing temperature. It corresponds to a gradual change from

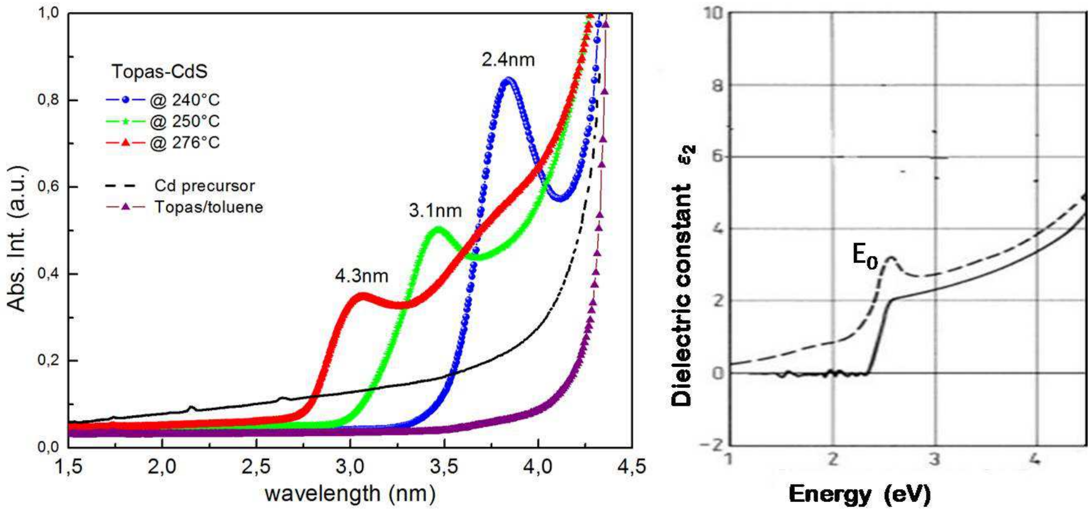

Figure 4.3: *Absorption spectra of Topas/Cd precursor samples at different annealing temperatures, 240, 250 and 275C. The pronounced feature in each spectrum is related to the E0 energy transition of CdS. The dielectric complex coefficient plot with indication of the energy position of E0 for bulk CdS is shown on the right [7]. The red shift of the absorption threshold has been observed with increasing the annealing temperature.*

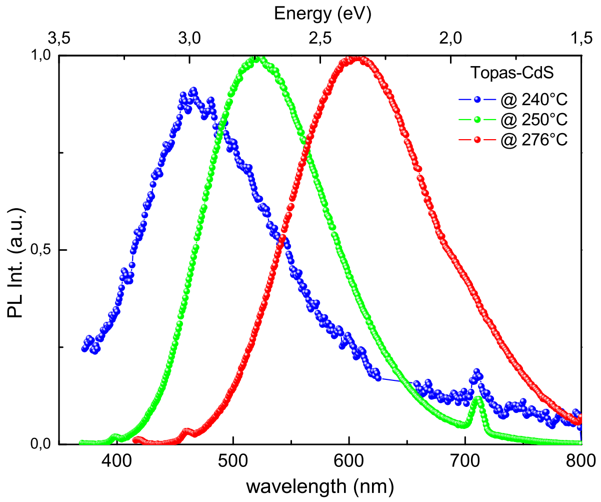

Figure 4.4: *Photoluminescence (PL) emission of Topas/Cd precursor samples annealed at temperatures T=240, 250 and 275C exciting at the wavelength were the absorption reaches the maximum. The emission is red shifted with increasing the annealing temperature.*

blue to orange emission. If the annealing temperature is increased above 280^0C the PL signal becomes very weak and reduces to background. The Cd precursor and the polymer are characterized by zero emission in the range investigated, consequently the PL signal is ascribed to CdS charge recombination. The broad emission (FWHM values are reported in Table 4.1) in such a wavelength range may be ascribed to both the charge carrier recombination in trap states [8]. and the band-edge emissions [9] At 276^oC a distinct shoulder at about 750nm in the emission curve is detected. It comes from the defect states probably due to sulfur vacancies [10] The blue shift of the PL peak in the direction of smaller nanoparticle size is also supported by similar experiments in literature [5][11].

4.5 Conclusions

We synthesized CdS nanoparticles in TP matrix by in-situ thermolysis of the Cd thiolate precursor. The crystalline structure of CdS nanoparticles and their spatial distribution in TP films were investigated by the GID techniques. One of the main result of the experiments is that a temperature of 170^oC is sufficient for the CdS nanoparticles to form in thin films, while in the bulk system a temperature of 200^oC is needed [5]. It has been also proved that the nanoparticles grow with temperature.

The optical properties of nanocrystals were determined by UV-Vis absorption and PL spectroscopy after annealing of solid TP/Cd precursor samples. Significative results have been obtained in the range $240 - 280^oC$. Quantum confinement effect as been proved by UV-Vis absorption measurements which also show that nanoparticles of $2.4nm$ in diameter become bigger with increasing temperature. The color emission goes from blue to orange annealing at 240^oC and 276^oC respectively.

The presented results are an important and very promising step in taking control of the production of CdS nanoparticles in polymer matrix with specifically optical properties. They have been fundamental for the comprehension of the subsequent experiments concerning the synthesis of CdS in a conductive matrix.

Bibliography

[1] C. Sanchez, B. Julian, P. Belleville, M. Opall, J.Mater.Chem 15, 3559 (2005).

[2] L.D. Carlos, R.A. S Ferreira, V. de Zea Bermudez Wiley, weinheim, pp353-380 (2007).

[3] C. Sanchez, G.J. Soler-Illia, F. Ribot, T. Lalot C.R. Mayer, V. Cabuil Chem.Mater. 13, 3061 (2001).

[4] C. Sanchez, B. Julin, P. Belleville, M. Popall, J. Mater. Chem. 15, 3559 (2005).

[5] T. Di Luccio, A.M. Laera, L. Tapfer, S. Kempter, R. Kraus, B. Nickel, J. Phys. Chem. B 110, 12603 (2006).

[6] L. E. Brus, J. Chem. Phys. 79, 5566 (1983).

[7] S. Ninomiya, S. Adachi, J.Appl.Phys. 78, 1183 (1995).

[8] L. Spanhel, M. Haase, H. Weller, A. Henglein, J. Am. Chem. Soc. 109, 5649 (1987).

[9] J.W.M. Chon, M. Gu, C. Bullen, P. Mulvaney, Appl. Phys. Lett. 84, 4472 (2004).

[10] Hooi Ling Lee , Issam Ahmed Mohammed , Mohammed Belmahi , Mohamed Badreddine Assouar , Herv Rinnert Marc Alnot, Materials , 3, 2069 (2010).

[11] S.F. Wuister, A.J. Meijerink, Lumin. 105, 35 (2003).

Chapter 5

Poly(N-vinylcarbazole) - CdS nanocomposites

5.1 Introduction

This chapter deals with the developments of hybrid nanocomposite materials based on COPs with special emphasis on their impact on energy related devices such as OLED and solar cells.

The prominence of conducting organic polymers (COPs) in the last two decades has been related to two crucial historical events: first, the discovery of their electrical conductivity in 1977 by Shirakawa et al. [1] and later finding of their electroluminescence in 1990 [2]. Their conductivity and functionality can be controlled by means of two characteristic mechanisms: redox doping and acid-base doping. A careful choice of the latter has a direct influence on the final properties and, obviously on their final applications like conductive plastics, catalysts, membranes, batteries, sensors, etc. On the other hand in their undoped form COPs behave as intrinsic semiconductors and their properties can be modulated by the modification of the backbone or by substitution of the polymer chain. This versatility has placed COPs in the center of a constantly growing research area and has made them key players in many different applications like the plastic electronic industry, as polymer lasers, OLEDs, photovoltaic cells, field effect transistors, etc [3]

As a part of photovoltaic device, COPs present some drawbacks. Devices based on single layer COPs are able to produce good voltage values with poor photogenerated current. The main reason for this is the short exciton diffusion length and the relative low conductivity of COPs. An interesting class of photoactive material can be generated combining two properties, carrier generation efficiency and transport mobility. A typical approach is the incorporation of nanoparticles in a carrier transporting polymer. The blending of both materials into one phase-segregated mixture is a good option for shortening the travel distance for excitons, enhancing the efficiency of the composite and extending its sensitivity range (this topic will be examined in the next chapter).

Concerning other applications like organic LEDs, we have to consider that typical photoluminescent polymers are almost transparent in the visible spectral region and their emission occurs in the UV-blue region. Incorporating inorganic nanoparticles in the polymer matrix we can get hybrid materials characterized by large broad band emission whose peak position depends on the hybrid type.

These are only two of many examples where the interplay of COPs with inorganic materials works together to enhance device properties.

The aim of the work is the realization of hybrid nanocomposites materials synthesizing CdS nanoparticles by thermolysis in conducting organic polymers such as Poly(N-vinylcarbazole) (PVK) and Poly (3-Hexylthiophene) (P3HT). The hybrid organic-inorganic functional materials were investigated in order to use them in energy-related devices capable to produce, convert or save energy.

5.1.1 Electronic properties of conductive organic materials

Almost all the organic semiconductors as well as macromolecules dyes, dendrimers, oligomers and polymers employed in various technological applications are based on conjugated π electrons. A conjugated system occurs in an organic compound which has a framework of alternating single and double carbon-carbon bonds. Single bonds are referred to as σ-bonds and are associated with a highly localized electron density in the plane of the molecule, and double bonds contain a σ-bond and a π-bond, where the π-bond is the overlap between p_z orbitals of neighboring atoms along the conjugation path. The conjugation of single and double bonds establishes a delocalization of the electrons situated above and below the plane of the molecule. This electronic delocalization provides the "highway" for the charge mobility along the molecule chains. π-bonds are either empty (called the Lowest Unoccupied Molecular Orbital - LUMO) or filled with electrons (called the Highest Occupied Molecular Orbital - HOMO). In the organic semiconductors the intermolecular forces (Van der Waals forces) are weak, and the charge transport proceeds by hopping between localized states rather than transport within a band. This means that charge carrier mobility in organic materials is smaller than in inorganic semiconductors. The π electrons allow light absorption (solar cells) and emission (OLEDs) in the conjugated organic materials. The photon absorption produces excitons and it is from this optically excited neutral state that free charge pair can be provided. Nevertheless the charge separation is quite difficult in organic semiconductors due to their low dielectric constant.

5.1.2 Poly(N-vinylcarbazole) (PVK)

Poly (N-vinylcarbazole) (PVK) is a highly processable organic semiconducting polymer [4] It is a hole transport material (hole mobility is much larger than electron mobility) exhibiting an emission spectrum that, owing to the properties of carbazole groups, covers the entire blue region [5] Morphologically, PVK is constituted by linear chains of repeated molecular groups $(H_2CHC)_n$, with pendant carbazole side groups $(C_6H_4)_2NH$, arranged randomly around the same chain (Figure5.1). Due to the bulkiness of the carbazole groups, the main chain and size group motion are severely restricted in PVK. As a consequence the chain is stiff and the glass transition temperature is among the highest in vinyl polymers, as we have proved by DSC measurement (Tg$\sim 226^oC$).

A detailed analysis of electronic transitions in the polymer [6] showed that four distinct bands attributed to $\pi \rightarrow \pi^*$ electronic transitions were observed at 345nm (^1L_b), 295nm (^1L_a), 262nm (^1B_a) and 237nm (^1B_b) (using the Platt notation [7]) The fluorescence spectrum of PVK results from the radiative decay of two spectrally distinct excimers, one at long wavelength (420nm) and the other at shorter wavelenght (380nm).

Similarly to what occurs for other polymers, the electrical conduction in PVK is ruled by both field assisted and temperature activated hopping processes. Besides we have to consider that the PVK charge carrier mobility is highly influenced by the trapping

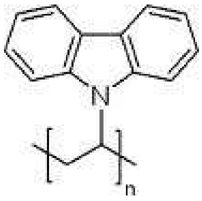

Figure 5.1: *Molecular structure of Poly (N-vinylcarbazole)*

of charge at the excimer forming sites. PVK is being currently utilized in the fabrication of blue light emitting diodes [8] in the place of conjugated polymers, which present poor emission in blue region, because of their long π-conjugation and relatively low fluorescence quantum yields. It is studied as a hole transporting material in multilayer devices [9] as well as in blends with electroluminescenct conjugated polymers such as poly(3-alkylthiophene)[12] or poly(p-phenylenevinylene)[11]. Due to its hole transporting nature, PVK has been also widely investigated as photoactive material. It s worth saying that PVK is characterized by relatively low charge generation efficiency [12] and it absorbs only in the UV region of the spectrum. For this reasons it is generally doped with nanostructured materials such as nanotubes [13] or nanoparticles [14] in order to increase its photoconductivity and to extend it in the visible range.
Given its wide range of applications, PVK is a good candidate to study the synthesis of CdS nanoparticles by thermolysis into a carrier-transporting polymer and thus to investigate the optical and electrical properties of an interesting class of materials for several technological applications, the PVK-CdS nanocomposites.
In this work we focus on the influence of CdS nanoparticles on the transport charge carriers in the nanocomposites. The fundamental issues we want to stress are whether the introduction of CdS nanoparticles into a polymer matrix causes any noticeable improvement of carrier transport and whether the synthesis of nanocomposites in situ is favorable respect to the ex situ methods.

In the next section we describe the procedure to realize PVK-CdS nanocomposites by thermolysis of Cd dodecanethiol, $Cd(SC_{12}H_{25})_2$, and discuss their optical and morphological properties varying the annealing condition. The subsequent section is dedicated to the realization process of simple stack devices using the PVK-CdS nanocomposite as active layer. We describe the results of electrical characterization making a comparison with PVK-CdS nanocomposites obtained both by combining the polymer with CdS nanoparticles purchased from NN-LABS, LLC and by mixing PVK and CdS nanoparticles synthesized in Octadecene. At the end of the chapter we make some conclusions about the improvement of carrier transport property induced by nanoparticles in all the investigated cases.

5.2 Synthesis and characterization of PVK - CdS nanocomposites

The PVK used in this work was purchased by Sigma Aldrich. It was first characterized by thermal analysis. In particular TGA and DSC measurements were performed on the original $Cd(SC_{12}H_{25})_2$ (C12) powder, already used for the synthesis of CdS nanoparaticles in octadecene and in Topas. The measurements were carried out in a dynamic nitrogen atmosphere from RT to 600^oC (400^oC for DSC experiments) at heating rate of $10^oC/min$, using a sample weight of about 15 mg in aluminum crucibles. For TGA and DSC analysis Jupiter $TA-2590$ and a Mettler DSC 822E instrument were used respectively. The curves are showed in Figure 5.2 and Figure 5.3. As already discussed in Chapter 3, the TGA and DSC curves of the Cd precursor show that the melting of the thiolate molecules occurs at 128^oC, the onset of temperature for thermal bond cleavage of C12 is at about 230^oC and the decomposition of the thiolate precursor is complete at 370^oC with a residual of about 35%. The DSC spectra tell us that the glass transition temperature, T_g, of PVK is 226^oC. It identifies the minimum annealing temperature to be used for the thermolysis process. As a matter of fact the minimum has to be set at temperatures higher than the glass transition of PVK in order to allow the polymer chain to move and the atoms of the precursor to reorganize inside the matrix. The maximum temperature has to be set before the polymer degradation point that in the case of PVK is beyond 400^oC. The TGA spectrum of PVK-C12 shows that the amount of PVK-C12 composite above 500^oC is much lower than that of C12 (already CdS at that temperature). This effect might be in part associated to the decomposition of CdS nanoparticles induced by in-situ formation of free radicals

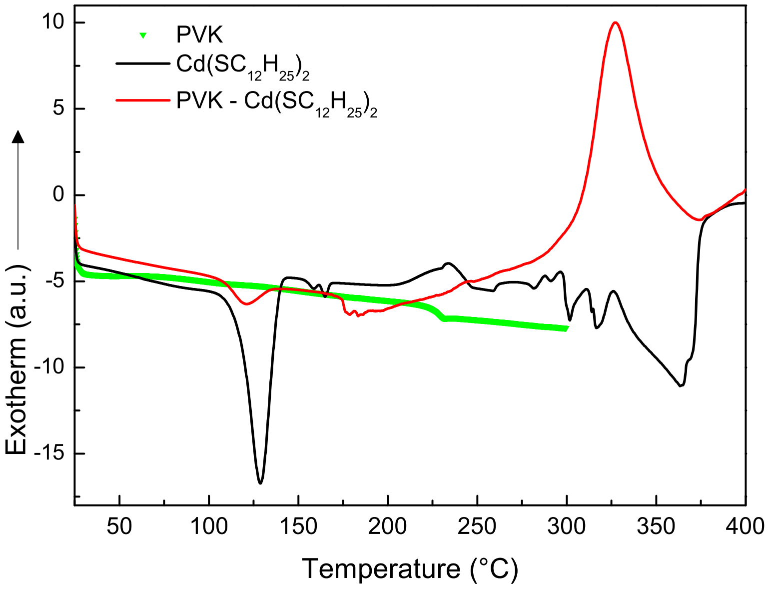

Figure 5.2: *Differential scanning calorimetry (DSC) analysis of PVK,* $Cd(SC_{12}H_{25})_2$ *and PVK-*$Cd(SC_{12}H_{25})_2$ *blend.*

species that come from the the PVK decomposition during TGA experiments. This is in agreement with the known susceptibility of CdSe nanoparticles to free radical degradation [15].

Samples preparation

The PVK-CdS nanocomposites were prepared according to the following procedure. We dissolved PVK in chlorobenzene (PVK concentration 25mg/mL) at 80^oC under magnetic stirring up to its complete solubilization. We processed the solution through a filtration stage. Then we added a stoichiometric amount of Cd thiolate precursor (20% by weight of Cd precursor in PVK corresponding to CdS/PVK ∼4% w/w) to the polymer solution under magnetic stirring. We got a white opalescent solution which was dried in a vacuum oven at room temperature over night to obtain a bulk foil.

The solid composite was annealed in a vacuum oven. The annealing process was carried out at different temperatures: 250^oC, 265^oC and 275^oC. The annealing ramp was set at about $5^oC/min$ starting from room temperature. The final temperature was

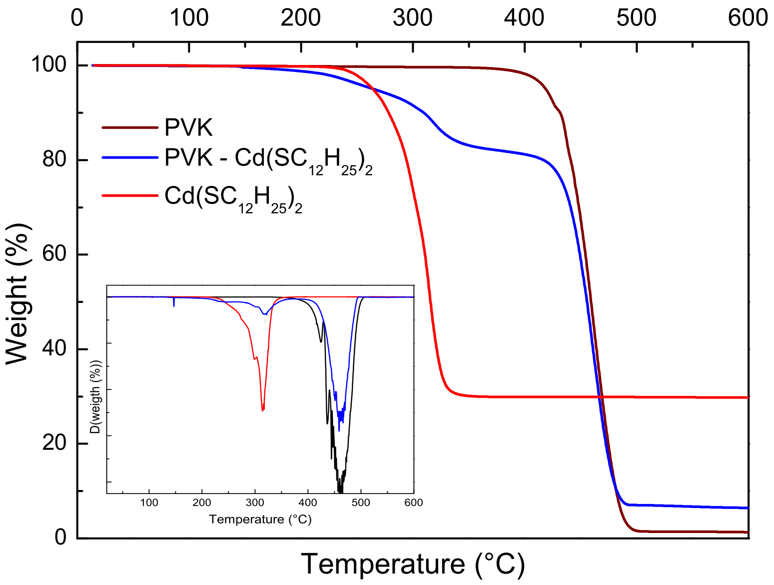

Figure 5.3: *Thermogravimetrical analysis (TGA) relative to PVK, $Cd(SC_{12}H_{25})_2$ and PVK-$Cd(SC_{12}H_{25})_2$ blend. It was performed at heating rate of $5^oC/min$ under a dynamic nitrogen atmosphere. Inset: Corresponding differential thermogravimetric analysis (DTA).*

kept constant for 20min. The process was stopped by removing the sample from the oven and allowing it to cool down to room temperature in air.

Morphological and optical characterization

In order to get morphological and structural information about the nanocomposites, the samples were investigated by transmission electron microscopy using a TEM TECNAI G2 F30 operating at 300 kV with spatial resolution of 0.205 nm. The TEM samples were prepared by dropping few μl of the PVK-CdS nanocomposite foil dissolved in chlorobenzene on a carbon coated copper grid. In Figure 5.4 Figure 5.5 and Figure 5.6 we report on the bright field TEM images of samples annealed at 250^{o}C, 265^{o}C and 275^{o}C. The images taken at low magnification demonstrate the formation of nanocrystals which appear mainly grouped in some areas where the polymer filaments are present. This effect is particularly evident for the sample annealed at 275^{o}C (Figure 5.6). Finer details in the TEM images can be hardly resolved since the organic chains are still present in the polymer film after the annealing process even in the case of high annealing temperature, reducing the image contrast. Moreover in some areas

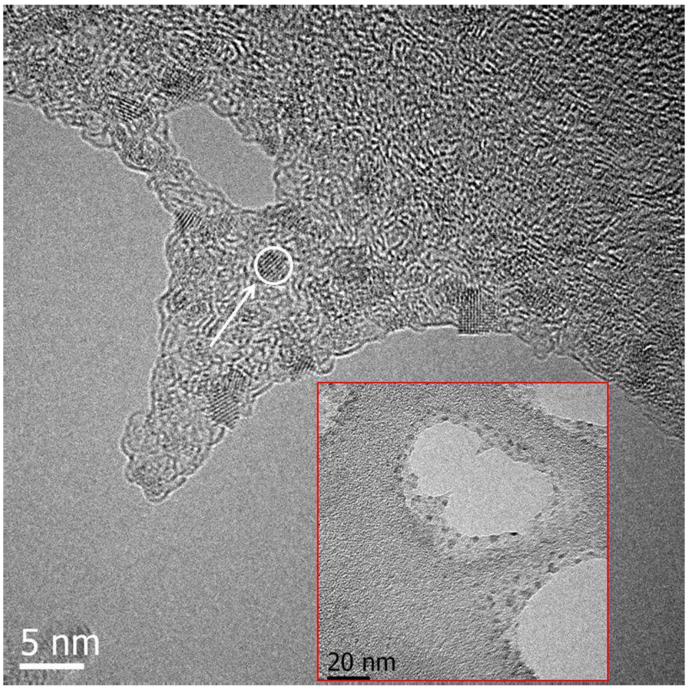

Figure 5.4: *HRTEM image of CdS nanocrystals in PVK matrix after annealing at 250^oC. The image shows the crystalline nanoparticles. Inset: Bright field TEM image over a large area.*

of the images the clusters overlap, but this is probably due to the samples preparation for the TEM.

Average sizes and morphologies on the nanocrystals were accomplished using high resolution TEM (HRTEM) at 550.000 times magnification. The HRTEM images (in the inset of Figure 5.5 and Figure 5.6) of all the samples indicate the formation of nanoparticles characterized by spherical shape regular lattice fringes at distance of 0.31nm. This result points out that the nanoparticles have a crystalline structure which can be assigned either to (111) of cubic (3.36Å) or to (002) of hexagonal CdS phase. We determined the average diameter of nanocrystallites by a statistical analysis of several low-magnification pictures of the samples. From such analysis we deduced that relatively low temperatures favor the nucleation of nanocrystals and their growth up to about 2.2nm in diameter. Higher temperatures (such as 275^{o}C) promote the Ostwald ripening process increasing both the average size (from 2.6 ± 0.5nm at 265^{o}C to 5.9 ± 2.3nm at 275^{o}C) and the polydispersity of the nanocrystals.

Local information about the elements present were obtained by energy dispersive spec-

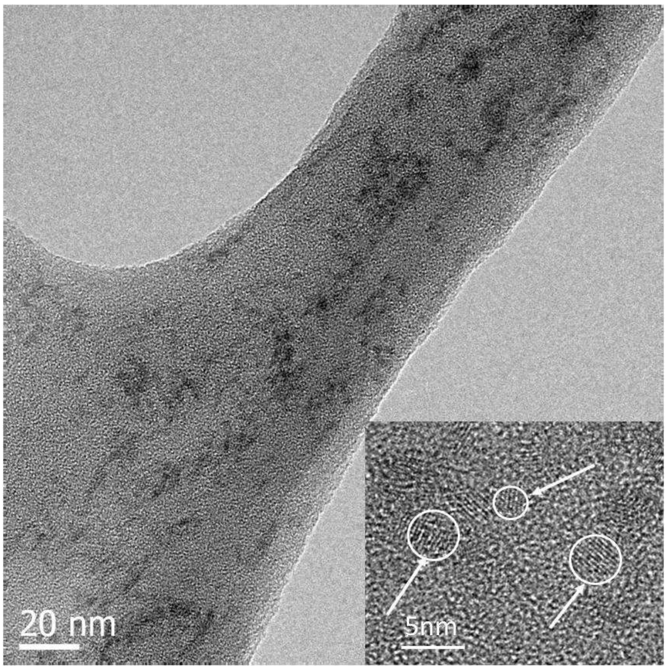

Figure 5.5: *Bright Field TEM image of CdS nanocrystals in PVK matrix after annealing at* 265^oC*. Inset: High resolution TEM image.*

troscopy (EDS) with a large area detector available on TEM. Figure 5.7 shows the EDS spectrum taken on a nanoparticle of the STEM Dark Field (HAADF) image shown in the inset. It contains both the Cd L, Cd K, S K edge peaks imputable to the sample and the peaks corresponding to C, O and Cu coming from the TEM grid.

The FT-IR analysis of PVK-CdS nanocomposite was performed on solid samples by mixing the PVK-CdS powder obtained from the foils, with KBr. The measurements were recorded by IR Nicolet 5700 FT-IR. The complex FT-IR spectra of PVK-CdS at different annealing temperatures are in general similar to that of the PVK reference and don't give more information about the creation of new functional groups in the composite. Nevertheless we noted the presence of the peak at around $2400cm^{-1}$ which can be ascribed to the -SH group of the thiol molecules. Such peak is present in the precursor as well as in the nanocomposites. Since the -SH group of thiol has a stronger interaction with the surface of CdS nanoparticles than the carbazole moiety of PVK, the peak in the FT-IR spectra could be an evidence of the fact that the residual organic chains from decomposition of dodecathiol are bounded to the nanoparticles

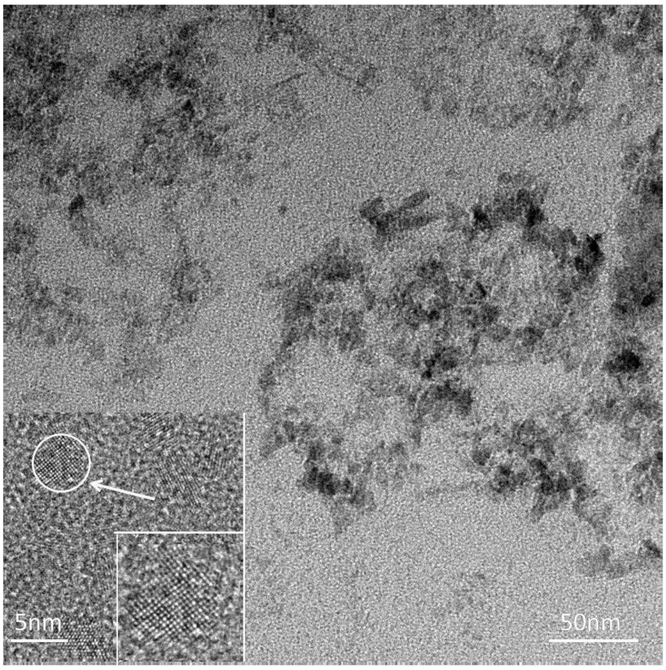

Figure 5.6: *Bright Field TEM image of CdS nanocrystals in PVK matrix after annealing at* 275^oC. *Inset: High resolution TEM image showing a crystalline nanoparticle indicated by the arrow. Further details in the blow up image.*

forming a sort of capping layer on the nanoparticles surface [16]. The characteristic vibration peaks of the Cd-S bond at 265 and $405 cm^{-1}$ were not detected in the FT-IR experiments because they are beyond the detection limit and in any case weak to be resolved.

A PVK/chlorobenzene solution is generally transparent and uncolored while the PVK-CdS nanocomposites dissolved in the same solvent appear transparent light yellow. The change of color is due to nanocrystals formation but since the polymer transparency is left unmodified we can assume that the nanocrystals are not aggregated. In other words the nanocrystals are well distributed inside the polymer matrix and almost uniform interparticles distance (much larger than the nanocrystals diameter) characterizes the nanocomposites [17]. In order to verify such hypothesis we perfomed UV-Vis absorption experiments using the Perkin Elmer Lambda 900 spectrophotometer on nanocomposites and PVK dissolved in clhorobenzene ($10^{-6} mol/l$). The PVK results essentially transparent at wavelength longer than 360nm and its absorption spectrum shows three main peaks at 295nm, 330nm and 345nm. The PVK-CdS nanocomposites

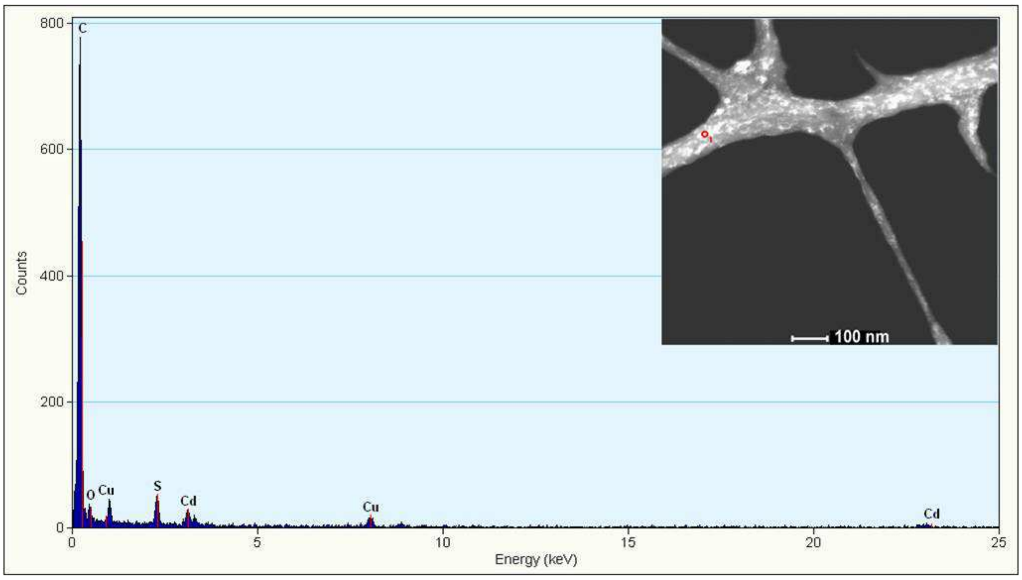

Figure 5.7: *EDS pattern of one nanoparticles of the nanocomposite PVK-CdS annealed at* 265^oC*, the nanoparticle is indicated in the inset by a red ring.*

sample	Eg(eV)	R(nm)	R(nm)from TEM analysis
250^oC	3.49	1.3	1.1
265^oC	3.36	1.4	1.3
275^oC	3.17	2.8	2.9

Table 5.1: *Energy band gap and radius (R) of nanocrystals of samples annealed at* 250^oC*,* 265^oC *and* 275^oC*, resulting from UV-Vis absorption and TEM measurements.*

are characterized by the same spectrum of PVK, with an additional tail at wavelength larger that 360nm. It can be assigned to the CdS nanoparticles (Figure 5.8).

From UV-Vis absorption curves we notice that all the samples investigated show quantum size effect since the absorption edge is blue shifted of more than 70nm from the corresponding value of bulk CdS (2.42eV). We calculated the energy band gap (see inset Figure 5.9) and the average particle size for each sample using the Brus equation which is based on the effective mass approximation for semiconductor nanoparticles [18]. The results in term of nanoparticle size are in agreement with those obtained by TEM measurements as it is shown in Table 5.1 in which the values of band gap (Eg) and nanoparticels size (radius R) calculated by both analysis are listed.

The photos of PVK-CdS nanocomposite solution under room light and under UV light

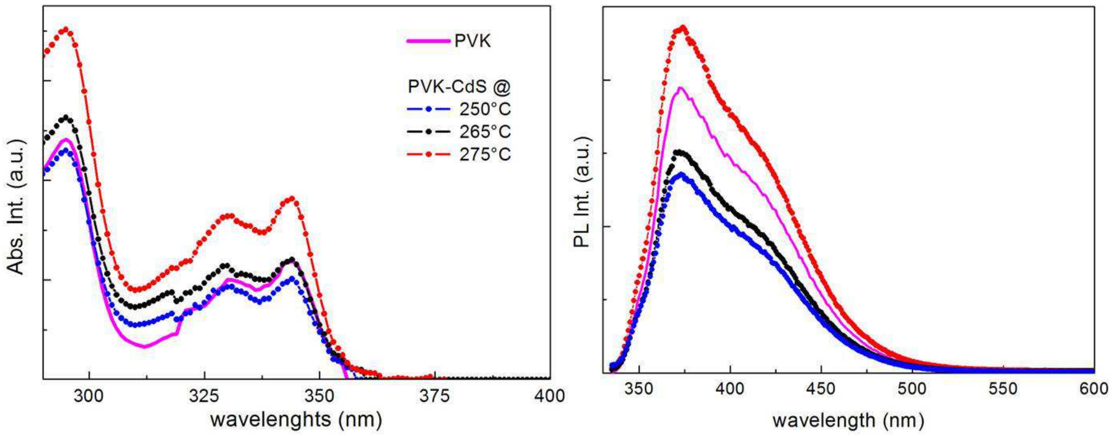

Figure 5.8: *UV-Vis absorption spectra (left side) and PL spectra (right side) relative to PVK and PVK-CdS nanocomposites.*

are shown in Figure 5.10. When irradiated with UV light the nanocomposites display a bright emission that appears light blue or yellowish depending on the nanoparticles size dispersed in the PVK. For better understanding the changes in the emission spectra from PVK to PVK nanocomposites, we measured the PL signal of PVK and PVK nanocomposites in solution by a Fluorolog 3 spectrometer (Jobin Yvon Horiba, Instruments SA). We got the emission spectra irradiating the liquid samples ($10^{-6} mol/l$) in quartz cuvette at 320nm with a band pass width of 1nm and collecting data with band pass of 5nm.

The PL spectrum of PVK (Figure 5.8 right side) shows one main peaks at about 380nm and a shoulder at 420nm as expected. With nanoparticles the emission spectra of the composites in solution remain almost similar to that of PVK reference except that a new broad emission tail appears above 450nm in the sample annealed at 275^oC. On the other hand the PL intensity of PVK is modified by the surrounding nanoparticles. In particular a quenching effect is detected when the nanoparticles are as small as in the samples at 265^o and 250^oC. In both cases the reduced PL intensity of PVK can be attributed to the quenching by interfacial charge transfer. Since the carbazole moieties in this system, coming from the PVK, are effective complexing agents with the surface of CdS clusters, the quenching of fluorescence of PVK in the nanocomposites probably results from the close vicinity of energy levels of the CdS nanoparticles and the polymer. When photons are absorbed, electrons are excited into the lowest

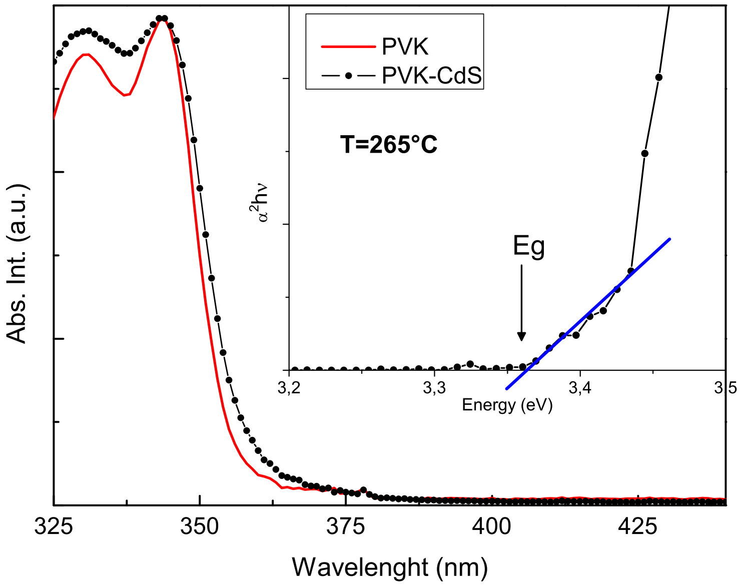

Figure 5.9: *UV-Vis spectra of nanocomposites annealed at* 265^oC *compared to that of PVK. Inset: plot of* $(\alpha h\nu)^2$ *versus* $h\nu$ *calculated from the spectrum of nanocomposite. The energy band gap (Eg) of the nanoparticles is obtained by the zero extrapolation of the curve.*

unoccupied molecular orbital (LUMO) of the carbazole groups in PVK and holes were left in the highest occupied molecular orbital (HOMO). The excited electrons, in the pure PVK solution, will return from the conduction band through a radiative process. In the system of the CdS-PVK nanocomposites, however, the excited electrons can also choose to migrate from PVK to the CdS nanoparticles. Such an interfacial charge-transfer brings down the transition probability from HOMO to LUMO and thus reduces the PVK photoluminescence. The difference between the HOMO ($2.2eV$) and the LUMO ($5.8eV$) of PVK equal to $3.6eV$, thus very close to that calculated for CdS nanoparticles. The experiments have shown that the smaller are the nanoparticles the bigger is the quenching effect. This is probably due to a better matching between the conduction and the valence bands of the CdS, in quantum regime, and HOMO-LUMO levels of PVK. Moreover the nanocomposites annealed at relatively low temperature are characterized by narrower size distribution, this result along with the relatively small size of the nanorystals can be responsible of the enhancement of PL quenching effect.

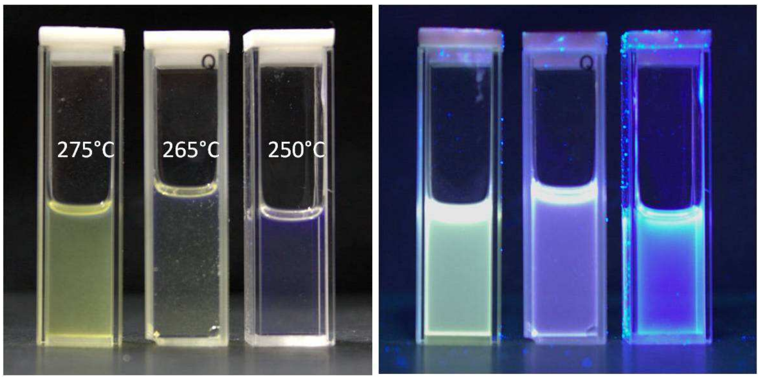

Figure 5.10: *Photo of PVK-CdS nanocomposites dissolved in chlorobenzene under room light (left side) and under UV light (right side). The annealing temperature of each sample is indicated in the photo on the left*

On the contrary we don't think that the thiol chains which come from the decomposition of dodecanethiol and surround the nanocrystals, as indicated by NMR analysis, play a critical role in the nanocomposites emission. The thiol chain are expected to be reduced at increasing annealing temperature. Consequently the nanocrystals in the sample annealed at 275^{o}C having shorter organic capping layer should be in close contact with the PVK. This could favor the charge transport through the interface between the two materials quenching the PVK PL emission, conversely in samples annealed at 250^o and 265^{o}C the nanocrystals are characterized by longer thiol chains which should inhibit the charge transfer. The experimental data don't confirm this hypothesis. As a consequence we assume that the space layer of thiols separating PVK and the nanocrystals doesn't change significantly in the range from 250^o to 275^{o}C being far from the melting temperature of dodecanhiol, thus its effect on the PL emission of nanocomposites is almost the same in all the investigated cases.

5.3 Electrical characterization of single layer PVK-CdS based devices

In order to investigate the transport properties of the nanocomposites we realized the single layer stack devices shown in Figure 5.11.

The in-situ PVK-CdS nanocomposites (PVK/CdS = 25/1 w/w) realized according the

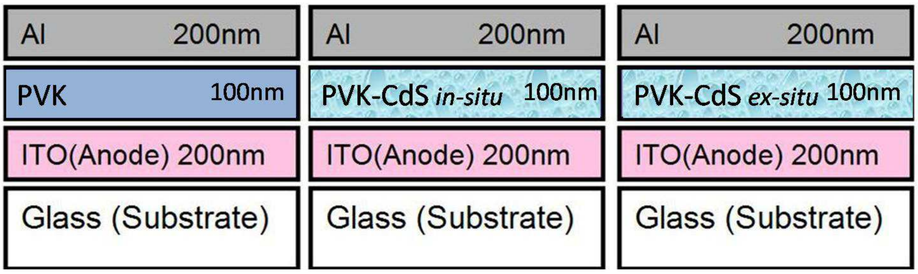

Figure 5.11: *Sketch of stack devices realized. They differ for the active layer: a) PVK, b) PVK-CdS in situ realized according to the procedure described in the previous section c)PVK-CdS ex-situ realized by dispersing in PVK commercial CdS nanoparticles (NNLabs) in one case, and CdS synthesized in ODE in an other case.*

procedure described in the previous section, were dissolved in chlorobenzene solution (25mg/ml) spun on patterned ITO (indium tin oxide) glass to form a transparent film and then heated at 80^oC for 20 min to form the active layer. The film thickness was about 100^oC, as determined by an Alpha-step IQ surface profiler. Subsequently, aluminium electrodes (area $\sim 0.7cm^2$) were deposited by evaporation through a shadow mask on the surface of the nanocomposite film.

We fabricated analogous devices with PVK only and ex-situ PVK-CdS nanocomposite as a comparison. We realized two different ex-situ nanocomposites. The first with commercial CdS nanoparticles (purchased from NN-Lab, USA) characterized by optical emission at 420nm and stabilized by a shell of oleic acid. The second with CdS nanoparticles obtained by the synthesis in octadecene described in the Chapter 3, in particular we used the nanoparticles of sample CdSODEr1 after the extraction with methanol and hexane. In both cases we added the dryed nanoparticles without any further treatment, to a PVK / chlorobenzene solution and we kept it under stirring for 24 hours before depositing it on the ITO glass substrate. The spin-coating process was carried out in ambient condition.

Before discussing the possible influence of the nanoparticles on the charge carrier transport in the composite we define some parameters describing the nanocomposite material. First of all the diameter of the nanoparticles, d, and the volume fraction of nanoparticles, x. It is related to the mass fraction g as follows $x = \frac{g}{\rho_n/[g/\rho_n+(1-g)/\rho_p]}$ where the density of CdS nanoparticles and polymer are equal to $\rho_n = 4.8g/cm^2$ for

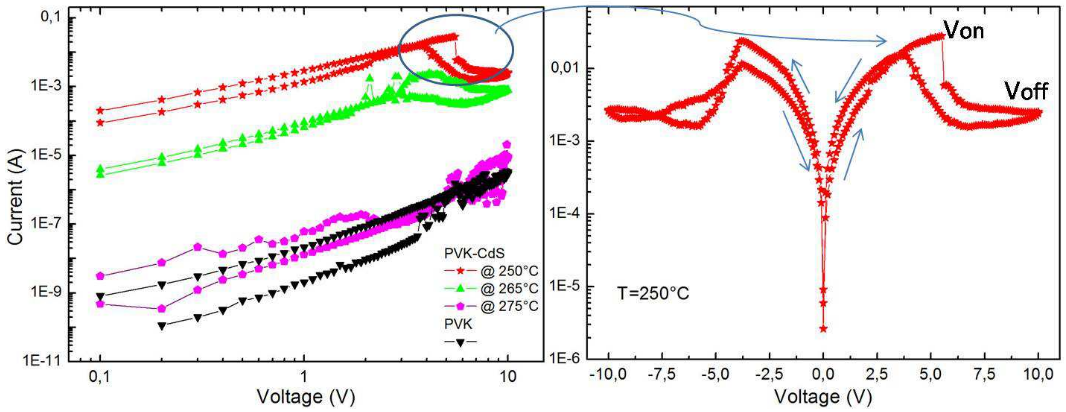

Figure 5.12: *Log-log diagram of I-V characteristics of of PVK and of the nanocomposites in-situ annealed at* 250^oC*,* 265^oC*,* 275^oC *respectively. The circle highlights the particular behavior of the sample annealed at* 250^oC*, showed in more details in the figure on the left. It presents the I-V hysteresis curve of the device ITO/PVK-CdS(250C)/Al at room temperature.*

CdS nanoparticles and $\rho_p = 1.2g/cm^2$ respectively. Since the CdS weight fraction is 4 % with respect to the polymer, we obtain that the nanoparticle volume fraction is $x = 0.01$. Given the CdS volume fraction, we define the concentration of the nanoparticles as $N = 6x/\pi d^3$ (N=0.001) and the average distance between the center of the nanoparticles which can be approximated as $r_m = N^{-1/3}$ ($r_m = 9.1nm$). Since there is no evidence of regular distribution of nanoparticles in the polymer matrix we assume that the nanoparticles are randomly distributed and the average distance between the nanoparticles is given by r_m.

To investigate the effect of CdS nanoparticles into the PVK film in term of electric properties we examined the I-V characteristics in ambient condition with a Keithley 2400 semiconductor parameter analyzer. Current-voltage (I-V) measurements were performed by sweeping the voltage from 10 to +10 V and then back to 10 V. The forward bias indicates that the ITO electrode is positively biased. The current-voltage curves obtained with forward bias are shown in Figure 5.12 and Figure 5.13.

The first important result, clearly shown in Figure 5.12 (left side), is the enhancement of current adding nanoparticles in the polymeric active layer. The degree of enhancement is high (about 10^6) for small nanoparticles as confirmed by I-V curves corresponding to PVK-CdS nanocomposite annealed at 250^oC. Since we assume that

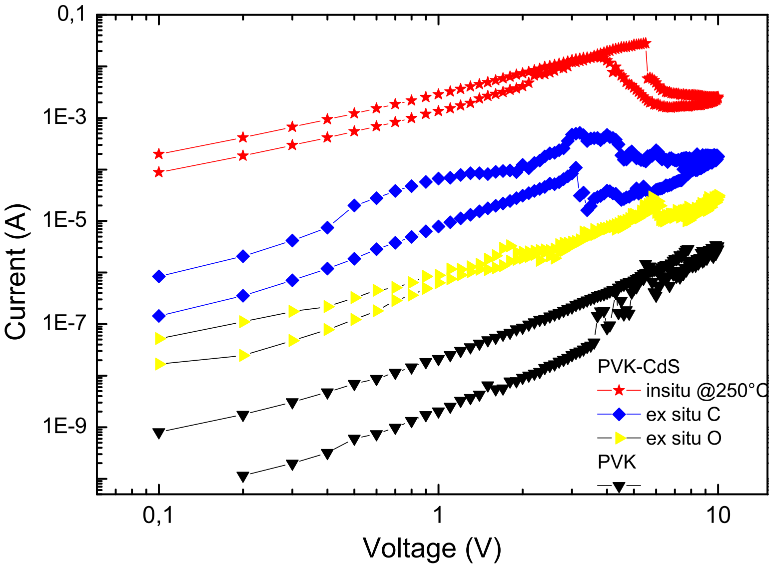

Figure 5.13: *Log-log diagram of I-V characteristics (forward and back I-V curves) of the nanocomposites in-situ annealed at* 250^oC *and ex situ with commercial CdS nanoparticles, ex-situ C, and with CdS from ODE synthesis, ex-situ O. Two consecutive I-V measurements are shown for each sample.*

the nanoparticles are randomly distributed in the polymer film, the enhanced transport properties of the nanocomposites cannot be due to the formation of well defined paths inside the matrix, generally induced by the regular distribution of nanoparticles [19]. Moreover since the CdS nanoparticle volume fraction is relatively low we can assume that the transport in our samples proceeds mostly through the polymer and is only modified to a certain extent by the nanoparticles. Nevertheless upon the application of external voltage, PVK carbazole groups may donate their electrons to the nanoparticles to increase the hole concentration and the conductivity of the polymer. Concerning the different degree of current enhancement provided by the different samples, we attribute such effect to both the interface between the matrix and the nanoparticles and the aggregation process. In the case of active layer with commercial CdS the transfer of charge from the nanoparticles into the surrounding matrix can be partially inhibited by the capping layer of oleic acid. Whereas in the other cases trapping can occur at the surface of nanoparticles which are not well stabilized by thiols. More in general

we think that the aggregation process induced by the mechanical mixing in the ex situ nanocomposites and by the high annealing temperature in the in situ nanocomposites could be one of the most important factor in influencing the charge transport.
A bistable along with an unusual property of negative differential resistance (NDR) were also observed in the high conductivity state. The electric curves develop as follows. Starting from 0V the current increases by several orders of magnitude until it reaches the maximum at voltage $V = V_{ON}$ then it goes through a NDR region to a minimum ($V = V_{OFF}$). When the voltage is decreased towards zero, the current approximately follows the same path. It remains in the OFF state until the voltage near V_{OFF} is applied then the devices is set in the ON state. Analogous behavior is observed for negative applied bias, presenting a NDR region at the same value of applied electric field. This effect is particularly evident for nanocomposites prepared in situ at 250^oC with the V_{ON} voltage in the range 4-6V and the ON/OFF current ratio of about 10. As a first attempt in explaining both the bistable and the NDR effects observed we take into account the possibility that the CdS nanoparticles may act as deep charge trapping sites to store a great deal of carriers stably. It has been reported previously in the literature that trapping of charges by impurities or trap levels can induce hysteresis and bistability [20] [21]. According to this hypothesis the NDR effect could result from a trapping and detrapping of the electrons in the nanoparticles, a process driven by the bias applied.

For devices with larger nanoparticle size the NDR effect is reduced. The reduction occurs also for devices with ex-situ nanocomposites (Figure 5.13). This result suggests that the phenomena observed are related to the quantum size effects in nanoparticles as small as 2-3nm in diameter. Consequently the same effects cannot observed for the in situ nanocomposites at 275^oC because of the formation of nanoparticles with diameter larger than the Bohr exciton radius. Moreover the narrow size distribution of the nanoparticles of the sample annealed at 250^oC may also contribute to the broadness of the NDR effect. On the other hand for the ex situ nanocomposite the reason may lay in the large size distribution of nanoparticles (see Chapter 3) and in the aggregation process induced by dispersing the nanoparticles in the polymer. In addition the general low V_{ON} /V_{OFF} ratio is due to the fact that the electrical measurements were performed at room temperature thus thermal effects also contributed to the overall conduction mechanism.

Such devices don't show light emission up to 10V because holes and electrons cannot efficiently recombine to form excitons. On the other hand we didn't increase the voltage bias further because in this way we could have easily induced a serious damage to the aluminium cathode due to the lack of a hole blocking layer in the stack devices.

5.4 Conclusions

In this work we succeeded in synthesizing CdS nanocrystals of few nanometers in diameter in PVK. The CdS nanocrystals were prepared in situ by thermolysis of Cd bis thiolate precursor in the PVK matrix as a solid bulk. CdS nanocrystals 2-3 nm sized are produced keeping the temperature at 265^oC for few minutes. The nanocrystals, predominantly in the hexagonal phase, increase in size with the annealing temperature. Despite the fact that the annealing temperature necessary to allow the thermolysis of Cd precursor in PVK is much higher than in the case of thermolysis in octadecene (see Chapter 3), the nanoparticle size in the PVK matrix is up to one order of magnitude lower than in the colloidal synthesis. This result can be explained by considering that the nanoparticles formation depends on the precursor organic chain mobility induced by temperature and it is limited by the presence of polymer chain in which the precursor is encapsulated [22]. As a consequence, the CdS nanoparticles formation is a more controllable process in a polymer matrix than in a solvent. The thermolysis of Cd thiolate precursor is then more effective in terms of small and uniform size production and reproducibility when it occurs in a polymer matrix.

Moreover we observed a reduction of photoluminescence for nanocrystals of small size. This effect has been ascribed to an increase of charge transfer between PVK and CdS. The opposite effect was observed increasing the size and polydispersity of the nanocrystals. The transfer of electrons is expected to favor the conductive properties of the nanocomposites. We found that the nanoparticles partially modify the dispersive transport in the matrix indeed. The conductivity of the organic layer is enhanced up to six order of magnitude. Moreover a NDR behavior has been observed when the devices is biased at about 5V. This behaviour is very sensitive to the nanoparticle properties, in particular to their size and size distribution in the polymer matrix. The device with in-situ nanocomposite annealed at $250^o C$ exhibits the best performances with a reproducible NDR behavior. We deduced that in order to obtain devices with well controlled NDR and bistable behaviour, the nanoparticles should be smaller than 3nm and uniformly distributed. Such devices can have promising applications in memory cells and analog oscillators.

Bibliography

[1] H. Shirakawa, E.J. Lois, A.G. McDiarmid, C.K. Chaing, A.J. Heeger, J Chem Soc.Comm. 16, 578 (1997).

[2] J.H. Burroughes, D.D.C. Bradley, A.R. Brown, R.N. Marks, K. Mackay, R.H. Friend, P.L. Burns, A.B. Holmes, Nature 347, 539 (1990).

[3] A. Pron, P. Ranno, Prog.Polym.Sci. 27, 135(2002).

[4] G. Gustafsson, Nature 357, 477 (1992).

[5] M. Pope, *Electronic processes in organic crystals and polymers*, 2nd ed. Oxford University Press, 1993.

[6] G.E. Johnson, J. Phys. Chem. 78,1512 (1974).

[7] J. R. Platt, J. Chem. Phys. 17, 484 (1949).

[8] J. Kido, Appl.Phys. Lett. 63, 2627 (1993).

[9] T. Ostergard, A.J. Pal, H. Stuub, Synth. Met. 85(1-3), 1249 (1997).

[10] G. Wuang, C. Yuan, Z. Lu , Y. Wie, J. Luminescence 68, 49 (1996).

[11] C. Zhang, H. Von Segern, K. Pakbaz, B. Kraabel, H.W. Schmidt, A.J. Heeger, Synth. Met. 62, 35 (1994).

[12] Y. Wang, N. Herron, J. Luminescence 70, 48 (1996).

[13] S. Zhang, Y. Li, J. Li, L. Liu, Y. Qin, Z.-X. Guo, L. Dai, C. Ye, D. Zhu Macromolecules 36, 6286 (2003).

[14] J. Cheng, S. Wang, X.Y. Li, Y. Yan, S. Yang, C.L. Ynag, J.N. Wang, W.K. Ge Chem. Phys. Lett. 333, 375(2001).

[15] W.H. Guo, J. Li, Y.A. Wang, X.G. Peng, J. Am. Chem. Soc. 125, 3901 (2003).

[16] S. Wang, S. Yang, S. Ynag, Z. Li, J. Wang, W. Ge, J. Phys. Chem. B 104, 11853, (2000).

[17] G. Carotenuto, F. Nicolais, Materials 2, 1323 (2009).

[18] L. Brus, J. Phys. Chem. 90, 2555 (1986).

[19] J. Jeszka, J. Ulanski, M. Kryszewski, Nature 189, 390 (1981).

[20] L.D. Bozano, B.W. Kean, V.R. Deline, J.R. Salem, J.C. Scott, Appl. Phys. Lett. 84, 607 (2004).

[21] R.J. Tseng, J. Ouyang, C.W. Chu, J. Huang, Y. Yang, Appl. Phys. Lett. 88, 123506 (2006).

[22] T. Di Luccio, A. M. Laera, L. Tapfer, S. Kempter, R. Kraus, B. Nickel, J. Phys. Chem. B 110, 12603 (2006).

Chapter 6

Poly(3-hexylthiophene) based nanocomposites for solar cell and OLED applications

In this Chapter we present the synthesis of CdS nanoparticles in a largely exploited conductive polymer, the Poly(3-hexylthiophene) (P3HT) for solar cell applications. After a brief digression on the principle of operation and the advantages of realizing organic based solar cells we report on the realization process of P3HT-CdS nanocomposites and stack devices as solar cell and organic light emitting diode prototypes. We show the photocurrent measurements performed on different P3HT-CdS based devices, and the response of P3HT-CdS nanocomposite as active material in a single layer organic light emitting devices (OLEDs). The experiments were carried out in collaboration with the Prof. De Crescenzi's group in the Departments of Physics of University of Roma "Tor Vergata".

6.1 Introduction

In the last decades many efforts have been driven to the production of low cost photovoltaic modules. In this framework organic semiconductors have been indicated as a less expensive alternative to inorganic semiconductors as well as less energy consumer [1].

As already mentioned in the introductive sections of Chapter 4, the organic absorber films can be regarded as a semiconductor-like material, where the band gap corresponds to the difference between the LUMO and the HOMO. Upon light absorption, the molecules are excited from the fundamental to the excited state realizing a singlet transition. Singlet-singlet transitions are very efficient similar to direct transitions in inorganic semiconductors. They have short life time. They can go back to the ground state through luminescence or phonon emission. Another exciton decay channel is through a lower triplet state. Triplet excitons have an increased lifetime (in the order of μs) because they cannot be deexcited radiatively, it is equivalent to indirect transition, triplet state can diffuse over large distance up to 100 μm. Both singlet and triplet excitons can provide charges for photovoltaic (PV) cells.

The majority of organic semiconductors have band gaps higher than 2.0 eV. This property can be, at least partly, managed by varying the polymer chain length. Anyway organic material are characterized by a high absorption coefficient. In some conditions 100 nm thick organic layers can absorb up to 90% of light. On the other hand the exciton diffusion range (L_{ex}) in organic materials before de-excitation is around 10 nm, which means that the distance between an exciton creation site and a dissociation site (interface) should not be higher than 10 nm. Moreover, since the charge mobility is very small, there is large probability that the charges recombine during the way to the electrodes. This results in very low power conversion efficiencies achieved (10^{-6}%) in the organic solar cells.

Concerning the solar cell architectures, different architectures can be developed. In the single layer cells both positive and negative photo-excited charges travel through the same material, consequently the recombination losses are high. In bi-layers cells the charge transport occurs in two different layers decreasing the recombination probability of the carrier. However in this case the active domain, that is the donor/acceptor interface, is still very small and only excitons near the depletion layer can reach it and become dissociated. An alternative is the bulk (or dispersed) heterojunction (BHJ) cell like a blend of donor and acceptor materials.

The new concept of bulk heterojunction is used to overcome the limited cells efficiency observed in single layer cell or in multilayer cell. In fact the BHJ PV cells offer much greater IPCEs due to

- the decreased distance the excitons must diffuse to reach the interface, in other words the average acceptor/donor phase domain size (L_{pol}) is less than L_{ex}

- the much greater area of the acceptor/donor interface.

In the past decades significant progress has been reported for the bulk heterojunction photovoltaic devices starting from solution processed p-type conjugated polymers, either in combination with polymers [2] or fullerenes [3] [4]. On the other hand nanocomposites realized by inorganic nanoparticles embedded in a polymer matrix would benefit of the complementary properties of organic and inorganic materials in particular they can be processed as the polymers and thin films can be realized by spin coating or printing techniques on flexible substrates. In solid state photovoltaic devices formed by such nanocomposites the light is absorbed by the polymer and the photoproduced excitons can diffuse to the interface with the nanoparticles. Because of a relative positive electron affinity, nanoparticles accept electrons from the polymer under illumination. In other words the polymer acts as p-type material and the nanoparticles as a n-type material [5] [6]. Thus an internal field is created by contacting the p-type and the n-type materials and it can separate the electron-hole pairs. The insertion of nanoparticles in a solar cell active layer is also particularly interesting because of the peculiar properties of inorganic material at nanometric size. First of all the nanoparticles have size dependent Eg and energy levels depending on their size. This provides a tool for tuning J_{SC} in a solar cell devices [7]. Material at nanometric size are characterized by a large surface area to volume ratio ensuring an extended interfacial area for charge transfer [8]. In addition the inorganic nanoparticles can harvest light offering potential contribute to the spectral coverage and photocurrent.

In this framework nanodispersed heterojunction based on semiconductor nanoparticles and conjugated are subjected to intense studies. It has been demonstrated that the nanoparticle geometry and aspect ratio, the its concentration as well as the nature of the nanoparticle-polymer interaction are important factors governing the IPCE of inorganic nanoparticlepolymer PV cells [7].

One of the main challenge for nanocomposite film preparation is getting uniform distribution of nanoparticles inside the polymer matrix in order to maximize the number of interfaces between the nanoparticles and the polymer. That is not obvious if the

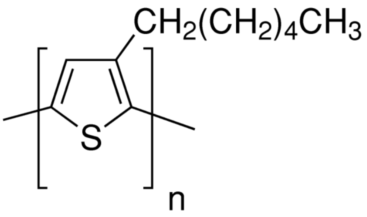

Figure 6.1: *Chemical structure of poly(3-hexylthiophene), P3HT.*

method used to create active layer consists of mechanically mixing inorganic nanocrystals with polymers. Since the in-situ method consists of the synthesis of nanoparticles in the polymer matrix, it can allow a better nanoparticle dispersion in the polymer itself reducing the difficulty generally encountered in ex-situ dispersed heterojunction such as the solid state miscibility and stability.

6.1.1 Poly(3-hexylthiophene) (P3HT)

Among the several parameters which influence the organic cells performances, the most important is the absorption efficiency of the photons of the solar spectrum. To achieve a good overlap between the polymer absorption spectrum and the solar spectrum, polymer with band gap smaller than 2eV must be used. A review of such polymers has been proposed by E. Bundgaard and F.C. Krebs [9] Most of low band gap polymers encountered in the literature are based on thiophene. In particular poly(3-hexylthiophene), P3HT, has a band gap of 1.9 eV and it is one of the thiophene derivatives which has been systematically investigated for solar cell applications [10] [11]. It is a regioregular polymer belonging to a class of conjugated polymers, poly(3-alkylthiophene)s (P3AT). P3ATs are highly conductive polymers, soluble and environmentally stable. These properties enable PATs to be significantly useful in a wide variety of applications ranging from chemical and optical sensors, light emitting diodes, display, memory devices and solar cells [12]. Thin films of P3HT adopt a highly microcrystalline and anisotropic lamellar microstructure comprising two-dimensional conjugated layers with strong $\pi - \pi^*$ interchain interactions separated by layers of insulating side chains (Figure 6.1). This microstructure leads to fast in-plane charge transport. The mobility of P3HT depends very sensitively on the degree of head-to-tail, head to head or tail to tail regioregularity of the molecules, and on the deposition conditions. Lots of processing factors influence the P3HT properties. It has also been proved, for instance, that annealing treatments of the polymer can induce the spectral absorption broadening and the improvement the crystallinity of the polymer resulting in an increase of the carrier mobility [13] [14].

6.2 Synthesis and characterization of P3HT-CdS nanocomposites

In this paragraph we report on the synthesis of CdS nanoparticles in Poly(3-Hexylthiophene). The P3HT-CdS nanocomposites were prepared according to the procedure used to realize PVK-CdS foils described in Chapter 5, that is by the thermolysis of cadmium thiolate precursors $Cd(SC_{12}H_{25})_2$ mixed with P3HT (regioregular 99.995%, Mn $15.000 - 45.000$, Sigma Aldrich) chlorobenzene solution. The precursor-polymer weight ratio was set at 20% which yields CdS/P3HT 4% w/w after the decomposition. The solution was then dried and the bulk piece obtained was annealed in vacuum at 240^oC.

The preliminary thermal characterization of P3HT and P3HT-$Cd(SC_{12}H_{25})_2$ was performed by TGA and DSC measurements. The analyses were carried out in a dynamic nitrogen atmosphere from RT to 600^oC at heating rate of $10^oC/min$ by STA 449 F3 Jupiter Netzsch. The TGA measurement shows that the precursor mass loss occur around 220^oC as expected. DSC analysis indicates that P3HT has the peculiarity to start its degradation at high temperature, above 400^oC (Figure 6.2). The glass transition temperature of P3HT is a controversial issue. It is generally found at temperature beyond 20^oC [15] but we couldn't clearly identify it from the DSC analysis even heating at low rate. At 228^oC the DSC curves present an exothermic peak corresponding to the crystallization phase of the polymer. Adding the precursor the crystallization point is slightly shifted toward higher temperature (233^oC).

We annealed in vacuum the P3HT-$Cd(SC_{12}H_{25})_2$ foils at 240^oC in order to allow the CdS precursor decomposition as indicated by TGA and realize small-sized nanoparticles. In particular the sample was annealed at 240^oC for 20min according to the

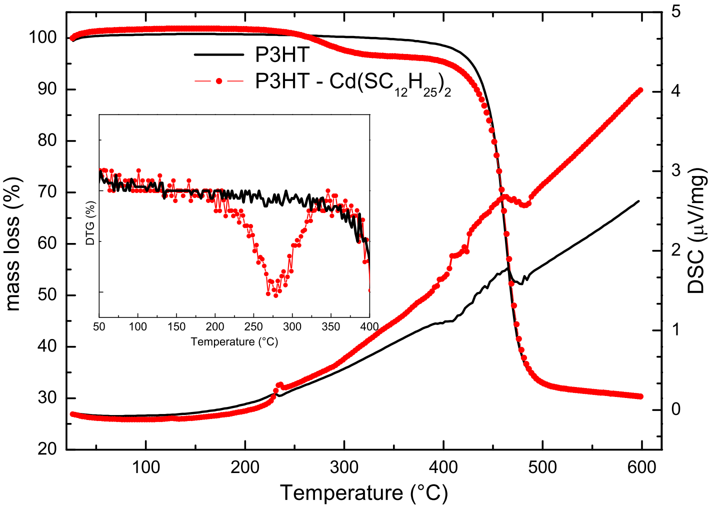

Figure 6.2: *Thermogravimetric (TGA) analysis and heat flow from standard DSC on polymer and precursor/polymer composite showing that the decomposition of P3HT starts at about* 400^oC*. The Cd precursor mass loss occurs at* 220^oC *(inset image) as expected.*

experiments performed in Topas. During the annealing process the foil changes its color from red to golden.

To investigate the formation of CdS nanostructures in the P3HT matrix, transmission electron microscopy (TEM) measurements were performed using a 100 keV JEOL system, in collaboration with the Electron Transmission Microscopy Laboratory of ENEA C.R. Brindisi. The samples for TEM were prepared by dissolving few mg of annealed nanoparticle-polymer foil in few μl of chlorobenzene. This solution was drop cast on Cu grids 3.05 mm in diameter and 300 meshes. TEM analyses of the sample prove the formation of CdS nanoparticles. In this particular case, small and spherical nanoparticles are present in the polymer, as shown in Figure 6.3. The HRTEM image in the inset shows regular lattice fringes at a distance of about 0.31 nm as found in the PVK-CdS samples. Statistical analysis over about 100 nanoparticles has given a narrow nanoparticle size distribution peaked at about 2.5 ± 0.7nm.

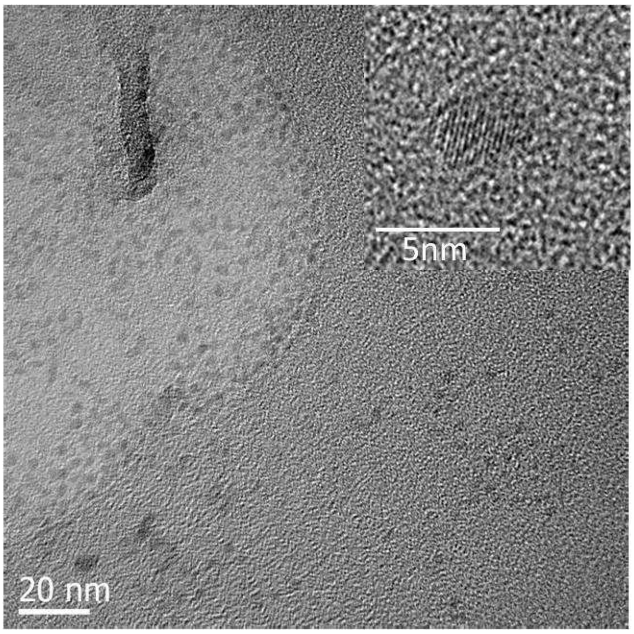

Figure 6.3: *Bright field and HRTEM images (inset) of P3HT/Cd precursor nanocomposite after annealing at* 240°*C. The annealing conditions used favors the formation of small and uniformly sized nanoparticles which also show regular lattice fringes* 0.31*nm spaced.*

6.3 Realization of P3HT-CdS nanocomposite based device

In this section we describe the realization process of stack device using the P3HT-CdS nanocomposite as active layer in order to analyze both its photoconductive and electroluminescent properties. Glass substrates (Corning 1737) with 150 nm thick indium tin oxide (ITO) layer were cleaned with deionised water, detergent and ultrasounds and dried in oven at 115°*C* for 2 hours. The ITO was patterned through inverse photolithography and HCl-based etching in order to define the anode electrode area. The P3HT and P3HT-CdS nanocomposite were dissolved under stirring in cholorobenzene at concentration of 25mg/mL. The solution was spin-coated (2000 rpm) on ITO-glass substrates and heated at 80°*C* for 20 min to let the solvent evaporate. The films were about 100nm thick, as determined by an Alpha-step IQ surface profiler. Subsequently Lithium Fluoride (LiF) $\sim$ 1nm thick and aluminium electrodes 200nm thick were deposited by evaporation through a shadow mask on the surface of nanocomposite film. The device area is $\sim 0.7 cm^2$.

ITO is suitable as transparent conductive oxide (TCO) because it provides high transmission T in the visible spectral region(T $\sim$ 90%) and sheet resistance around 10Ω/square. The LiF layer between the active layer and the aluminium cathode is generally used to improve the organic optoelectronic devices performances. The effect of LiF on the optoelectronic performances is often described in organic light emitting devices (OLEDs) [16]. The increase in luminance and efficiency is attributed to enhancement of the electron injection from the aluminium into the organic layer [17] In the case of solar cells, insertion of a thin LiF layer at the interface organic/aluminium could allow to improve the power conversion efficiency of the cells favoring an increase in the forward current upon reducing the serial resistivity across the contact. The optimum LiF thin film thickness has been proved to be around 1 nm [18].

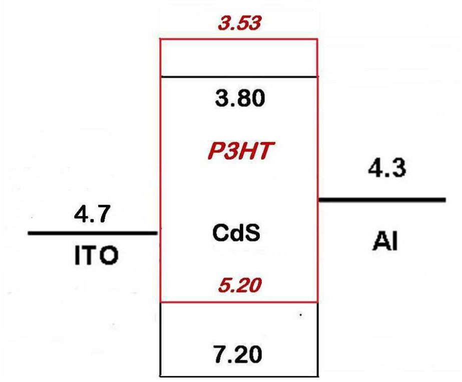

Figure 6.4: *Device energy diagram expressed in eV. The vacuum energy level is zero.*

The device realized have the following structure ITO/P3HT:CdS/LiF/Al (Figure 6.5), whereas the device ITO/P3HT/LiF/Al was used as reference. Figure 6.4 shows a schematic diagram of the theoretical work function of electrodes [19], the energy levels of P3HT [20] and of CdS nanoparticles. The HOMO LUMO levels of CdS have been valuated considering that CdS have electron affinity in the range $3.8 - 4.5eV$ [21] with band gap of $3.58eV$ as calculated from absorption spectrum of nanoparticles in Topas (see Chapter 4).

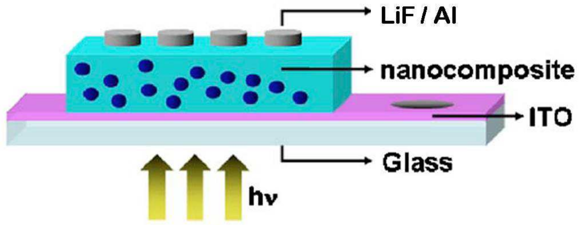

Figure 6.5: *Schematic drawing of the device used for the photocurrent measurements*

6.3.1 Photocurrent measurements

In order to evaluate the photocurrent response of the P3HT-CdS nanocomposites we measured the Incident-Photon-to-electron Conversion Efficiency, IPCE (see introductive paragraphs in Chapter 2). The IPCE spectra were acquired by optical set-up for solid state measurements. The optical set up is equiped with a 150W Xenon lamp (spectral range: from 200nm to 2400 nm) a monochromator (spectral range: 300 nm to 1000 nm), an optical chopper, focusing optics (lenses), a sample holder, a Si calibrated photodiode as a reference with amplifier, a low noise-current amplifier and an Ametek Signal Recovery lock-in amplifier (Figure 6.6). The sample and the photodiode were positioned in order to be illuminated alternatively by a mirrored chopper blade, therefore their signals were dephased of about 180^oC when no electronic induced dephasing was considered . At each wavelength from the near UV (300 nm) to the near IR (1000nm), the photogenerated current was evaluated by averaging, over tens of light/dark cycles. The dark and light current density values were subtracted each other and their absolute value was taken. The light and dark cycles were obtained by a chopper at fixed frequency (usually around 22 Hz), the signals were collected by the lock-in amplifier. The current were recorded by the Keithley 2602A source meter, positioning the spotlight (size 2 x $3.7mm^2$) at fixed distance from the sample. The photocurrent induced by dark-light cycles results to be a square signal as function of time. The photocurrent signal was used to calculate the IPCE following the Eq.2.4 (Chapter 2). The power of impinging light used to calculate the IPCE was measured by the calibrated photodiode. Figure 6.7 shows the IPCE spectrum of the polymer. The presence of several features at high wavelength ($> 700nm$) is due to the peaks of

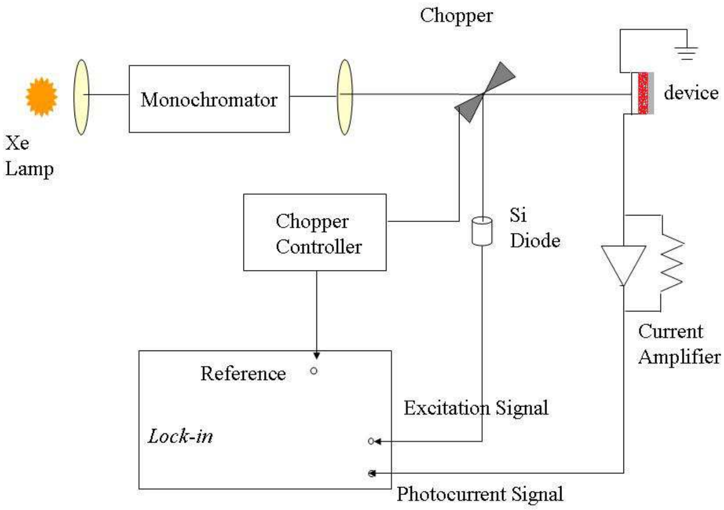

Figure 6.6: *Block diagram of the measurement set up for photocurrent measurements*

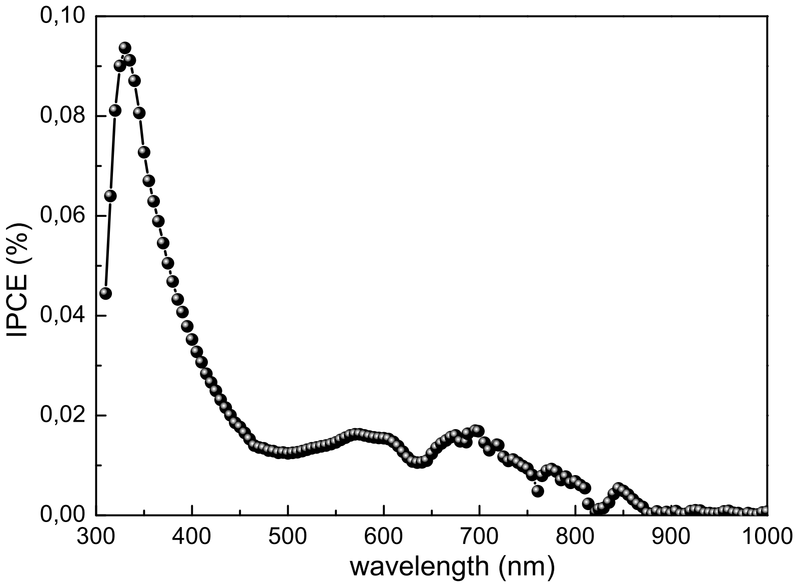

Figure 6.7: *IPCE spectrum of P3HT. The measurements were performed on a layer 100nm thick.*

the lamp spectrum.

Since the IPCE is proportional to the absorbance A(λ), as stated in the introductive paragraphs of Chapter 2, it is worth measuring the absorption spectra of the polymer and the nanocomposite. Figure 6.8 shows the absorption spectra of the polymer and

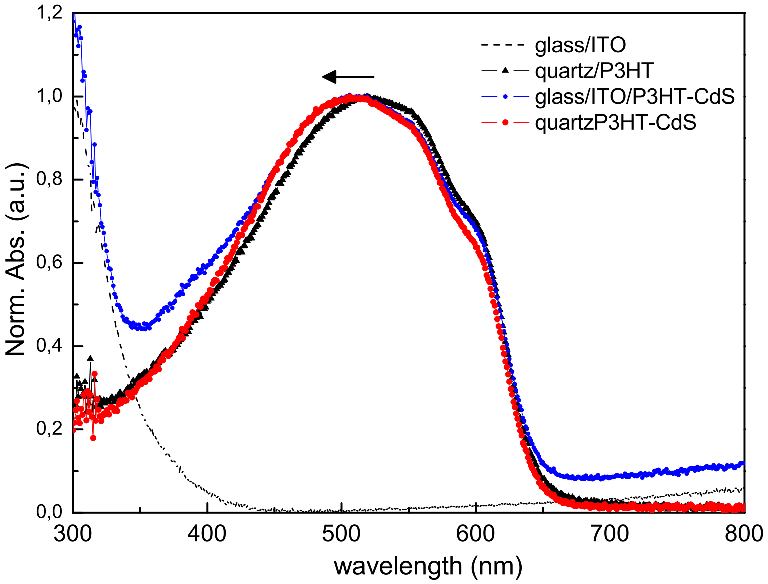

Figure 6.8: *UV-Vis absorption spectra of P3HT and P3HT-CdS nanocomposite annealed at* 240^oC. *The measurements were performed on films 100nm thick deposited on quartz substrates.*

the nanocomposite deposited on a quartz substrate (NSG OZ optical grade) and the absorption spectrum of nanocomposite deposited on glass/ITO substrate. The absorption measurements in the UV and visible region (UV-Vis) were performed on the 100nm thick films by a spectrophotometer Perkin Elmer Lambda 9.

The optical absorption spectrum of pure P3HT on quartz has a feature in the visible region spread over a large range from 350 to 650nm with a peak at 519nm (2.39eV) and two shoulders at 556nm (2.23eV) and 605nm (2.05eV). The absorption peak is attributed to the excitation of electrons in the π conjugated system [22]. The energy difference between two shoulders corresponds to 0.18eV and may be associated with the stretching frequency C=C in the polymer [23] As expected, the absorption spectrum of P3HT as thin film is red-shifted respect to P3HT in solution which presents a broad feature peaked at about 450nm. The red-shift is generally ascribed to a change in the the chain ordering in P3HT [26]. In the hybrid samples the presence of nanoparticles cannot be clearly detected. The weak signal from nanoparticles is expected to arise at about 325nm as indicated by absorption spectrum of CdS nanoparticles syn-

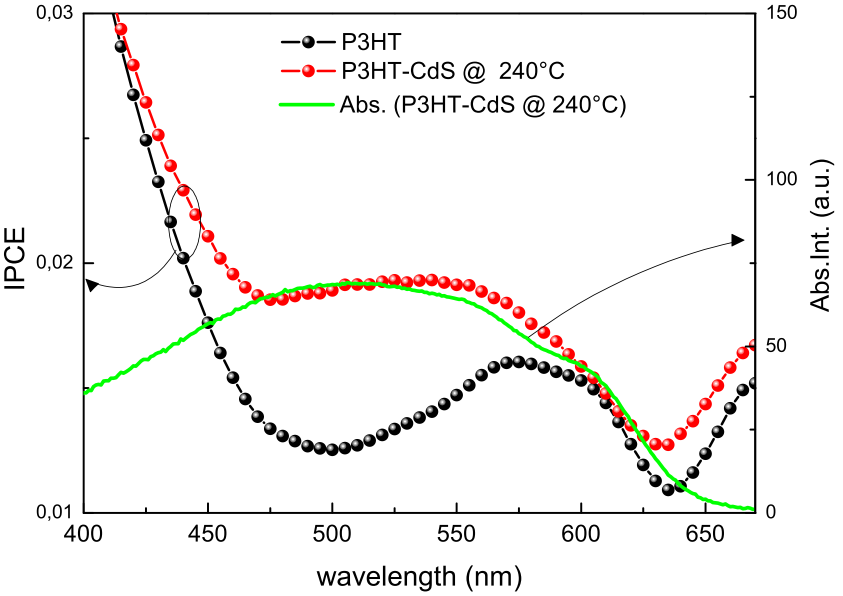

Figure 6.9: *IPCE spectra of P3HT and P3HT-CdS nanocomposite annealed at* 240^oC *(black and red dots respectively) and absorption spectrum of the nanocomposite. Note that the absorption resembles the action spectrum of the IPCE spectrum in the range 450-650nm. The measurements were performed on 100nm thick films. The absorption spectrum of a glass/ITO substrate is also shown.*

thesized in TP at the same temperature (reported in Chapter 4), but it is probably hidden by the huge polymer absorption curve. However the nanoparticles are probably responsible of the slightly blue-shift of the P3HT absorption curve (indicated by the arrow), determined by a ground state charge transfer between the polymer and the nanoparticles [29]. Such blue-shift cannot be ascribed to modification or ordered polymer chains induced by the annealing process. In fact the absorption spectrum of P3HT and P3HT annealed at 240^oC are similar. On the other hand the absorption curve of P3HT deposited on glass/ITO shows the effect of ITO on the device light absorption. It is crucial in the UV region and at high wavelength where an absorbtion tail is present.

The calculated IPCE spectra of P3HT and nanocomposite are superimposed in Figure 6.9. A slightly enhancement of the IPCE in the range 400-600nm has been detected. The absorption curve of P3HT-CdS nanocomposite, also reported in Figure 6.8, follows

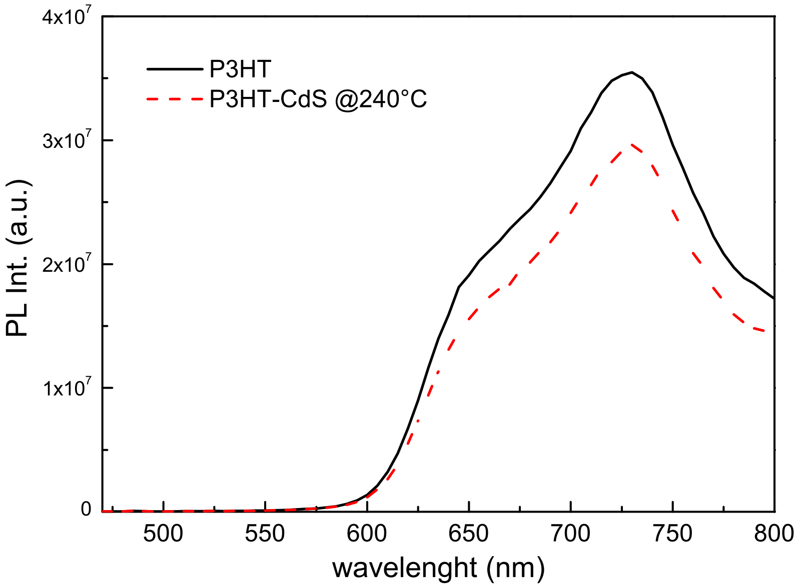

Figure 6.10: *PL spectra of P3HT and P3HT-CdS nanocomposite annealed at* 240°C. *The measurements were performed on 100nm thick films on quartz substrates. Excitation wavelength: 450nm.*

the experimental IPCE curve of the nanocomposite in the 400-600nm range, indicating that the nanocomposite contributes in improving the charge separation after exciton formation.

It is well established that P3HT is a good hole conductor characterized by high recombination because of its low mobility and short excitonic diffusion length, thus a strong photoluminescence signal is generally expected. We measured the photoluminescence emission spectra of P3HT and P3HT-CdS nanocomposite in thin films. The PL measurements were recorded by FluoroLog Jobin Yvon with 5nm band width at 450nm of excitation wavelength. The PL spectrum of P3HT in Figure 6.10 shows a shoulder at 650nm and a peak at 730nm. The PL emission features are generally assigned to the pure electronic transition and to the first vibronic band of the polymer [25].

It is interesting noting that the PL emission is quenched by adding the nanoparticles. This is a good indication of the interaction between the two component in the excited state. In particular if we consider the polymer as a donor and the nanoparticles

as an acceptor material, the PL quenching demonstrates the effective donor-acceptor charge transfer [27] [28]. As a matter of fact the PL intensity reduction is generally associated to an improvement in the photovoltaic performance [29].
As a consequence both the spectral overlap that occurs between the nanocomposite absorption and the IPCE curves in the 400-600nm range and the PL emission quenching indicate that the IPCE enhancement observed in the UV-visible region is due to the beneficial effect of nanoparticles which favor the charge separation in the photoactive material. It is worth noting that the moderate increase of IPCE is due to the small amount of nanoparticles in the nanocomposite. Since the wight ratio CdS/P3HT is 4% w/w, the volume fraction of CdS nanoparticles in the P3HT matrix is 0.01 [30]. The volume of nanoparticles used is one order of magnitude less than that reported in literature [7]. Since the interface between the nanoparticle and the matrix play a fundamental role in the charge transfer process, the main concern in realizing photoactive layer is maximizing the interface between the acceptor and the donor materials. This can be obtained by increasing the amount of nanoparticles and assuring their uniform distribution in the matrix.

Our results in terms of IPCE indicate that the photocurrent generation is mainly governed by the polymer and it is only modified to a certain extent by the nanoparticles. Therefore we assume that the photogenerated excitons mostly recombine before reaching the electrodes. Nevertheless our first attempts of realizing P3HT-CdS nanocomposites by thermolysis are encouraging because they demonstrate the advantage of in-situ method in synthesizing likely uniformly dispersed nanoparticles which allowed a slightly improvement in the performance of the photoactive material even with a small amount of nanoparticles. Concerning the complete characterization of the devices, the resistance was obtained by measuring the J-V characteristics under dark room conditions (voltage range $-0.1 < V < 0.1$, step $0.02V$) is about 74kΩ cm^2, it is 3 order of magnitude higher than reported in literature [31] Along with the resistance two characteristics parameters of solar cells, the short circuit density, J_{SC} and the open circuit voltage, V_{OC} was measured in dark and room light conditions. The J_{SC} for the nanocomposite based device is about $0.18 \mu A/cm^2$ under light conditions. Under dark conditions the J-V characteristic is lowered of one order of magnitude.

The measured values of J_{SC} are about 3 order of magnitude lower than those reported in recently published papers [32] while the value of V_{OC} around 530mV is in line with the that reported in literature. The low device performances are probably due to both the presence of defects at the interface between the active layer and the electrodes and the existence of pinhole defects in the active layer [31]. The overall performance of the solar cell could be recovered by annealing process of the deposited active layer and by optimizing the layer deposition process [31].

Starting from these first results on realizing P3HT-CdS based solar cells, next experiments can proceed by increase the precursor concentration in order to raise the number of nanoparticles, optimizing the inter-layer interfaces to reduce the defects at the electrodes and treating thermally the P3HT layer after the spin coating deposition.

6.3.2 Electrical measurements

As we have already stressed in the previous section the polymer-electrodes constitutes two semiconductor-metal junctions. The barrier between the metal and the semiconductor, Φ_B, can be identified on the energy band diagram, using a common vacuum level (Figure 6.4). The barrier height is defined as the potential difference between the Fermi energy of the metal and the band edge where the majority carriers reside, thus it is equal to the difference between the work function of the semiconductor and the metal. The stack ITO/P3HT/LiF/Al constitutes a Schottky device because Al forms a depletion layer with P3HT [33]. This depletion layer gives ITO/P3HT/LiF/Al a typical rectifying behavior resulting in a diode like current voltage. In the case of nanocomposite the barrier height at the metal junctions is in principle unknown. Consequently we are interested in determining the current voltage behavior of the nanocomposite based device. The P3HT device was also investigated as comparison. We measured the I-V characteristics of devices in dark condition at room temperature using a Keithley 2400 Power Supply Source Meter in voltage mode in the range 0 - 10V with constant increment steps and delay time of 1sec before each measurement point. Our analysis on electric characteristics was mainly focused on determining the best fitting conduction model to experimental data for forward current density (positive voltage applied at ITO electrode). Figure 6.11 shows the current density-voltage (J-V) characteristics of

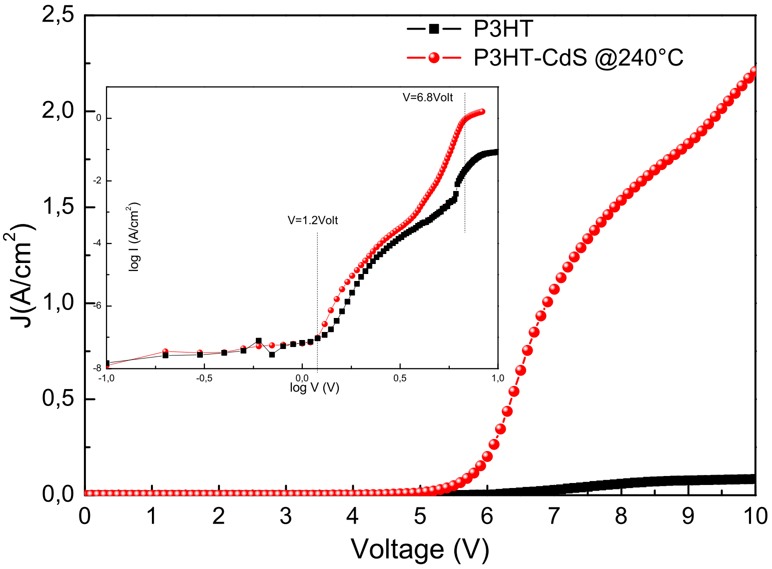

Figure 6.11: *Current density-voltage (J-V) characteristics of ITO/P3HT:CdS/LiF/Al and ITO/P3HT/LiF/Al devices. Three main conductive behavior have been detected from the logI-log V plot. The different regimes are separated by the dashed lines*

ITO/P3HT:CdS/LiF/Al and ITO/P3HT/LiF/Al devices. The inset of Figure6.11 is a plot of log(J) as function of log(V). We found that the curves fit reasonably well with the power function I $\propto V^m$, thus we calculated the parameter m from the logJ-logV curve slope. Each value of m corresponds to a conduction mechanism. For low voltage values the J-V curve of ITO/P3HT:CdS/LiF/Al roughly follows the ohmic behavior being $m \sim 1$, at V$> 1.2Volt$ the experimental data fit reasonably well with the trap limited current model (TCLC) [34] [35] being $m \geq 2$. When the applied voltage is low the current is mainly carried by the thermal charges the concentration of thermal charges is determined by the thermal equilibrium between the Fermi energy level and the conduction band of the semiconductor (Ohmic regime). When the injected charges outnumber the thermal charges, the current voltage characteristic is governed by traps. According to the TCLC model the traps are distributed in energy and are gradually filled with increasing electric field. It means that the current grows with power law increasing the electric fields. At high bias (V$> 6.8Volt$), the trapping sites are already filled and all the additional injected carriers are located in the transport level. This situation bends the curve from a voltage exponent higher than 2, towards a square law dependence typical of space charge limited current (SCLC) (J $\propto V^2$) [36][37] that is the well-known trap free model with constant mobility.

This behavior appears to be quite reasonable for the films with nanoparticles, which are generally surrounded by several surface defects. However also in polymer films there are always some traps due to some impurities or structural imperfections [38]. In fact in the case of ITO/P3HT/LiF/Al the current-voltage characteristic follows the same behavior of nanocomposite but the current density is lower of a factor 2 at 9V, moreover the SCLC is not reached at $V < 10Volt$. Anyway a large forward current density of $13mA/cm^2$ at 5V is obtained for nanocomposite with respect to $0.9mA/cm^2$ of P3HT only. The main cause of enhanced carrier transport at reduced dimensions has been ascribed to the higher electron concentration in the nanoparticles [39]. The current is then controlled by the surface defects due to non stoichiometry, such as excess of cadmium or sulfur vacancies which are responsible of Fermi level shift and thus of the activation of several conduction regimes even in the TCLC range. A relation between such defect states and the photosensitivity of CdS has been studied by Sebastian at al. [40]. They impute the enhancement of photoconductivity in nanocomposite to the presence of Cd deep acceptor states above the valence band and donor states located below the conduction band, due to S vacancies. According to their theory the impurity levels act as sensitizing centers in the photoactive materials.

The results of electrical characterization are in agreement with those of nanocomposite based device reported in literature [39].

6.4 Organic light emitting device: generalities

Electroluminescence (EL) is an optical and electrical phenomenon in which a material emits light in response to an electric current passed through it.

An electroluminescent device, OLED, consists of one or more emissive layers sandwiched between the two electrodes. The emitting layers can be an organic or hybrid organic/inorganic electroluminescent compound. The color of the light produced depends essentially on the chemical nature of the electroluminescent material.

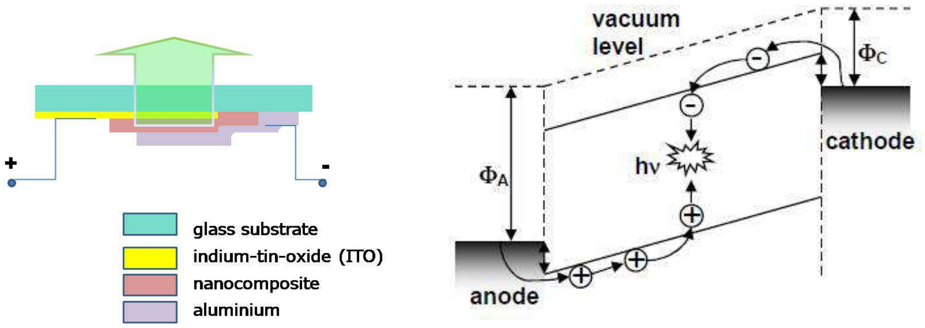

Figure 6.12: *Sketch of OLED and mechanism of light emission (left side). Schematic energy diagram of a single-layered OLED (right side).*

Figure6.12 shows a schematic drawing of OLED and the energy diagram to represent approximately how the light emission is produced.

When the externally applied field exceeds the built-in voltage (the work functions ,ϕ_A, ϕ_B of the electrodes) the charge carriers of different polarity are injected from the inorganic electrodes (anode: holes, cathode: electrons) and meet in the organic layer (Figure 6.12, right side). This usually occurs on a single molecule and is associated with exciton formation. The exciton relaxes either radiatively or nonradiatively. Generated photons leave the device through the glass substrate.
Non-radiative decay reduces the light output of the OLED (e.g its internal quantum efficiency) and is therefore undesired. This happens for instance when the recombination zone of the OLED is located close to an electrode (quenching).
The gap is an intrinsic property of the organic compound used. It defines the exciton energy and hence the electroluminescent spectrum. A very important OLED property is specified by the external quantum efficiency, η_{ext}. It represents the ratio of emitted photons to the injected electrons (per unit area, per unit time). It is influenced by both the device architecture and the materials used. From the physical point of view the quantum efficiency is one of the most meaningful device properties.

Electroluminescence in nanoparticles is of great practical importance because it may be used for various device applications also in combination with polymers or small molecules to obtain white emission. Inorganic nanoparticles used in combination with a conducting polymer have been reported to show strong luminescence signal under excitation by electric current [41] [42]. The main problem obtaining efficient electroluminescence is to get a dense ensemble of nanoparticles in a proper conducting environment providing charge injection and migration.

Nowadays intensive research effort have increasingly focused towards the development of efficient electroluminescent hybrid nanoparticle-polymer materials aiming to the fabrication of flexible organic white light emitting devices. In nanoparticle-polymer emitting layer the EL become a complex phenomenon that brings up a number of complicated aspects related to the charge transfer through a single nanoparticle and to the carrier migration in the matrix. In addition also the size and shape distribution of nanoparticles could influence dramatically the electroluminescene features and thus have to be carefully selected.

In the following section we discuss the EL-V measurements carried out on ITO/P3HT-CdS/LiF/Al device in order to record the electroluminescence response of P3HT-CdS nanocomposites synthesized *in-situ*.

6.4.1 Electroluminescence response of the P3HT-CdS nanocomposite

The EL analysis was performed using a photodiode, Newport 810UV, connected to a Keithley 6517A Electrometer. The EL emission of P3HT obtained by applying 8V ($0.4A/cm^2$) at ITO-Al electrodes and recording for 1min (Figure 6.13) shows a shoulder 650nm (1.88 eV) and peak at 730 nm (1.70 eV) as in the PL spectrum. The low energy peak is more intense than the high energy peak. This is generally explained as being due to emission from interchain (aggregate) excited states in P3HT, where symmetry considerations reduce the intensity of the high energy emission [43][44]. The turn on voltage for this device is about $5.4V$. The P3HT EL spectrum resembles that reported by Yu et al.[45] even if they got the spectrum at lower turn on voltage, $1.1eV$ by using a Ca electrode.

The EL spectrum of nanocomposite recorded at 8V ($1.5A/cm^2$) shows a broad feature peaked at 657nm. The turn on voltage, $5.1eV$, thus it is slightly lower than in the case of the P3HT based device. The nanocomposite based device is characterized by an enhanced EL signal. The presence of CdS nanoparticles induces the loss of the

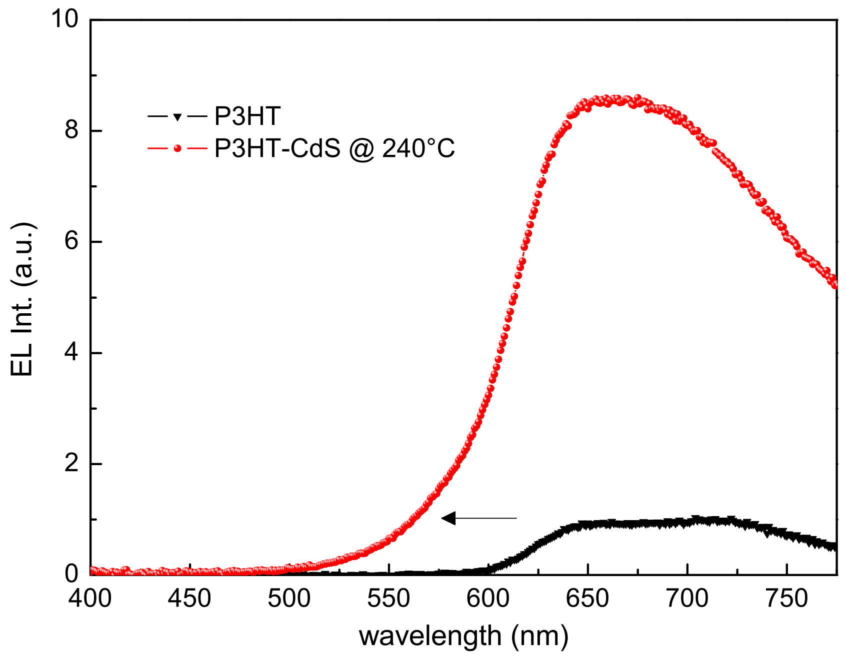

Figure 6.13: *EL spectra of P3HT (black square) and P3HT/CdS (red square) based devices. In the latter case the electroluminescent spectrum is appreciably enhanced and the color emission is shifted from red to orange*

double structure of the P3HT spectrum. The nanocomposite EL spectrum basically blue-shifts and the color emission changes from deep red into to light orange. This result suggests that both the P3HT and the CdS component emission are present. Concerning the influence on the change of EL spectrum by eventual charge transfer effect between the two materials nothing can be inferred.

In conclusion we have proposed a simple method to synthesize nearly monodispersed CdS nanoparticles in a P3HT matrix. The nanocomposites offer large forward current density of the order of $10mA/cm^2$ at 5V, and may be used in a diode structure with ITO and Al electrodes. In particular in a single layer electroluminescent device it shows improved performance in terms of spectral coverage with respect to the polymer only. However the device architecture must be optimized by adding, for instance, an hole/electron blocking layer at the electrodes in order to reduce the quenching effect probably responsible of the very low external EL efficiency ($\eta \sim 10^{-7}$ at 8V).

Bibliography

[1] G. Horowitz. Adv. Mater. 2, 287 (1990).

[2] M.M. Koetse, J. Sweelssen, K.T. Hoekerd, H.F.M. Schoo, S.C. Veenstra, J.M. Kroon, X. Yang, J. Loos, Appl. Phys. Lett. 88, 083504 (2006).

[3] M.M. Wienk, J.M. Kroon, W.J.H. Verhees, J. Knol, J.C. Hummelen, P.A. van Hal, R.A.J. Janssen, Angew. Chem. Int. Ed. 41, 3371(2003)

[4] G. Yu, K. Pakboz, A.J. Heeger. Appl. Phys. Lett. 64, 3422 (1994).

[5] D.S. Ginger, N.C. Greenham, Synth. Met. 124, 117 (2001).

[6] A.J. Nozik, Physica E 14, 115 (2002).

[7] R.B. Saunders, M.L. Turner, Advances in Colloid and Interface Science 138, 123 (2008).

[8] J.S. Salafsky, Phys. Rev. B 59, 10885 (1999).

[9] E. Bundgaard, F.C. Krebs, Solar Energy Materials and Solar Cells 91, 954 (2007).

[10] B. Sun, N.C. Greenham, Phys. Chem. Chem. Phys. 8, 3557, (2006).

[11] S. Cook, A. Furube, R. Katoh, Energy Environ. Sci. 1, 294 (2008).

[12] M. Reyes-Reyes, K. Kim, D.L. Carroll, Appl. Phys. Lett. 87, 083506 (2005).

[13] P. Vanlaeke, A. Swinnen, I. Haeldermans, G. Vanhoyland, T. Aernouts, D. Cheyns, C. Deibel, J. DHaen, P. Heremans, J. Poortmans, J.V. Manca, Solar Energy Materials and Solar Cells 90, 2150 (2006).

[14] Y. Zhao, Z. Xie, Y. Qu, Y. Geng, L. Wang, Appl. Phys. Lett. 90, 043504 (2007).

[15] J. Zhao, A. Swinnen, G. Van Assche, J. Manca, D. Vanderzande, B. Van Mele, J. Phys. Chem. B, 113 (6), 1587 (2009).

[16] L.S. Hung, C.H. Chen. Materials Science and Engineering R 39, 143, 114 (2002).

[17] M.A.M. Baldo, S.R. Forrest, Phys. Rev. B 64, 085201, (2001).

[18] C.J. Brabec, J. E. Shaheen, C. Winder, N.S. Sariciftci, P. Denk. Appl. Phys. Lett. 80, 1, (2002).

[19] Y. Hong, J. Kanicki, IEEE Transaction on Electron Devices 51, 10, 1562 (2004) .

[20] A.I. Maher, R.H. Klaus, Z. Uladzimir, G. Gobsch, S. Sensfuss Solar Energy Materials and Solar Cells 85, 1320 (2005).

[21] C. Ghezzi, C. Paorici C. Pelosi, Appl. Phys. 11, 4 (1976).

[22] R. Valaski, L.M. Moreira, L. Micaroni, I.A. Hummelgen, J. Appl. Phys. 92, 2035 (2002).

[23] A. Ruseckas, E. B. Namdas, T. Ganguly, M. Theander,M. Svensson, M. R. Andersson, O. Inganas, V. Sundstrom, J. Phys. Chem. B, 105, 7624 (2001).

[24] S. Cook, A. Furube, R. Katoh, Energy Environ. Sci. 1, 294 (2008).

[25] M. Sharma, D. Kaushik, R. R. Singh, R.K. Pandey, J. Mater. Sci.:Mater.Electron 17, 537, (2006).

[26] S. Cook, A. Furube, R. Katoh, Energy Environ. Sci. 1, 294 (2008).

[27] N. S. Sariciftci, L. Smilowitz, A.J. Heeger, F. Wudl, Science 258, 1474 (1992).

[28] D.S. Ginger, N.C. Greenham, Phys. Rev. B 59, 10622 (1999).

[29] N.C. Greenham, X. Peng, A.P. Alivisatos, Phys. Rev. B, 54, 17628 (1996).

[30] K. R. Choudhury, M. Samoc, A. Patra, P.N. Prasad, J. Phys. Chem. B 108, 1556 (2004).

[31] G. Li, V. Shrotriya, J. Huang, Y. Yao, K. Emery, Y.Yang, Nature Materials 4 (2005).

[32] H.C. Leventis, S.P. King, A. Sudlow, M.S. Hill, K.C. Molloy, S.A. Haque, Nanoletters DOI: 10.1021/nl903787j.

[33] K.Rikitake, D. Tanimura, W.Takashima, K.Kaneto, Jpn, J. Appl. Phys. 92, 9 5259 (2002).

[34] D.Braun, A.J. Heeger, Appl. Phys. Lett. 58, 1982 (1981).

[35] K.C. Kao and W. Hwang. *Electrical Transport in Solids*, Pergamon Press, Oxford (1981).

[36] N.F. Mott, R.W. Gurney, *Electronic Processes in Ionic Crystals*, Clarendon Press, Oxford (1940).

[37] A.Moliton, W.Rammal, B. Lucas, Europhys. Lett. 72(5), 754 (2005).

[38] M.A. Lampert, P.Mark, *Current injection in solids*, Academic Press N.Y. 1970.

[39] N.Deshmukh, J. Elect. Mater 36,6, (2007).

[40] . P.J. Sebastian, M.Ocampo, Sol.Energy. Mater. Sol. Cells 44, 1 (1996).

[41] J.H. Park, J.Y. Kim, B.D. Chin, Y.C. Kim, Jai K. Kim, O. Park, Nanotechnology 15, 1217 (2004)

[42] S. Coe-Sullivan, W.K. Woo, J.S. Steckel, M. Bawendi, V. Bulovi, Organic Electronics 4, 123 (2003).

[43] . J. Clark, C. Silva, R.H. Friend, F.C. Spano, Phys. Rev. Lett. 98, 206406 (2007).

[44] S.C.J. Meskers, R.A.J. Janssen, J.E.M. Haverkort, J.H. Wolter, Chem. Phys. 260, 415 (2000).

[45] G.Yu, H Nishino, A.J. Heeger, T.A.Chen, R.D. Rieke, Synthetic Metals 72, 249 (1995).

Conclusions

The main activities of the work described in this thesis have been devoted to the synthesis of semiconductor nanoparticles and hybrid nanocomposites to study their behavior in photo-to-electron conversion devices and other optoelectronic applications. The quantum size effects observed in the nanostructures were also presented. We studied both Ge and CdS as inorganic semiconductor materials, while the organic materials taken into account were Topas (TP), poly(n-vynilcarbazole) (PVK) and poly(3-hexylthiophene) (P3HT).

Concerning the synthesis of Ge nanostructures, we realized nano dots via a method of high temperature vacuum evaporation on SiO_2 substrates. The mechanism of Ge dots formation on a SiO_2 substrate allows to obtain a high dot density ($4{\times}10^{12}cm^{-2}$) and to avoid interdiffusion effects which generally lead to GeSi alloys at the interface of each dot when grown on Si substrates. Each Ge island is as small as 5.0nm in diameter and it is actually a sphere as revealed by STM study. Quantum size effects in those nanostructures have been evidenced by I-V measurements by using a STM probe on a single dot. The measurements show the widening of the energy gap into the single and isolated dot (up to 1.8 eV for 5.0 nm sized Ge dots). We demonstrated the ability of Ge quantum dots to generate photocurrent in the near UV and visible range using electrochemical photocurrent measurements. The photogenerated current depends on the excitation wavelength. By reducing the average dot size a dramatic change in the photocurrent spectrum occurs due to the quantum confinement effects. In particular quantum effects enhances the photocurrent yield in the visible range. Those results opens a new issue to Ge for photovoltaic nanodevices compatible with the existing Si based technology.

Concerning the synthesis of II-VI semiconductor such as CdS, we have shown that it is possible to prepare CdS nanocrystals adopting a simply synthetic route on the way to green chemical synthesis, the thermolysis of a single Cd precursor in octadecene. The thermolysis proceeds with the melting of the thiolate precursor and its transformation into the relative metal sulfide nanoparticles. The synthesis was performed at different annealing conditions and precursor concentration in order to investigate their influence on the CdS nanoparticles growth. We found that the CdS nanocrytals size mainly depends upon a combination of the temperature, speed and duration of the annealing procedure and also on the precursor concentration. In particular a low precursor concentration (3mmol) favors the formation of CdS nanocrystals with narrow size distribution and good optical properties already at $200^o C$. A higher concentrated solution (10mmol) needs higher temperature ($240^o C$) and long annealing time (30min) to allow the growth of 3nm sized nanoparticles. The samples exhibit excitonic PL emission is in the 400-425nm spectral range. The PL peak is sharp with FWHM between 20 and 50nm. On the basis of the results of HRTEM, EDS and WAXS the nanoparticles are characterized by a good degree of crystallinity even if the crystal phase has not yet clearly determined. Furthermore we accomplished in depositing uniformly the CdS nanoparticles on mica substrates as proved by AFM analysis. This results is particularly interesting in view of the technological application of the colloidal nanocrystals synthesized.

The proposed colloidal synthesis method is a one pot process involving a single source precursor. It is a low cost and environmental-friendly method which leads to the formation of nanocrystals with a surface passivated by thiol chains without the use of additional passivating agents. All the mentioned properties induce to the consideration that the thermolytic synthesis is a very promising technique which can be extended to other semiconductor compounds and provide an extensive nanoparticles production.

A great deal of work has been devoted to the synthesis of hybrid nanocomposites by inducing the growth of CdS nanoparticles in different polymer matrices. We first synthesized CdS nanoparticles in TP, an optically transparent and chemically inert olefin copolymer. The synthesis proceeded by in-situ thermolysis of the Cd thiolate precursor. The crystalline structure of CdS nanoparticles was investigated by grazing incidence diffraction measurements performed during the annealing process. The main result was that a temperature of 170^oC is sufficient for CdS nanoparticles in the cubic phase to form in thin films of TP. Significative results have been obtained by UV-Vis absorption and PL spectroscopy in the range $240 - 280^oC$. Quantum confinement effects have been proved by UV-Vis absorption measurements which also show that nanoparticles of 2.4nm in diameter become bigger with increasing temperature. The color emission goes from blue to orange annealing at 240^oC and 276^oC respectively. The presented results are an important and very promising step in taking full control of the production of CdS nanoparticles in polymer matrix with specific optical properties. The results obtained played a crucial role in the comprehension of the experiments concerning the synthesis of CdS in a conductive matrix where the nanocrystal optical signals cannot be clearly distinguished.

The next step was the synthesis of CdS nanocrystals in PVK by adopting the same synthetic procedure used with TP. CdS nanocrystals 2-3 nm sized were produced at annealing temperatures of 250^oC and 265^oC. The spherical nanocrystals, predominantly in the hexagonal phase, increase in size with the annealing temperature. Although the annealing temperature necessary to allow the thermolysis of Cd precursor in PVK is much higher than in the case of thermolysis in octadecene the nanoparticles size in the PVK matrix is up to one order of magnitude lower than in the colloidal synthesis. The results obtained from the synthesis in TP and supported by the experiments in PVK have proved that the CdS nanoparticles formation by thermolysis is a more controllable process in a polymer matrix than in the solvent. Consequently the method of thermolysis of Cd thiolate precursor is more effective in terms of small and uniform size production and reproducibility when it occurs in a matrix.

The PVK-CdS nanocomposites were used to realize single layer devices to investigate their conductive properties. We found from current-voltage measurements that the nanoparticles modify the dispersive transport in the matrix. The conductivity of the organic layer is enhanced up to six order of magnitude. Moreover a bistable behavior and negative differential resistance (NDR) have been detected when the devices is bi-

ased at 5V. The NDR is very sensitive to the nanoparticles, in particular to size and size distribution in the polymer matrix.
The enhanced conductive behavior of the nanocomposites with respect to the PVK only is expected to be related to charge transfer process between the polymer and the CdS nanoparticles. Such hypothesis is corroborated by quenching effect in the PL spectra of the nanocomposites. We observed that the smaller nanocrystals are more effective contributing to a more pronounced quenching effect. This is in agreement with the results obtained by electrical measurements.

At the end, we have applied the synthetic approach of thermolysis to a different conductive polymer, the P3HT, with the aim of investigating both its photocurrent and electroluminescent responses. We succeeded in synthesizing nearly monodispersed 2-3nm sized CdS nanoparticles in P3HT by annealing at 240^oC. The nanocomposite was then sandwiched between ITO and LiF/Al electrodes and the photocurrent measurements carried out. The results in terms of photon to electron conversion efficiency (IPCE), measured as function of wavelenght in the near-IR, visible and near-UV range, indicate that the photocurrent generation is mainly governed by the polymer and it is modified in the visible range by the nanoparticles. In particular, the IPCE results to be enhanced in the spectral region around 500 nm. The values of IPCE measured in the nanocomposite are of about 0.1% at 330 nm and 0.02% at 500 nm. The charge transfer process occurring in the nanocomposite between the organic and inorganic components and responsible of the IPCE enhancement, is supported by optical measurements which show a quenching effect of the PL emission of the P3HT. Anyway, since the amount of nanoparticles in the matrix is relatively low (the CdS/PVK volume fraction is 0.01), the photogenerated excitons generated in the active layer of the device mostly recombine before they can reach the electrodes. This might be the main cause of the low performance of the presented devices. Nevertheless our first attempts of realizing P3HT-CdS nanocomposites by thermolysis are encouraging because they demonstrate the advantage of the in-situ method in synthesizing almost uniformly dispersed nanoparticles. This characteristic has allowed slight improvement of the performance of the photoactive material even at small amount of nanoparticles. However, the photocurrent generation efficiency can be significantly improved by both adding a larger amount of CdS nanoparticles and optimizing the charge exchange between the nanoparticles and the polymer. The P3HT/CdS nanocomposite realized offers large forward current density of the order of $10mA/cm^2$ at 5V. In a single layer device configuration it works also as an electroluminescent material which extends the emission spectrum of the polymer only. Nevertheless the device architecture needs to be optimized for instance by adding hole/electron blocking layer at the electrodes in order to reduce the quenching effect probably responsible of the very low external EL efficiency ($\eta \sim 10^{-7}$ at 8V).

In conclusion in this thesis work we succeeded in realizing quantum confined nanoparticles of two different semiconductor materials, Ge and CdS. We proved by photocurrent measurements that the Ge nanodots can harvest the light producing a not negligible photocurrent signal. A simple route for the synthesis of CdS nanoparticles in colloidal solution as well as in polymer matrix (in-situ) has been proposed. The applicability of in-situ hybrid organic/inorganic nanocomposites to different optolectronic devices has been demonstrated.

Publications and proceedings

1. M. Scarselli, S. Masala, P. Castrucci, M. De Crescenzi, E. Gatto, M. Venanzi, A. Karmous, P. D. Szkutnik, A. Ronda, and I. Berbezier, ***Optoelectronic properties in quantum-confined germanium dots***, Applied Physics Letters 91, 1 (2007).

   Selected for "Virtual Journal of Nanoscale Science and Technology" Americal Institute of physics and American Physical Society (October 2007), www.vjnano.org.

2. M. De Crescenzi, M. Scarselli, A. Sgarlata, S. Masala, P. Castrucci, E. Gatto, M. Venanzi, A. Karmous, A. Ronda, P.D. Szkutnik, I. Berbezier, ***Photocurrent generation from Ge nanodots in the near UV and visible region***, Superlattices and Microstructures 44, 331336 (2008).

3. S. Masala, D. Capitani, M. De Crescenzi, A. De Girolamo Del Mauro, C. Minarini, M. Pentimalli, M. Scarselli, P. Vacca, O. Valentino and T. Di Luccio, ***Polymer/QD nanocomposites for OLED devices***. Proc. Conf. PPS-24, Polymer Processing Society, Salerno, June 2008.

4. T. Di Luccio, D. Carbone, S. Masala, C. Minarini, G. Nenna, P. Vacca, O. Valentino, ***Structural and optical properties of polymer/CdS nanoparticle films***, Proc. Conf. EL2008, Tivoli (Roma), Sept. 2008.

5. C. Borriello, S. Masala, V. Bizzarro, G. Nenna, M. Re, E. Pesce, C. Minarini, T. Di Luccio ***Luminescent nanocomposites of conducting polymers and in-situ grown of CdS quantum dots***, Proc. Conf. TOP Time Of Polymers, Ischia (Napoli) June 2010.

Acknowledgments

I would like to thank all the people who contribute during the various stages of my research to the realization of my PhD work. In particular I express my gratitude to Prof. M. De Crescenzi for support and motivation and for his precious suggestions and teachings. I am particularly grateful to Dr. Tiziana Di Luccio for her continuous assistance, for giving me many opportunities and for helping me in solving various problems both in this thesis work and on a personal level. I deeply appreciate it!

I like to thank Prof. L. Miglio for his support and encouragment, and Prof. G. Jabbour who has agreed to correct my thesis.

I am thankful to Eng. C. Minarini and Dr. D. Della Sala for supporting and giving me the possibility of working in a motivated and enterprising group with very friendly people. A special thank goes, indeed, to my colleagues at ENEA (Portici) with particular attention to the ”nano” group, especially G. Nenna, R. Miscioscia, V. Bizzarro, C. Borriello, A. De Girolamo Del Mauro, and F. Villani. I am also very thankful to the members of the group lead by Prof. De Crescenzi in Roma ”Tor Vergata” in particular Dr P. Castrucci and Dr. M. Scarselli for their collaboration and guidance in the interpretation of some results, and Dr. S. Del Gobbo for solid state photocurrent measurements and for giving precious insights into various aspects of our collaborative work. Finally thanks to Dr. M. Re and Dr. E. Pesce, from ENEA C.R. Brindisi, for providing the TEM images.